

**CHARACTER OF SIGNAL AND NOISE SOURCES IN DISPERSIVE AND STATIC  
FOURIER TRANSFORM REMOTE-SENSING RAMAN SPECTROMETERS**

A DISSERTATION SUBMITTED TO THE GRADUATE DIVISION OF THE UNIVERSITY  
OF HAWAI'I AT MĀNOA IN PARTIAL FULFILMENT OF THE REQUIREMENTS FOR  
THE DEGREE OF

DOCTOR OF PHILOSOPHY

IN

EARTH AND PLANETARY SCIENCE

AUGUST 2020

By:

Miles Jacob Egan

Dissertation Committee

Shiv K. Sharma, Chairperson

Anupam K. Misra

Przemyslaw Dera

Jasper Konter

David Jameson

*One man's noise is another man's data.*

## ACKNOWLEDGMENTS

Many people contributed in various ways to this thesis. I would like to thank my research advisors Shiv Sharma and Anupam Misra who supported my development as a graduate student both academically and financially. I would like to thank my committee members Przemyslaw Dera, Jasper Konter, David Jameson, Paul Lucey and Jeff Taylor for instructing me on mineralogy, elemental isotopic measurements, luminescence, remote-sensing, and petrology of the Moon and Mars. I would like to thank Tayro Acosta-Maeda for moral support and finding lost items. I would like to thank Mike Angel and his research group at the University of South Carolina for inviting me to visit his lab on two occasions and getting me started on research related to spatial heterodyne spectrometers. I would like to thank Roger Wiens for his support and direction in characterizing the SuperCam noise sources, and Ray Newell, Sam Clegg, Ann Ollila and Dawn Venhaus for offering their time and feedback on those characterizations. I would like to thank Nancy Hulbirt for her tireless help in producing publication-quality figures, often on short deadlines. Finally, I would like to thank my family for their steadfast support and encouragement without which I could not have succeeded.

## ABSTRACT

Raman scattering, the inelastic scattering of photons by polarizable vibrational modes, was first reported by Raman and Krishnan in *Nature* (Raman 1928) as combination scattering in liquids. Landsberg and Mandelstam reported observing the same effect in quartz simultaneously in *Naturwissenschaften* (Landsberg 1928). The discovery of the Raman effect was pivotal in support of the quantum theory of light and matter as the quantity of energy imparted to a scattered photon is always equal to a harmonic vibrational energy, regardless of the intensity of the excitation light source. Raman spectroscopy probes stereochemistry in a given target analyte and is therefore sensitive to the quantity of electron density shared between elements in a molecular vibrational mode as well as its reduced mass. Raman spectral features occur at well-defined energies as sharp, narrow peaks in contrast to IR spectra that occur as broad features caused by the multitude of symmetry-allowed ro-vibrational transitions for a given vibrational harmonic. The position of Raman peak centers is so selective that polymorphs, hydration states and compositional variation can be quantitatively characterized by peak centers alone.

Applying remote-sensing Raman spectrometers to probe the natural world was proposed as early as 1965 (Cooney 1965; Leonard 1970), but the successful implementation of such an instrument was said to be “impossible” by early authors (Hirschfeld 1972) because of the low value of Raman scattering cross-sections, the diminution of Raman signal with distance, the low number of Raman-active molecules illuminated in a remote-sensing Raman scattering experiment, and competition for a detector’s limited dynamic range with more luminous radiation sources. However, the advent of pulsed laser excitation sources and time-gated detectors made possible remote Raman measurements. Since that time, a number of research groups have proposed utilizing remote-sensing Raman spectrometers for planetary science

missions. Recent work has demonstrated the ability of remote-sensing Raman spectrometers to measure planetary science materials at hundreds to thousands of meters distance (Acosta-Maeda 2016; Misra 2020). Extensive calibrations have already been performed on planetary science materials, including modeling compositional variation as a function of Raman peak shifts, and crystallinity as a function of Raman linewidth. At the time of this publication, the first two Raman spectrometers are en route to Mars aboard the Perseverance rover (Beegle 2021; Wiens 2021).

Two classes of remote-sensing Raman spectrometers exist: dispersive grating spectrometers (Sharma 2003) and static Fourier Transform spectrometers (Gomer 2011). Differentiation between the two categories arises from how each spectrometer separates wavelength. The former separating wavelengths by use of an entrance slit and increasing with focal length of the spectrometer, and the latter separating wavelengths by phase differences between crossed wavefronts. Dispersive grating spectrometers attain high sensitivities as a result of localized detection of Raman modes on a detector and correlated photon-noise, while constrained by light throughput and narrow fields-of-view. Static Fourier Transform spectrometers attain medium sensitivities and large fields-of-view, while being limited by multiplicative photon-noise and diluted photon detection. In this work, the merits of both classes of remote-sensing Raman spectrometers are evaluated and their limits of sensitivity defined.

## TABLE OF CONTENTS

|  |       |
|--|-------|
| ACKNOWLEDGMENTS .....  | iii   |
| ABSTRACT.....  | iv    |
| TABLE OF CONTENTS.....   | vi    |
| LIST OF TABLES.....  | x     |
| LIST OF FIGURES .....  | xi    |
| LIST OF ABBREVIATIONS.....   | xviii |
| 1. Raman Spectroscopy – Theory and Laboratory Spectra of Geologic Materials .....            | 1     |
| 1.1. Introduction to Raman Scattering.....   | 1     |
| 1.2. Theory of Normal Raman Scattering.....  | 2     |
| 1.2.1. Classical Theory of Normal Raman Scattering .....                                     | 2     |
| 1.2.2. Polarization and Intensity of Raman Lines.....  | 4     |
| 1.2.3. Energy Diagram and Phenomenon of Luminescence, IR Absorption, and<br>Scattering ..... | 6     |
| 1.2.4. Resonance Raman Scattering.....   | 10    |
| 1.2.5. Normal Modes of Vibration and Selection Rules.....                                    | 11    |
| 1.2.5.1. Vibrational Modes of H <sub>2</sub> O Molecules .....                               | 13    |
| 1.2.5.2. Vibrational Modes of CO <sub>2</sub> Molecules.....                                 | 15    |
| 1.2.5.3. Vibrational Modes of MX <sub>3</sub> Molecules.....                                 | 16    |
| 1.2.5.4. Vibrational Modes of MX <sub>4</sub> Tetrahedral Molecules .....                    | 17    |
| 1.3. Classification of Crystal Vibrations.....   | 18    |

|   |    |
|---|----|
| 1.4. Experimental Methods.....  | 21 |
| 1.4.1. Excitation Laser Sources.....  | 22 |
| 1.4.1.1. Continuous Wave (CW) Lasers .....  | 22 |
| 1.4.1.2. Pulsed Lasers .....  | 23 |
| 1.4.2. Dispersive Spectrometers and Interferometers .....   | 24 |
| 1.4.2.1. Dispersive Raman Spectrographs .....   | 24 |
| 1.4.2.2. Fourier Transform Raman Spectrometers.....   | 25 |
| 1.4.3. Detectors for Raman Measurements with CW and Pulsed Lasers .....                               | 26 |
| 1.4.3.1. Detectors for Raman Measurements with CW Lasers .....  | 26 |
| 1.4.3.2. Detectors for Raman Measurements with Pulsed Lasers.....                                     | 27 |
| 1.4.4. Advances in Micro-Raman and Remote Raman Instruments.....                                      | 28 |
| 1.4.4.1. Advances in Micro-Raman Spectroscopy.....  | 28 |
| 1.4.4.2. Advances in Remote Raman Instrumentation.....  | 30 |
| 1.5. Raman Spectra of Planetary Ices and Geologic Materials.....                                      | 31 |
| 1.5.1. Raman Spectra of Planetary Ices .....  | 31 |
| 1.5.2. Raman Spectra of Geologic Materials .....  | 32 |
| 1.6. Summary.....   | 35 |
| 2. One Mirror, One Grating Spatial Heterodyne Spectrometer for Remote Sensing Raman Spectroscopy..... | 36 |
| 2.1. Development of Spatial Heterodyne Spectrometers for Planetary Science Applications .....         | 36 |
| 2.2. Design of a Modified Spatial Heterodyne Spectrometer.....  | 38 |
| 2.3. Samples.....   | 41 |

|  |    |
|--|----|
| 2.4. Experimental Results .....  | 42 |
| 2.4.1. Raman Spectra of Minerals, Salts and Organics as Measured by mSHRS42  |    |
| 2.4.2. Other Applications of mSHRS.....  | 49 |
| 2.4.3. Comparison of Raman Spectra of Minerals as Measured by SHRS and a<br>Diffraction Grating Spectrometer .....                             | 55 |
| 2.5. Summary.....  | 57 |
| 3. Suppressing the multiplex disadvantage in photon-noise limited interferometry via cross-<br>dispersed spatial heterodyne spectrometry ..... | 59 |
| 3.1. Development of Dispersed Fourier Transform Spectrometers .....  | 59 |
| 3.2. Theory of Multiplex Gain.....   | 62 |
| 3.3. Design of a Cross-Dispersed Spatial Heterodyne Spectrometer .....   | 63 |
| 3.3.1. First Light.....  | 65 |
| 3.3.2. Raman xSHS Interferograms .....   | 68 |
| 3.3.3. Visualizing the Multiplex Disadvantage.....   | 69 |
| 3.3.4. Mowing the Long Grass.....  | 71 |
| 3.3.5. Beating the Multiplex Disadvantage.....   | 72 |
| 3.4. The Abstemious Spatial Heterodyne Spectrometer .....  | 76 |
| 3.5. Summary.....  | 77 |
| 4. SuperCam Thermal-Vacuum Testing and Raman Detection Limits .....  | 79 |
| 4.1. Raman Spectrometers Take Flight to Mars .....   | 79 |
| 4.2. Thermal-Vacuum Testing .....  | 81 |
| 4.2.1. CCD Bias .....  | 82 |
| 4.2.2. Dark Current .....  | 84 |

|   |     |
|---|-----|
| 4.2.3. Effective Background Illumination.....             | 86  |
| 4.2.4. Background Signal Model .....                      | 88  |
| 4.2.5. Background Noise.....                              | 89  |
| 4.2.6. Photon Transfer Curves .....                       | 90  |
| 4.3. Raman and Luminescence Detection Limits .....        | 94  |
| 4.4. Tracking Raman Photons from Source to Detector ..... | 96  |
| 4.5. Summary .....  | 101 |
| 5. Summary .....  | 103 |
| References Cited .....                                    | 105 |

## LIST OF TABLES

### Chapter 1

- 1.1 Character table for point group  $C_{2v}$
- 1.2 CW laser radiation commonly used as Raman excitation

### Chapter 3

- 3.1 SNR comparisons of Raman peaks of cyclohexane measured with xSHS and pseudo-SHS. xSHS outperforms pseudo-SHS in terms of SNR for all but the strongest  $801.3 \text{ cm}^{-1}$  Raman line. For the weakest Raman features (i.e.  $384.1$ ,  $426.3$  and  $1347.9 \text{ cm}^{-1}$ ), xSHS can detect these features whereas SHS cannot.
- 3.2 Predicted SNR of cyclohexane's least luminous Raman features via SHS when acquiring interferograms in the full presence of the multiplex disadvantage.

### Chapter 4

- 4.1 Propagation of Raman photons from source to detector for gypsum  $\nu_1$  emission.

## LIST OF FIGURES

### Chapter 1

- 1.1 Jablonski energy-level diagram showing the virtual states involved in elastic (Rayleigh) and inelastic (Raman) scattering and the real electronic excited states involved in fluorescence and phosphorescence (see text for explanation). IC = internal conversion; ISC = intersystem crossing; F = fluorescence (lifetime picoseconds to nanoseconds), and P = phosphorescence (lifetime microseconds to seconds) (modified from Panczer et al. 2012).
- 1.2 Symmetry elements and normal modes of vibration for the water molecule. The + and – signs denote vibration going upward and downward, respectively, perpendicular to the plane of the paper.
- 1.3 Normal modes of vibration of CO<sub>2</sub> molecule (a) and MX<sub>4</sub> molecule (b).
- 1.4 Schematics of a confocal micro-Raman system with 180- and 135-degree scattering geometry with a CW Ar-ion laser and a pulse 532 nm laser, respectively.
- 1.5 Raman spectra of selected minerals. (a) spectra of  $\alpha$ -quartz, coesite and vitreous-SiO<sub>2</sub> (data from Sharma & Simmons 1981), (b) spectra of iron oxides/hydroxides and phyllosilicates (data from Edwards et al. 2004; Bishop & Murad 2004), (c) spectra of carbonates, nitrates and sulfates (data from Bishop 2017; RRUFF database: <http://rruff.info>), (d) spectra of feldspar and pyroxene minerals (data from Bishop et al. 2014).

### Chapter 2

- 2.1 A schematic diagram of the mSHRS used in this work.
- 2.2 The Raman spectra of plagioclase and forsterite as recorded by mSHRS at 3 meters distance. The Littrow angle was set to retro-reflect 554 nm ( $\sim 744 \text{ cm}^{-1}$ ) light.
- 2.3 The Raman spectra gypsum and anhydrite as recorded by mSHRS at 3 meters distance. The Littrow angle for gypsum and anhydrite was set to 584 nm ( $\sim 1671 \text{ cm}^{-1}$ ) and 554 nm ( $\sim 744 \text{ cm}^{-1}$ ), respectively.
- 2.4 The Raman spectra of milky quartz and dolomite as recorded by mSHRS at 10 meters. The Littrow angle for both minerals was set to retro-reflect 554 nm ( $\sim 744 \text{ cm}^{-1}$ ) light.
- 2.5 The Raman spectra of barite, calcite, and  $\alpha$ -quartz as recorded by mSHRS at 19 meters. The Littrow angle for all minerals was set to retro-reflect 554 nm ( $\sim 744 \text{ cm}^{-1}$ ) light.
- 2.6 The Raman spectra of  $\text{KClO}_3$ , naphthalene, and urea as recorded by mSHRS at 19 meters. The Littrow angle for  $\text{KClO}_3$  and urea was set to retro-reflect 554 nm ( $\sim 744 \text{ cm}^{-1}$ ) light, and the Littrow angle for naphthalene was set to retro-reflect 584 nm ( $\sim 1671 \text{ cm}^{-1}$ ) light.
- 2.7 The Raman spectra of three organic calibration targets as measured by SHRS at a distance of 19 meters from the telescope. The Littrow angle was set to retro-reflect 595 nm light in order to maximize SHRS's sensitivity to the C-H stretching region and the Raman fingerprint region (e.g.  $< 1800 \text{ cm}^{-1}$ ). The accumulation time was 10 seconds. The left panel shows the complete spectra of these three organic compounds while the right panel is windowed to highlight the Raman bands in the fingerprint region of the same spectra.
- 2.8 The Raman spectra of three aromatic hydrocarbons, benzene, m-xylene and p-xylene, as measured by SHRS 19 meters from the collecting optic.

- 2.9 The Raman spectra of three cyclical hydrocarbons (e.g., cyclohexane, cyclohexanone and nitrobenzene) as measured by SHRS at a distance of 19 meters from the telescope. The Littrow angle was set to retro-reflect 562 nm light so as to maximize the sensitivity of SHRS to peaks near  $1000\text{ cm}^{-1}$ . The accumulation time was 10 seconds.
- 2.10 The Raman spectra of three common constituents in hydrocarbon energy sources as measured by SHRS at a range of 19 meters from the collecting optic.
- 2.11 The Raman spectrum of calcite as measured by a diffraction grating spectrometer, two-grating SHRS and one-grating SHRS. The diffraction grating spectrometer attains the highest SNR, followed by the one-grating SHRS, followed by the two-grating SHRS while the spectral resolution characterized by the FWHM of this Raman band follows the reverse trend.

### Chapter 3

- 3.1 An image of xSHS used in the present work. Collimated light enters the Amici prism. Spectral light is refracted, then focused onto the gratings within SHS by a cylindrical lens. SHS generates Fizeau fringes, which are imaged by a lens and recorded by a CCD.
- 3.2 The interferograms of a Hg calibration lamp as measured by xSHS and SHS with and without bandpass filters. Note that the fringe contrast appears brighter for xSHS, even though  $\sim 22\%$  of incident light is lost due to reflections at the Amici prism surfaces, as a result of spectral light being focused along the y-axis by a cylindrical lens.
- 3.3 Fringe visibilities were calculated for each interferogram presented in **Fig. 3.2** by taking the brightest row and applying the standard formula  $v = I_{\max} - I_{\min} / I_{\max} + I_{\min}$ . For the xSHS interferograms,  $v_1$  represents the 546 nm fringe (in blue), and  $v_2$  represents the

577 and 579 nm fringes (in orange). Note that no change in the fringe visibility occurs for xSHS when bandpass (BP) filters are removed, while a significant degradation in fringe contrast does occur for SHS.

- 3.4 The xSHS interferogram of cyclohexane's Raman spectrum. The Littrow wavelength was  $\sim 532$  nm. As one scans from the bottom of the image to the top, the Raman shift increases. The brightest band at the top of the image is cyclohexane's C-H stretching region. The fringe with the highest contrast at the center of the image is cyclohexane's  $801.3 \text{ cm}^{-1}$  Raman mode. The xSHS interferogram was windowed to those pixels where spectral light occurred.
- 3.5 The above image illustrates the row by row FT of cyclohexane's xSHS Raman interferogram shown in **Fig. 3.4**. The low spatial frequencies near zero fringes per mm were masked so as to not skew the color scale by the first term in the Fourier series. Note that where a Raman feature occurs, multiplex noise is present across the entire row. This is the multiplex disadvantage (i.e. uncorrelated photon noise). By cross-dispersing spectral light before (or after) generating Fizeau fringes, the photon noise becomes correlated and the multiplex disadvantage is defeated.
- 3.6 The xSHS and Amici prism Raman spectra of cyclohexane. Three spectra are present here: the xSHS spectrum within the Nyquist limit (blue), the xSHS spectrum beyond the Nyquist limit (red) and the Amici prism spectrum (black). A slash was placed between the blue and red xSHS spectra as a visual aid to those viewing this figure in greyscale. The Amici prism spectrum is a proxy for total incident flux in a given row of the xSHS interferogram. Note that the Raman doublet at  $384.1$  and  $426.3 \text{ cm}^{-1}$  occurs at a local minimum in incident flux.

- 3.7 Plotted above are 100 spectra measured with xSHS (main figure) and 100 pseudo-SHS (sub-figure) spectra plotted, superimposed. In the pseudo-SHS spectra, the total incident flux per interferogram is much larger, which causes the low Raman shift modes at 384.1 and 426.3  $\text{cm}^{-1}$  to be washed out by multiplicative photon noise. In the pseudo-SHS spectra, spurious peaks appear in the  $\text{CH}_2$  bending region caused by aliasing of the C-H stretching modes.
- 3.8 The SNR vs.  $I(\sigma)/\overline{I(\sigma)}$  scatter plot presented here illustrates how SNR attained in an SHS experiment depends upon the ratio of the peak intensity divided by the mean of the interferogram. When the signal ratio becomes significantly small enough, the SNR equals one. Below this signal ratio, a spectral feature cannot be measured.

#### Chapter 4

- 4.1 A depiction of thermal-vacuum testing (TVAC) performed in order that the temperature-dependence of SuperCam's CCD bias, dark current, EBI, wavelength and resolution could be quantified.
- 4.2 The CCD bias as a function of channel number and detector temperature for the Transmission spectrometer.
- 4.3 Dark counts per second as a function of channel number and detector temperature for the Transmission spectrometer.
- 4.4 The intensifier temperature-dependence on intensifier background counts (EBI) at gain setting 3200 and gate-width of 10 ms.
- 4.5 The gain-dependence on intensifier background counts (EBI) for channel 5000 where the intensifier temperature was 37.2°C and the gate-width was 10 ms.

- 4.6 Background model estimates versus measured background data. The background data was acquired with the following parameters  $T_{\text{detector}} = 38.9^{\circ}\text{C}$ ,  $T_{\text{intensifier}} = 37.2^{\circ}\text{C}$ ,  $t_{\text{detector}} = 106$  ms,  $t_{\text{intensifier}} = 100$  ms, and gain = 2300.
- 4.7 A background model (black) for SuperCam with shot noise upper (red) and lower (blue) bounds versus 20 measured backgrounds plotted superimposed (semi-transparent). Nearly all the semi-transparent data points fall within the bounds, demonstrating that the background noise is a shot noise process.
- 4.8 A typical photon transfer curve where SNR is plotted against signal, and the slope of the line defines the dominate noise source (see figure annotations). This figure copied from (Janesick 2007).
- 4.9 SNR vs signal PTC plot for SuperCam's Green ROI in the absence of dark current noise. The crossing of the read (slope = 1) and shot noise (slope = 1/2) regime lines indicates the transition from one noise regime to another.
- 4.10 The SNR vs signal PTC as a function of temperature (range  $-46.2^{\circ}\text{C}$  to  $38.0^{\circ}\text{C}$ ) for the deuterium-tungsten halogen lamp as measured by SuperCam's Transmission spectrometer (Green ROI). The dotted lines represent three noise regimes experienced by SuperCam, namely read, shot and fixed pattern, that may be distinguished by their slopes. Read noise is defined by a slope of one; shot noise by slope of one-half; fixed pattern by slope of zero.
- 4.11 SNR vs signal PTC for active-sensing Raman measurements of SuperCam's transmission spectrometer (Orange ROI) taken during STT.
- 4.12 An illustration of the number of Raman photons scattered (e.g. gypsum's  $\nu_1$  band) within SuperCam's FOV for as a function of distance. As distance increases, the overlap

between SuperCam's FOV and laser spot increases. At large distances, slight misalignment angles cause the total energy captured by the FOV to decline.

## LIST OF ABBREVIATIONS

BP – bandpass

CCD – charge coupled device

CW – continuous wave

DC – direct current

DCG – dichromate gelatin

dFTS – dispersed Fourier transform spectrometer

DN – digital number

DPSS – diode pumped solid state

EBI – effective background illumination

EM – electromagnetic

FOV – field of view

FT – Fourier Transform

FWHM – full width half maximum

IC – internal conversion

ICCD – intensified charge-coupled device

IRF – instrument response function

ISC – intersystem crossing

LAMES – laser ablation molecular emission spectroscopy

LIBS – laser induced breakdown spectroscopy

MCP – micro channel plate

mSHRS – modified spatial heterodyne Raman spectrometer

PTC – photon transfer curve

PMT – photomultiplier tubes

SHRS – spatial heterodyne Raman spectrometer

SHS – spatial heterodyne spectrometer

SISAM – spectromètre interférentiel à selection par l'amplitude de modulation

SNR – signal to noise ratio

SPAD – single photon avalanche diode

TVAC – thermal vacuum

UV – ultraviolet

VPHG – volume phase holographic gratings

xSHS – cross-dispersed spatial heterodyne spectrometer

# Chapter 1. Raman Spectroscopy: Theory and Laboratory Spectra of Geologic Materials

## 1.1 Introduction to Raman Scattering

In 1928, C.V. Raman discovered inelastic scattering of light during the course of extended research on the molecular scattering of light (Raman 1928; Raman & Krishnan 1928). For this discovery, Raman was awarded the Nobel Prize in Physics in 1930 and the effect is known as the Raman Effect. Raman observed that when monochromatic light of frequency  $\nu_0$  is incident on a transparent sample, the spectrum of the scattered light shows two features. One is an elastically scattered light of identical frequency, called the Rayleigh line, and the other is a pattern of spectral lines of altered frequency ( $\Delta\nu_i$ ), called the Raman spectrum. The pattern on the low-frequency side of the exciting light ( $-\Delta\nu_i$ ), which is at longer wavelength than the exciting light, resembles the Stokes shift found in luminescence spectra. For this reason, these are referred to as Stokes Raman lines. The pattern is mirrored by an analogous pattern on the high-frequency side ( $+\Delta\nu_i$ ) at shorter wavelengths, referred to as anti-Stokes Raman lines. The relationship of intensities between the Stokes Raman lines and the anti-Stokes Raman lines depends on the temperature of the sample, as will be described later. Raman spectroscopy provides complementary information to infrared (IR) spectroscopy but the selection rules are different.

Raman spectral analysis has a number of advantages over passive IR and optical spectroscopy, chief among them being the sharpness and selectivity of spectral features. This allows unambiguous detection of specific minerals, in particular, mineral mixtures, rocks, isochemical glasses and fluid inclusions. A number of authors (White & De Angelis 1967; White 1975; McMillan 1985; McMillan & Hofmeister 1988; Nasdala et al. 2004; Dubessy et al. 2012)

have reviewed the applications of Raman techniques to geological materials. In this chapter, the basic theory of normal (spontaneous) and resonance Raman scattering are discussed along with advanced Raman techniques applicable to geologic materials.

## 1.2 Theory of Normal Raman Scattering

### 1.2.1 Classical Theory of Normal Raman Scattering

The phenomena of Rayleigh and Raman scattering can be explained in part by classic electrodynamics (Colthup et al. 1975). Light scattering, may be considered as an interaction between electromagnetic (EM) waves with matter that perturbs the electron clouds of the sample atoms and molecules. The perturbation of the electron cloud results in the periodic separation of the center of positive and negative charges within the atoms and/or molecules, which produces an induced dipole ( $P$ ). The oscillating induced dipole moment is a source of electromagnetic radiation, which may produce scattered light. For example, a hypothetical atom with a spherical symmetric electron cloud that has no permanent dipole moment can be modeled as

$$P = \alpha E \quad (1.1)$$

where  $\alpha$  is a constant of proportionality (also known as polarizability), and  $E$  is the magnitude of the electric field as described by  $E = E_0 \cos 2\pi\nu_0 t$ .

When the atoms and molecules are placed in an oscillating field of an electromagnetic light wave of frequency  $\nu_0$ , it will induce a dipole moment  $P$  given by the following equation

$$P = \alpha E_0 \cos(2\pi\nu_0 t) \quad (1.2)$$

where  $\nu_0$  is the frequency in Hz ( $c/\lambda_0$ , where  $c$  is the velocity of light and  $\lambda_0$  is the wavelength) of incident light, and  $t$  is time.

In the case of molecules, polarizability is not constant as certain vibrations and rotations of a molecule can cause  $\alpha$  to vary. For example, during the vibration of a diatomic molecule, the molecular shape is alternately compressed and extended. If the electron cloud is not identical at the extremes of the vibration, a change in polarizability will result.

For small displacements the polarizability of a diatomic molecule can be given as

$$\alpha = \alpha_0 + \left(\frac{\partial\alpha}{\partial Q}\right) dQ \quad (1.3)$$

where  $dQ$  is the difference between the internuclear distance at any time and the equilibrium internuclear distance, and  $\partial\alpha/\partial Q$  is the change of  $\alpha$  with respect to  $dQ$ . If the vibration is harmonic,  $dQ$  is given by

$$dQ = Q_0 \cos(2\pi\nu_{vib}t) \quad (1.4)$$

where  $Q_0$  is the maximum displacement about the equilibrium position, and  $\nu_{vib}$  is the vibrational frequency. Substituting the values of  $\alpha$  and  $dQ$  from Eqs. (1.3) and (1.4) in Eq. (1.5) yields

$$P = \alpha_0 E_0 \cos(2\pi\nu_0 t) + \left(\frac{\partial\alpha}{\partial Q}\right) E_0 Q_0 \cos(2\pi\nu_0 t) \cos(2\pi\nu_{vib}t) \quad (1.5)$$

Using the product to sum trigonometric identity, Eq. (1.5) can be rewritten as

$$P = \alpha_0 E_0 \cos(2\pi\nu_0 t) + \left(\frac{E_0 Q_0}{2}\right) \left(\frac{\partial\alpha}{\partial Q}\right) [\cos(2\pi(\nu_0 + \nu_{vib})t) + \cos(2\pi(\nu_0 - \nu_{vib})t)] \quad (1.6)$$

It is evident from Eq. (1.6) that the spectrum of the scattered light will contain the line corresponding to incident light (Rayleigh scattering) but also two modified lines corresponding to frequencies  $(\nu_0 + \nu_{vib})$  (Raman scattering). The intensity of the Rayleigh line depends on the

square of the amplitude, i.e.,  $(E_0\alpha_0)^2$ , and intensities of the Raman lines depend on  $(E_0Q_0/2)^2(\partial\alpha/\partial Q)^2$ , where  $\partial\alpha/\partial Q$  is the rate of change at which  $\alpha$  changes during a given normal mode of vibration. A necessary condition for Raman scattering is that  $\partial\alpha/\partial Q$  must be nonzero. Thus, we have a classical explanation of Stokes and anti-Stokes Raman lines. As demonstrated by Lord Rayleigh, the intensity of scattered light is proportional to  $\nu_0^4$ , and is responsible for the blue color of sky. According to the classical theory, the intensities of Stokes–Raman and anti-Stokes Raman lines should be  $(\nu_0 - \nu_{\text{vib}})^4/(\nu_0 + \nu_{\text{vib}})^4$ ; however, this prediction is not borne out by experiments, and is the main limitation of the classical theory.

### 1.2.2 Polarization and Intensities of Raman Lines

Polarization of incident radiation and the orientation of single crystal samples affect the intensities of Raman scattered radiation. Studies of the intensities of Raman lines in varying polarization and crystal orientations provides a valuable guide in assigning the observed frequencies to specific modes of vibrations.

As discussed previously, a normal mode of vibration is allowed in the Raman spectrum if the polarizability of the molecule changes during the mode. By resolving  $P$ ,  $\alpha$ , and  $E$  in the  $x$ ,  $y$ , and  $z$  directions, we anticipate the following relationships.

$$P_x = \alpha_x E_x; P_y = \alpha_y E_y; P_z = \alpha_z E_z \quad (1.7)$$

Equation (1.7) is applicable only to a completely spherical molecule. Most molecules, however, have structures that are not totally spherical; therefore, the equation does not hold in such cases because the direction of polarization does not coincide with the direction of the applied field. Instead of Eq. (1.7), we must use the following relationship instead:

$$\begin{bmatrix} P_x \\ P_y \\ P_z \end{bmatrix} = \begin{bmatrix} \alpha_{xx} & \alpha_{xy} & \alpha_{xz} \\ \alpha_{yx} & \alpha_{yy} & \alpha_{yz} \\ \alpha_{zx} & \alpha_{zy} & \alpha_{zz} \end{bmatrix} \begin{bmatrix} E_x \\ E_y \\ E_z \end{bmatrix} \quad (1.8)$$

The first matrix on the right-hand side is called the second rank polarizability tensor. It is a symmetric tensor, i.e.,  $\alpha_{xy} = \alpha_{yx}$ ;  $\alpha_{yz} = \alpha_{zy}$ ; and  $\alpha_{zx} = \alpha_{xz}$ . Equations (1.7) and (1.8) are for Rayleigh scattering. For Raman scattering, the polarizability components  $\alpha_{xx}$ ,  $\alpha_{xy}$ ,  $\alpha_{xz}$ , etc. should be replaced by the change in polarizability with respect to coordinate  $\partial\alpha_{xx}/\partial Q$ , and so on. The polarizability tensor can be visualized by means of a polarizability ellipsoid.

To define the term depolarization ratio in the Raman spectra of fluids, which measures the degree of depolarization of Raman lines, let us assume that the x axis is the direction of propagation of incident monochromatic light unto the sample and the direction of observation is perpendicular to the x-axis in the yz plane. If the plane polarized incident laser light is the excitation source, then the depolarization ratio  $\rho_p$  is defined as the ratio of intensity of the scattered light polarized perpendicular to the yz plane,  $I_{\perp}$ , to that polarized parallel to the yz plane,  $I_{\parallel}$ .

$$\rho_p = \frac{I_{\perp}}{I_{\parallel}} \quad (1.9)$$

In the case of fluid samples, including glasses, where all orientations of scattering molecules are possible, the degree of depolarization of a totally symmetric Raman line will be close to zero and the maximum degree of depolarization of an antisymmetric Raman line will be 3/4 (Colthup et al. 1975). A measurement of the depolarization ratio in gases, solutions, and glasses provides a means of distinguishing totally symmetric vibrations from the rest of the vibrational modes.

The effect of polarization of radiation and orientation of crystals on the Raman spectra was investigated using a 90-degree scattering geometry in the early days of Raman spectroscopic research on single crystals of sodium nitrate and calcite and found that the polarization of Raman lines varies with orientation of the crystals (Nadungadi 1939; Bhagavantam 1940). The polarized Raman spectral analysis of an oriented single crystal yields a detailed description of the vibration symmetry of the crystal vibrations. In the 1960s, Porto's group at the Bell Laboratories (Damen et al. 1966) proposed a useful notation to specify the relative orientation of the polarization vector. In the case of an oriented crystal excited by polarized laser light under a 90-degree scattering configuration, these authors proposed the notation  $x(zx)y$ , where  $x$  is the direction of propagation of incident light and  $y$  is the direction of propagation of scattered light. The terms within the parenthesis refer to the polarization of the incident light and scattered light, respectively. These terms represent the  $\alpha'_{zx}$  component of the change in the polarizability. By changing the polarization of the incident and observed scattered light, and the crystal orientation, all the components of the polarizability tensor can be observed. The polarized Raman spectra help in identifying symmetry species of various modes.

### **1.2.3 Energy Diagram and Phenomena of Luminescence, IR Absorption, and Scattering**

The interaction of light with matter can be explained graphically with the aid of an energy diagram that depicts the quantized nature of the energy states, as shown in **Fig 1.1**.

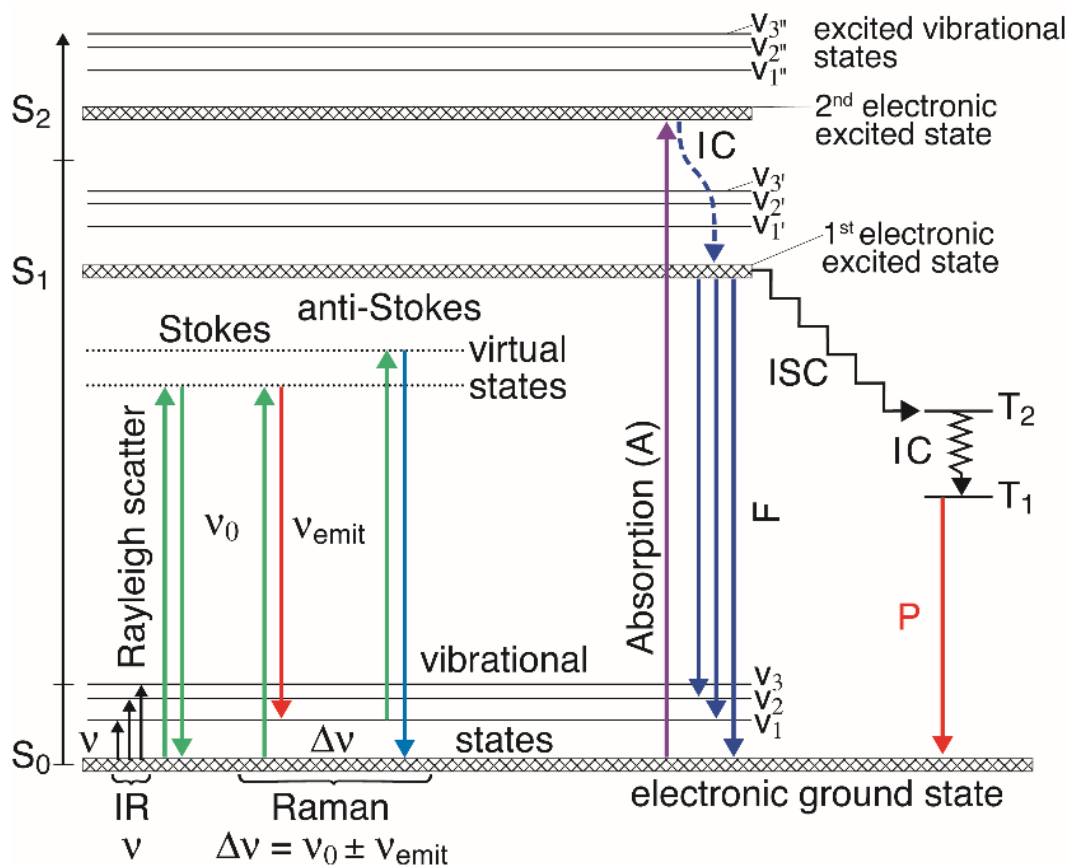


**Figure 1.1** Jablonski energy-level diagram showing the virtual states involved in elastic (Rayleigh) and inelastic (Raman) scattering and the real electronic excited states involved in fluorescence and phosphorescence (see text for explanation). IC = internal conversion; ISC = intersystem crossing; F = fluorescence (lifetime picoseconds to nanoseconds), and P = phosphorescence (lifetime microseconds to seconds) (modified from Panczer et al. 2012).

In the case of luminescence, a typical order of events is as follows. A molecule is excited by absorption of a photon to an excited electronic state (e.g. S<sub>2</sub>, the second excited singlet state) (see **Fig. 1.1**). The excited molecule relaxes to the first electronic excited state (S<sub>1</sub>) by internal conversion (IC), a nonradiative process, and can decay to the ground state by a radiative process emitting photons. This phenomenon is called fluorescence and has a lifetime in the range 10 ps to a few nanoseconds for biological and organic molecules. Another case may occur if a triplet

( $T_1$  and  $T_2$ ) electronic state available. An excited molecule in the first excited singlet state (e.g.  $S_1$ ) could decay by a nonradiative process to the triplet  $T_2$  excited state by intersystem crossing (ISC), followed by relaxation to the  $T_1$  excited state by a nonradiative IC process, and can decay to the ground state by phosphorescence. The lifetime for phosphorescence in minerals from transition metal ion and rare-earth ion impurities varies from sub-microseconds to milliseconds (Gaft et al. 2005; Gaft & Nagli 2009; Panczer et al. 2012).

During IR absorption, a molecule absorbs IR radiation and moves from ground vibrational state to an excited rotational-vibrational state. A few molecules will be in higher vibrational energy states, which are known as excited vibrational states. The fraction of molecules occupying a given vibrational state at a given temperature can be calculated using the Boltzmann distribution.

Atoms or molecules may elastically scatter light by first absorbing light, exciting the atom or molecule to a virtual state, followed by relaxation of the atom or molecule and simultaneous reemission of a photon of identical frequency to that of the incident light in a process known as elastic scattering or Rayleigh scattering (**Fig. 1.1**).

In Raman scattering, an absorbed photon is reemitted with lower energy, the difference between the incident and scattered photon corresponds to energy required to excite a molecule to a higher vibrational state (**Fig. 1.1**). This process gives rise to Stokes Raman lines. Similarly, a photon absorbed by a molecule in the excited vibrational state is reemitted with shorter wavelength by bringing the molecule to the ground state. This process gives rise to anti-Stokes Raman lines. This phenomenon of inelastic scattering is referred to as spontaneous or normal Raman scattering to distinguish it from stimulated Raman scattering, which is a nonlinear optical effect.

The intensity ratio of the Stokes Raman to anti-Stokes Raman lines of the sample will depend on the population of molecules in the ground and excited states, according to the following equation

$$\frac{I_{Stokes}}{I_{anti-Stokes}} = \frac{(\nu_0 - \Delta\nu)^4}{(\nu_0 + \Delta\nu)^4} e^{-(hc\Delta\nu/kT)} \quad (1.10)$$

where  $h$  is Planck's constant,  $k$  is Boltzmann's constant,  $T$  is the temperature in Kelvin, and  $\Delta\nu$  is the Raman shift due to a normal mode of vibration of the molecule ( $\nu_{vib}$ ) in  $\text{cm}^{-1}$ . This intensity ratio predicted based on the quantized nature of vibrational modes is consistent with the observed ratio of Stokes–Raman to anti-Stokes Raman lines. Based on Eq. (1.10), the Stokes to anti-Stokes ratio of Raman lines can be used to determine the temperature of the sample.

For a molecular bond, the individual atoms are confined to specific vibrational modes in which the vibrational modes are quantized (Kittel 1976). For example, the vibrational energy of a particular vibrational mode in a diatomic molecule can be given by the solution of the Schrödinger equation

$$\frac{d^2\Psi}{dq^2} + \frac{8\pi^2\mu}{h^2} \left( E - \frac{1}{2}Kq^2 \right) \Psi = 0 \quad (1.11)$$

where  $\Psi$  is the wave function of the quantum system,  $q$  is the atomic displacement from the equilibrium position, and  $\mu$  is the reduced mass of the system. For a diatomic molecule with molecular masses  $m_1$  and  $m_2$ , the reduced mass is  $1/\mu = 1/m_1 + 1/m_2$ ,  $h$  is the Planck's constant, and  $K$  is the force constant of the molecular bond. Solving for the condition that the wave function must be single valued, the eigenvalues are

$$E_v = (v + 0.5)h\nu_{vib} \quad (1.12)$$

where  $v$  is the vibrational quantum number,  $0.5h\nu_{vib}$  is the zero-point energy,  $\nu_{vib}$  is the vibrational frequency, and the frequency of vibration is given by

$$\nu_{vib} = \frac{1}{2\pi} \sqrt{\frac{K}{\mu}} \quad (1.13)$$

The vibrational frequencies depend on the reduced mass of atoms involved in a particular vibration. Isotopic substitutions have been used to assign the origin of the vibrational modes in silicate minerals and glasses (McMillan 1985).

#### 1.2.4 Resonance Raman Scattering

Resonance Raman scattering is a variant of the “normal” Raman scattering phenomenon. Normal Raman spectroscopy is typically performed using laser sources whose energy is above the vibrational or rotational energies of the molecule, but far below the first electronic excited state. Resonance Raman scattering takes place when the laser’s energy nears that of an electronic excited state (e.g. first or second electronic excited state in **Fig. 1.1**). In such a case, the Raman bands originating in the excited electronic transition may show very strong enhancements, with intensities  $10^3$ – $10^5$  higher than predicted by the  $\nu_0^4$  rule. When the excitation energy is in the vicinity of the electronic absorption, the term “pre-resonance Raman scattering” is commonly used. In minerals, Raman enhancement has been observed for the iron-containing oxides such as hematite ( $\alpha$ -Fe<sub>2</sub>O<sub>3</sub>), maghemite ( $\gamma$ -Fe<sub>2</sub>O<sub>3</sub>), and magnetite (Fe<sub>3</sub>O<sub>4</sub>) (de Faria et al. 1997; Nieuwoudt et al. 2011). For this group of minerals, pre-resonance Raman occurs with 636 nm excitation due to a spectral absorption band located near 640 nm (Cornell & Schwertmann 2003).

The resonance Raman spectra are also observed in biominerals containing chromophore biomolecules, such as carotene in pink corals (Urmos et al. 1991).

### 1.2.5 Normal Modes of Vibrations and Selection Rules

A polyatomic molecule composed of  $N$  atoms has  $3N - 6$  internal or vibrational degree of freedom ( $3N - 5$  in the case of a linear molecule). This is obtained by excluding translational and rotational degree of freedom from the total number of degrees of freedom. Corresponding to  $3N - 6$  degrees of freedom there are  $3N - 6$  fundamental or normal modes of vibrations and every other vibrational mode can be expressed as a linear combination of these normal modes.

The physical nature of the vibration modes depends mainly on the symmetry properties of the molecule. The activity of the normal modes in the Raman or IR spectrum also depends on the geometry of the molecule. The shape of the molecule can be specified by symmetry elements (e.g. axes of rotation, planes of symmetry, center of symmetry, etc.) that can be ascribed to it, which leads to a point-group notation. The point group implies that one point remains invariant under all the operations of the group. The first step in identifying the symmetries, and subsequently the Raman and IR active modes, is to identify the point group symmetry of the molecule or the crystal. Following Colthup et al. (1975), various types of vibrational modes or species in Mulliken symbols are designated according to symmetry operations, which they represent as follows

- A     symmetric with respect to principal axis of symmetry
- B     antisymmetric with respect to principal axis of symmetry

E doubly degenerate vibrations, the irreducible representation is two dimensional

F triply degenerate vibrations, i.e., a three-dimensional representation

g and u (subscripts) symmetric or antisymmetric with respect to a center of symmetry

1 and 2 (subscripts) symmetric or antisymmetric with respect to rotational axis (C) or rotation–reflection axis (S) other than the principal axis or in those point groups with only one symmetry axis with respect to plane of symmetry

Prime and double prime (superscripts) Symmetric or antisymmetric with respect to plane of symmetry.

For the linear molecules belonging to the point group  $C_{\infty v}$  and  $D_{\infty h}$ , capital Greek letter designations are used, the same as for electronic states for homonuclear diatomic molecules, as follows

$\Sigma^+$  symmetric with respect to plane of symmetry through the molecular axis

$\Sigma^-$  antisymmetric with respect to plane of symmetry through the molecular axis

$\Pi, \Delta, \Phi$  degenerate vibrations with degree of degeneration increasing in this order.

Group theory and its application to molecular vibrations have been described in several textbooks (Cotton 1963; Bhagavantam & Venkatarayudu 1969; Ferraro & Ziemeck 1969; Colthup et al. 1975; McMillan 1985; Rull 2012). Here, we focus on molecules of the type  $MX_2$ ,  $MX_3$ , and  $MX_4$ , where M is a positive valence atom and X is a negative valence atom, which are of interest in geologic and planetary science.

### 1.2.5.1 Raman and IR Active Modes of the H<sub>2</sub>O Molecule

The symmetry elements of the water molecule and the symmetric properties of the normal modes of vibration of the H<sub>2</sub>O molecule in C<sub>2v</sub> symmetry are shown in **Fig 1.2** and classified in **Table 1.1**. For N = 3 atoms in the water molecules the normal modes of H<sub>2</sub>O labeled T<sub>x</sub>, T<sub>y</sub>, and T<sub>z</sub> correspond to translational modes of the molecule moving the molecule as a whole, and three labeled as R<sub>x</sub>, R<sub>y</sub>, and R<sub>z</sub> correspond to the rotational modes of the molecule. These are referred to as the lattice or external vibrational modes of the molecule in solids.

In **Table 1.1**, the top row consists of the symmetry operations that form the point group. The first column lists the symmetry species that comprises the C<sub>2v</sub> point group. The symmetry species' irreducible representations appear in the column immediately to the right of Mulliken symbols. The individual characters indicate the result of the symmetry operation at the top of the column on a molecular basis for the symmetry. A comparison of the entries in **Table 1.1** with the vibrations shown in **Fig 1.2** shows that the vibrations do in fact fall into one or the other of these species as indicated in the **Fig 1.2**. **Table 1.1** also shows the symmetry species for T<sub>x</sub>, T<sub>y</sub>, and T<sub>z</sub>, and R<sub>x</sub>, R<sub>y</sub>, and R<sub>z</sub>. Only the vibrations of the symmetric species that include change in the electric dipole moment of the molecule (i.e. T<sub>x</sub>, T<sub>y</sub>, and T<sub>z</sub>) are IR active, and those that include change in the polarizability components are Raman active.

**Table 1.1** Character table for point group C<sub>2v</sub>

| C <sub>2v</sub> | E | C <sub>2</sub> (z) | σ <sub>v</sub> (xz) | σ <sub>v'</sub> (yz) |                |   |
|-----------------|---|--------------------|---------------------|----------------------|----------------|---|
| A <sub>1</sub>  | 1 | 1                  | 1                   | 1                    | T <sub>z</sub> | α <sub>xx</sub> , α <sub>yy</sub> , α <sub>zz</sub> |
| A <sub>2</sub>  | 1 | 1                  | -1                  | -1                   | R <sub>z</sub> | α <sub>xx</sub>                                     |

|                |   |    |    |    |                                 |               |
|----------------|---|----|----|----|---------------------------------|---------------|
| B <sub>1</sub> | 1 | -1 | 1  | -1 | T <sub>x</sub> ; R <sub>y</sub> | $\alpha_{zx}$ |
| B <sub>2</sub> | 1 | -1 | -1 | 1  | T <sub>y</sub> ; R <sub>z</sub> | $\alpha_{yz}$ |

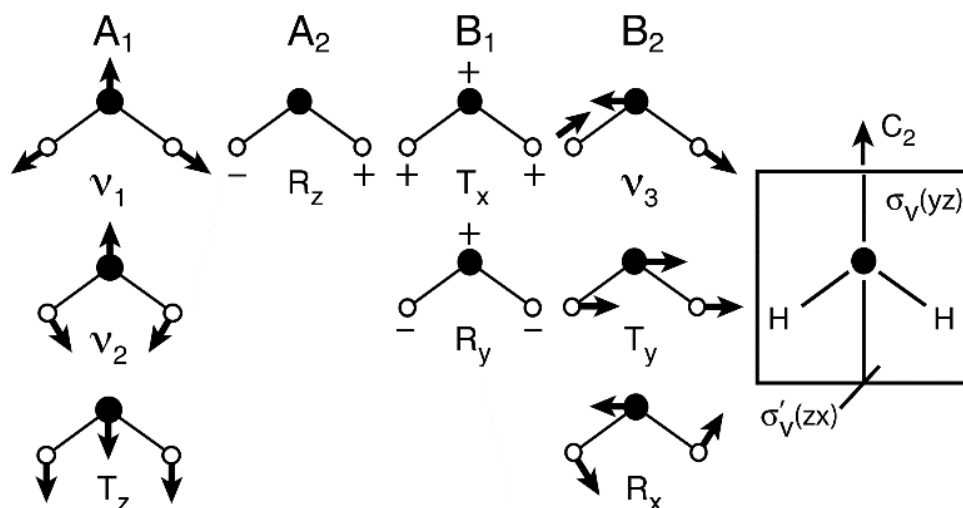


**Figure 1.2** Symmetry elements and normal modes of vibration for the water molecule. The + and – signs denote vibration going upward and downward, respectively, perpendicular to the plane of the paper.

The symmetric stretch mode  $\nu_1(A_1)$ , symmetric bending mode  $\nu_2(A_1)$  and the antisymmetric stretching mode  $\nu_3(B_2)$  are the three normal modes of vibrations of water molecule that are active both in the Raman and IR spectra. Accordingly, the three vibrational modes of water molecules can be classified according to the irreducible representation of the  $C_{2v}$  point group as  $\Gamma = 2A_1$  (R, IR) +  $B_2$  (R, IR). The R and IR refer to Raman active and IR active modes. The  $\nu_1$ ,  $\nu_2$ , and  $\nu_3$  modes of water vapors were observed in the first-order Raman and IR spectra at 3651, 1595, and 3755.8  $\text{cm}^{-1}$ , respectively (Herzberg 1945).

### 1.2.5.2 Raman and IR Active Modes of the CO<sub>2</sub> Molecule

**Fig. 1.3** illustrates normal vibrational modes of linear CO<sub>2</sub> and tetrahedral MX<sub>4</sub> molecules. The linear CO<sub>2</sub> molecule consists of three atoms and belongs to point group D<sub>∞h</sub> (Ferguson & Meister 1952). We should expect 3N – 5 or four normal modes of vibrations for this molecule (see **Fig. 1.3**). Molecules that have a center of inversion, such as CO<sub>2</sub>, adhere to rule of mutual exclusion that states a vibration that is active in IR will be Raman inactive and vice versa. The  $\nu_1(\Sigma_g^+)$  totally symmetric stretching of oxygen atoms does not involve any change in the electrical dipole moment of the molecule and will, therefore, be inactive in the IR but does involve change in the polarizability and therefore will be active in the Raman spectrum. The doubly degenerate  $\nu_2(\Pi_u)$  involves a motion of the carbon atom against the oxygen atoms in a line perpendicular to the symmetry axis of the molecule. The  $\nu_3(\Sigma_u^+)$  involves the oscillation of a carbon atom with respect to oxygen atoms along the symmetry axis of the molecule. Both the  $\nu_2$  and  $\nu_3$  vibrations possess change in the dipole moment of the molecule and are active in IR but inactive in the Raman spectrum.

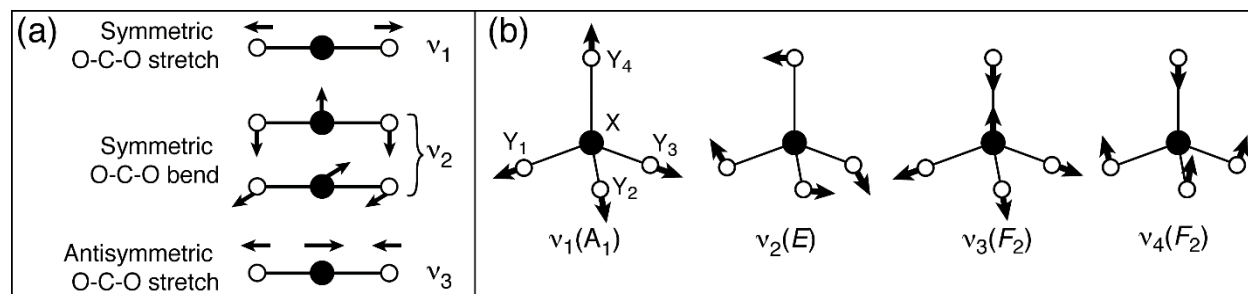


**Figure 1.3** Normal modes of vibration of CO<sub>2</sub> molecule (a) and MX<sub>4</sub> molecule (b).

According to the group theoretical analysis, the four vibrational modes of CO<sub>2</sub> can be classified according to the irreducible representation of the D<sub>∞h</sub> point group as

$$\Gamma = \Sigma_g^+(R) + \Sigma_u^+(IR) + \Pi_u(IR) \quad (1.14)$$

Strong IR bands observed for gaseous CO<sub>2</sub> are 667.3 and 2349.3 cm<sup>-1</sup>, and are assigned to the  $\nu_2$  and  $\nu_3$  modes, respectively. Group theory predicted a single Raman line in the Raman spectrum of a CO<sub>2</sub> molecule; however, a doublet consisting of Raman lines at 1388.3 and 1285.5 cm<sup>-1</sup> is observed. The doublet is assigned to an accidental degeneracy due to Fermi resonance between the  $\nu_1$  and the overtone ( $2\nu_2$ ) of the bending mode of CO<sub>2</sub> (Herzberg 1945).

### 1.2.5.3 Raman and IR Active Modes of the MX<sub>3</sub> Molecule

For MX<sub>3</sub> molecules where M is the central atom and X is a ligand, the simplest structures are planar and pyramidal. For planar structures, the three X atoms are at the corner of an equilateral triangle and M atom is at its center. The symmetry in this case is that of point group D<sub>3h</sub>. For a pyramidal structure, all the X atoms are at the corner of a pyramid and the M atom is at its center. The symmetry in this case is that of a point group C<sub>3v</sub>. The total number of normal modes of vibration for the MX<sub>3</sub> molecules will be six. According to group theory, the numbers of normal modes of vibrations belonging to each symmetry species are different in these two cases (Bhagavantam & Vaenkatarayudu 1969). These are summarized in the following respective irreducible representations

$$\Gamma_{D_{3h}} = A_1'(R) + A_2''(IR) + 2E'(IR) \quad (1.15)$$

For the pyramidal molecule

$$\Gamma_{C_{3v}} = 2A_1(R, IR) + 2E(R, IR) \quad (1.16)$$

For planar carbonate ions, the point group symmetry is  $D_{3h}$ . The Raman active totally symmetric stretching mode of carbonate  $\nu_1(A_1')$  appears at  $1088\text{ cm}^{-1}$ . The Raman and IR active doubly degenerate antisymmetric stretching mode  $\nu_3(E')$  and the antisymmetric in plane bending mode  $\nu_4(E')$  appear at  $1438$  and  $714\text{ cm}^{-1}$ , respectively. The IR active nondegenerate out of plane bending mode  $\nu_2(A_2')$  appears at  $880\text{ cm}^{-1}$ .

The pyramidal  $\text{NH}_3$  molecules, which belong to the  $C_{3v}$  point group, should display four Raman lines, which are all present in the IR absorption spectra (Buback & Schultz 1976). In the Raman spectrum of ammonia the totally symmetric  $\nu_1(A_1)$  mode appears as a strong polarized line at  $3336\text{ cm}^{-1}$  and as a weak line in the IR spectra. The symmetrical bending mode  $\nu_2(A_1)$  appears as a polarized Raman line at  $950\text{ cm}^{-1}$ . The Raman and IR active doubly degenerate antisymmetric stretching mode  $\nu_3(E)$  and the antisymmetric bending mode  $\nu_4(E)$  appear at  $3444$  and  $1626\text{ cm}^{-1}$ , respectively (Buback & Schultz 1976). This shows that it is possible to differentiate between the molecules in  $D_{3h}$  and  $C_{3v}$  point groups based on the polarized Raman spectra.

#### 1.2.5.4 Raman and IR Active Modes of the $\text{MX}_4$ Tetrahedral Molecule

A number of minerals including perchlorate, silicates, and sulfates have basic building blocks that have tetrahedral symmetry. The symmetry of these  $\text{MX}_4$  molecules or ions is that of point group  $T_d$ . The total number of normal modes of vibration for  $\text{MX}_4$  is nine. According to group theory, these modes of vibrations can be classified according to the irreducible representation of the  $T_d$  point group as  $\Pi_d = A_1(R) + E(R) + 2F(R, IR)$ . **Figure 1.3b** illustrates these four fundamental modes of vibrations. For isolated silicate ions, the totally symmetric Raman active

$\nu_1(A_1)$  line appears at  $819\text{ cm}^{-1}$ . The doubly degenerate Raman active symmetric bending mode  $\nu_2(E)$  appears at  $340\text{ cm}^{-1}$ ; and the triply degenerate antisymmetric stretching  $\nu_3(F)$ , and antisymmetric bending modes,  $\nu_4(F)$ , appear, respectively, at  $956$  and  $527\text{ cm}^{-1}$  (White 1975).

### 1.3 Classification of Crystal Vibrations

In crystalline solids, atoms are arranged in a periodic lattice and strong forces exist between neighboring atoms. If one atom is displaced from its mean equilibrium position, the neighboring atoms also undergo displacements. Therefore, the atomic motions in solids are collective rather than individual. These motions give rise to normal modes of vibrations, which travel as a wave through the crystal. The energy of these waves is quantized. The pseudo-particles associated with these waves are referred to as phonons, by analogy with the term photon for a quantized unit of light energy.

A crystal containing  $N$  atoms in the primitive cell has  $3N$  degrees of freedom, of which three are associated with the translation of the unit cell as a whole and thus become acoustic modes. The acoustic modes are responsible for the propagation of sound waves through the crystal lattice. Thus, the number of lattice vibrations that may be observed by Raman and IR spectroscopy is equal to  $3N - 3$  and are referred to as “optical modes.” The transverse and longitude modes are referred to as TO and LO modes.

A classification of the crystal vibrational modes into internal (molecular) and external (lattice) vibrations can be accomplished by taking into account the factor group of the crystal instead of the entire space group. A factor group is defined as the group formed by the symmetry elements present in the smallest unit cell, which is called a Bravais cell. The Bravais cell is defined in such

a way that the pure lattice translations of the unit cell can be used to obtain the entire space group. A factor group is always isomorphous with one of the 32 crystallographic point groups (Bertie & Bell 1971).

The analysis of the vibration at  $k = 0$ , the center of the Brillouin zone, for the entire crystal can be accomplished by two principal methods. The first is the factor group method of Bhagavantam and Venkatarayudu (1939) that considers the atoms in the Bravais unit cell as a large molecule. The crystallographic unit cell may be identical with the Bravais cell or it may be larger by some simple multiple. For example, for all X-ray crystal structures designated by a symbol P (for primitive) or R (rhombohedral primitive), the crystallographic unit cell and Bravais unit cell are identical. Crystal structures designated by capital letters I, A, and C have unit cells that contain two Bravais cells. Crystal structures designated by capital letter F (Face-centered) have unit cells that contain four Bravais cells. For factor group analysis the number of molecules per crystallographic unit cell should be divided by the cell multiplicity, e.g. by 4 for an F cell, by 2 for I, A, and C cells, and by 1 for P and R cells (Fateley et al. 1972; Salthouse & Ware 1972). Adams and Newton (1970 a,b) established tables for factor group analysis of vibrational modes for all space groups.

The other method is called the site group method of Halford (1946), which involves deriving the number of allowed modes of specific molecular entities based on site symmetry of the molecule in the unit cell. It is an approximation that can be used for molecular crystals such as carbonates, sulfates, and phosphates, where the forces between molecules are considerably weaker than those between the atoms inside the molecules. Hornig (1948) and Winston and Halford (1949) discuss the relationship of the factor group method to the site group method. These authors showed that it is possible to get equivalent results using either of the methods.

Maraduddin and Vosko (1968), and Warren (1968) provide an in-depth discussion on factor group analysis for the full Brillouin zone. Based on factor group analysis, Ferraro (1975) listed selection rules for some common minerals. Fateley et al. (1972) developed the correlation of the site group to the factor group. DeAngeles et al. (1972), and Fateley et al. (1972) summarized the procedure to perform calculations for the zone center ( $k = 0$ ) phonons. To assist with the analysis of vibrational modes in crystals, a set of online databases is available that includes data from international tables, space groups, and point groups; symmetry relations between space groups; and a k-vector database with Brillouin zone figures and classification tables of the wave vectors for space groups (Aroyo et al. 2006a, 2006b, 2011).

The essentials of factor group analysis are illustrated in the text that follows for calcite and aragonite polymorphs of calcium carbonate minerals. The rhombohedral primitive cell of calcite (space group #167,  $D_{3d}^{16}$  or  $R\bar{3}C$ ) contains two  $\text{CaCO}_3$  formula units, i.e., a total of 10 atoms; its 27 ( $3N - 3$ ) vibrational modes can be classified according to the irreducible representations of the  $D_{3d}$  point group as follows

$$\Gamma_{D_{3d}} = A_{1g}(R) + 4E_g(R) + 3A_{2g}(\text{i. a.}) + 2A_{1u}(\text{i. a.}) + 3A_{2u}(\text{IR}) + 5E_u(\text{IR}) \quad (1.17)$$

where R = Raman active, IR = IR active, and i.a. = inactive mode.

At room temperature, in the polarized Raman spectra of an oriented single crystal of calcite the following fundamental internal modes of the  $\text{CO}_3$  ion are detected (Porto et al. 1966):  $\nu_1(A_{1g}) = 1088 \text{ cm}^{-1}$ ; doubly degenerate  $\nu_3(E_g) = 1434 \text{ cm}^{-1}$ , and  $\nu_4(E_g) = 711 \text{ cm}^{-1}$ . The two doubly degenerate  $E_g$  translational and rotation lattice modes of calcite are observed at the 156 and 283  $\text{cm}^{-1}$ , respectively. The Raman line observed at 1750  $\text{cm}^{-1}$  is a combination ( $\nu_1 + \nu_4$ ) mode.

The orthorhombic cell of aragonite (space group #62,  $D_{2h}^{16}$  or  $P_{nma}$ ) contains four formula units and 20 atoms in total. According to Fateley et al. (1972), its 57 vibrational modes can be classified as follows

$$\Gamma_{D_{2d}} = 9A_g(R) + 6A_u(ia) + 6B_{1g}(R) + 8B_{1u}(IR) + 9B_{2g}(R) + 5B_{2u}(IR) + 6B_{3g}(R) + 8B_{3u}(IR) \quad (1.18)$$

Of the 30 Raman active fundamental modes of aragonite, 28 have been identified in single crystal measurements at 80 K (De La Pierre et al. 2014). The following internal modes of vibrations of  $CO_3$  were detected: four  $A_g$  (705, 854, 1087.2, and 1466.2  $cm^{-1}$ ); two  $B_{1g}$  (705.9 and 1464.1  $cm^{-1}$ ); three  $B_{2g}$  (716.9, 911.1, and 1579.0  $cm^{-1}$ ); and one  $B_{3g}$  (700.1  $cm^{-1}$ ). On the basis of theoretical calculations De La Pierre concluded that the two internal modes  $B_{2g}$  (1091.6  $cm^{-1}$ ) and  $B_{3g}$  (1415.0  $cm^{-1}$ ) have zero intensity. Due to the low intensities of these bands, these could not be detected in the Raman spectra (De La Pierre et al. 2014).

## 1.4 Experimental Methods

Raman spectroscopy was initially considered a physics curiosity until the invention of lasers because the intensities of Raman lines are extremely weak without a high-intensity monochromatic light source. This was despite the fact that Raman studies of several minerals and pure compounds had been carried out at the macroscopic scale using 404.6, 435.8, and 253.65 nm light from mercury emission lamps as the excitation ( $\lambda_0$ ) source. Lasers that became available during the 1960s were able to provide high irradiance of monochromatic light onto samples for recording the Raman spectra. The following subsections outline the advancements in (1) continuous wave (CW) and pulsed laser excitation sources; (2) Raman dispersive

spectrometers and interferometers; (3) detectors used for Raman measurements with CW and pulsed lasers, respectively; and (4) advances in micro-Raman and remote Raman instrumentation.

### 1.4.1 Excitation Laser Sources

Various lasers used for exciting Raman spectra of samples can be classified into two basic categories: (1) CW laser sources and (2) pulsed laser sources.

#### 1.4.1.1 CW Lasers

In modern Raman spectroscopy systems three types of CW ionized-gas lasers are being used: Ar-ion, Kr-ion, and mixed ArKr-ion lasers. The wavelengths of these lasers are stable and known within an accuracy of  $\sim 1$  pm which corresponds to  $0.04 \text{ cm}^{-1}$  around 500 nm. In addition, CW HeNe and HeCd lasers are also used as Raman excitation sources. Various excitation wavelengths these lasers provide are listed in **Table 1.2**.

**Table 1.2** CW laser radiation commonly used as Raman excitation

| Continuous-wave lasers | Wavelengths (nm)           |
|------------------------|----------------------------|
| Ar-ion                 | 457.9, 488.0, 514.5        |
| Kr-ion                 | 532.9, 566.2, 647.1, 676.4 |
| He-Ne                  | 632.8                      |
| He-Cd                  | 325, 441.6                 |

With these lasers, laser line filters or pre-monochromators are used to eliminate all plasma line emissions. The plasma lines may, however, be used as a wavelength standard for calibrating the Raman spectrograph (Pandya et al. 1988).

The compact UV hollow cathode NeCu ion-lasers, which emit CW radiation at 248.6 nm with output power up to >50 mW (Storrie-Lombardi et al. 2011), have recently been selected as the excitation source for the SHERLOC instrument on NASA's Mars 2020 rover mission (Beegle et al. 2014).

Diode Pumped Solid State (DPSS) CW Nd:YAG lasers that emit fundamental radiation at 1064 nm with output power of several watts are commonly used as an excitation source with Fourier Transform-Raman (FT-Raman) spectrometers. The linewidth is  $< 1 \text{ cm}^{-1}$  in standard lasers. In addition to the 1064 nm laser wavelength, radiation at 532, 355, and 266 nm can be obtained with frequency doubling, tripling, and quadrupling crystals.

Single-mode, frequency stabilized near-IR 785 and 830 nm diode lasers with linewidth  $< 1 \text{ cm}^{-1}$  are increasingly finding applications in Raman spectroscopy as excitation sources (Angel et al. 1995; Cooney et al. 1995; Cooper et al. 1995; Wang et al. 1995, 2012; McCreery 2000). When excited with near-IR lasers, the Raman spectra of some minerals and related materials display strong laser-induced fluorescence lines from rare-earth elements, which may be mistakenly identified as Raman lines (Aminzadeh 1997; Kaszowska et al. 2016).

#### **1.4.1.2 Pulsed Laser Sources**

In the past, flash lamp pumped or diode pumped solid state (DPSS) Nd:YAG pulsed 532 nm laser excitation sources were not usually used for exciting Raman spectra of geologic samples.

This was because a focused nanosecond-pulsed beam could damage the samples when used in 180-degree scattering geometry. Sharma (1989) demonstrated that a 532-nm pulsed laser could be used by focusing the expanded excitation beam in a 135-degree scattering geometry and collecting the scattered beam with a 20× objective. A spectrally narrowed (< 0.1 nm), 532 nm, passively Q-switched microchip laser with 600 ps pulses (1.5 μJ, 40 kHz) has also been used to measure the micro-Raman spectra of minerals in 180-degree scattering geometry (Blacksberg et al. 2010, 2016).

## **1.4.2 Dispersive Spectrometers and Interferometers**

Both grating-based dispersive and interferometer-based Raman spectrometers have been developed for measuring Raman spectra of minerals and inorganic and organic materials. The following gives a brief description of these two types of Raman spectrographs.

### **1.4.2.1 Dispersive Raman Spectrographs**

In modern spectrographs, an important component is the dispersing element. Two types of gratings are available: transmission gratings and reflection gratings. Dubessy et al. (2012) reviewed the properties of various gratings. Holographic gratings are used to efficiently reject stray light and eliminate ghost lines in the spectrographs. Both plane and concave holographic gratings are used in commercial Raman spectrometers (Delhaye & Dhamelin court 1975; Dhamelin court et al. 1979; Li & Deen 2014). Most dispersive Raman spectrographs employ the Czerny–Turner configuration. The aperture of Czerny–Turner optics is limited to F/4 or slower in order to minimize chromatic and spherical aberrations.

In the past two decades, the technology of Volume Phase Holographic gratings (VPHGs) has been widely exploited in the field of Raman spectroscopy for instrumentation that works both in the visible and in the near-IR (Arns et al. 1995, 1999). This is because they have very large diffraction efficiency even at very high dispersion and are easy to customize (each VPHG is a master grating). In VPHGs the diffraction of light occurs due to a periodic modulation of the refractive index in the volume of an active material such as dichromate gelatin (DCG) (Arns 1995). These holographic gratings have found applications in Raman instrumentations (Battey et al. 1993; Arns 1995; Owen 2007). These gratings have been instrumental in developing compact and high-throughput Raman spectrographs for planetary applications (Wang et al. 2003; Sharma et al. 2005; Gasda et al. 2015).

Due to the low ( $\sim 10^{-7}$ ) efficiency of Raman scattering and potential high efficiency of Rayleigh ( $10^{-3}$ ) scattering combined with reflection of the laser excitation radiation ( $\lambda_0$ ), rejection of  $\lambda_0$  radiation before it reaches the detector must be achieved to avoid detection of unwanted light. In the past, double and triple Czerny–Turner spectrographs were developed to measure low-wavenumber Raman spectra (McCreery 2000). Rejection of the excitation  $\lambda_0$  laser radiation has been made possible with advanced holographic notch filters and dielectric edge filters, which allows the use of only a single stage Czerny spectrograph for Raman scattering measurements down to  $50 \text{ cm}^{-1}$ . Since 2011 ultra-narrow holographic notch filters have been developed that allow the measurements of Raman lines down to  $\sim 10 \text{ cm}^{-1}$  (Lebedkin et al. 2011).

#### **1.4.2.2 FT-Raman Spectrometers**

The development of laboratory-based FT-Raman spectrometers based on Michelson interferometers was motivated by the possibility of (1) achieving higher resolution than is possible with the dispersive grating based instruments (Jennings et al. 1986); and (2) measuring near-IR excited Raman spectra of materials that are highly fluorescent when excited with visible radiation (Chase 1986; Hirschfeld & Chase 1986). In FT spectrometers, the limiting resolution does not depend on the size of the aperture, so high spectral resolution can be achieved without sacrificing the optical throughput. Multichannel FT-Raman systems that combine a common-path interferometer (Sagnac) with near-IR laser excitation (Zhao & McCreery 1996, 1997), and spatial heterodyne interferometers with 532 nm and UV pulsed laser excitations have been developed (Gomer et al. 2011; Hu et al. 2015; Lamsal et al. 2016). The multichannel FT-Raman systems with pulsed laser and gated ICCD detectors do not have any moving parts, thus offering an advantage for standoff measurements under high ambient light environments.

Relative to FT instruments, Czerny-Turner spectrometers benefit from robust design (no moving parts) and smaller FOV, which is sometimes desirable when one wants to measure individual mineral grains rather than multiple phases. Echelle spectrographs are not typically used for Raman because Raman scattering is so weak, and the spectral range and resolution enhancements are not needed unless Raman isotopic shifts are desired.

### **1.4.3 Detectors for Raman Measurements with CW Lasers and Pulsed Lasers**

Various detectors used in CW and time-resolved modes with pulsed lasers are briefly discussed in the following subsections.

#### **1.4.3.1 Detectors for Raman Measurements with CW Lasers**

Single channel photomultiplier (PMT) tubes were used during 1960–1980 for Raman spectroscopy. These PMT detectors were used in the first Raman microprobes at ambient pressures (Delhaye & Dhamelincourt 1975; Rosasco et al. 1975) as well as in high-pressure Raman with the diamond anvil cell (Adams et al. 1977; Sharma 1979). In the mid-1980s, the first popular multichannel detectors were linear intensified photodiode arrays of 1024 pixels with dimensions of 3 mm × 24 μm (Denson et al. 2007). These diode array detectors significantly reduced the measurement time as a 1024-pixel spectral wavelength could be measured simultaneously in 1s; however, the spectral resolution was degraded because of the size and number of pixels. Charge-coupled device (CCD) cameras appeared in mid-1990 and replaced all the other detectors because of their high quality. The CCDs are made up of two-dimensional arrays of individual pixels. The common dimensions of CCD used in Laboratory Raman spectrographs are 1024 × 256 pixels. The pixel size is typically 26 μm × 26 μm. The dynamic range of most laboratory CCDs is 16 bit (e.g. maximum counts 65,536 = 2<sup>16</sup>).

#### **1.4.3.2 Detectors for Raman Measurements with Pulsed Lasers**

Minerals and rocks containing transition metal and rare-earth ions can produce luminescence spectra that in some cases overlap with their Raman spectra. The lifetime of mineral photoluminescence is much longer (microseconds to milliseconds) as compared with the lifetime of the Raman signal that is ~ 10<sup>-13</sup> s. The difference in the lifetime of Raman scattering and fluorescence has been exploited to minimize interference by luminescence with the Raman spectra by using pulsed laser excitation and a gated detection (Matousek et al. 1999; Carter et al.

2005a,b; Misra et al. 2005; Blacksberg et al. 2010). Raman spectrometers equipped with intensified CCD (ICCD) detectors or single-photon avalanche diode (SPAD) array detectors and pulsed laser excitation allow measurements of Raman spectra of minerals with minimum interference from photoluminescence as well as from ambient light (Blacksberg et al. 2010; Carter et al. 2005b; Sharma 2007). The ICCD detectors normally allow gating down to 2 ns and the SPAD arrays offer gating down to 0.5 ns, thus effectively minimizing interference from mineral photoluminescence and short-lived fluorescence (>0.5 ns) from organic and biological molecules, respectively.

#### **1.4.4 Advances in Micro-Raman and Remote Raman Instruments**

Since the late 1990s, significant advances have been made both in the micro-Raman and remote Raman instrumentation. These advances in Raman instrumentation are briefly outlined in the text that follows.

##### **1.4.4.1 Advances in Micro-Raman Spectroscopy**

**Figure 1.4** shows a schematics of a micro-Raman system with CW Ar-ion laser, 488 and 514.5 nm radiation used in 180-degree excitation, and a pulsed frequency-doubled 532 nm Nd:YAG laser used in an oblique (typically 135-degree) angle excitation.

One of the principal advantages of micro-Raman spectroscopy is the ability to make measurements on a region of a sample the same size as the focused laser spot. The laser can be focused to a diffraction limited spot such that the system will accept light from other areas such

as above and below the nominal focus area in an on-axis configuration (e.g. backscattering geometry). Insertion of a pinhole in the optical path in the image plane as shown in **Fig. 1.4** will make the Raman system confocal, allowing rejection of out of focus signal as well as spurious light from other sources. The 180-degree confocal microscope setup can map the sample in three dimensions. Use of 135-degree excitation geometry also avoids the generation of scattered light within the collection optics that may interfere with the weak light scattered from a sample.

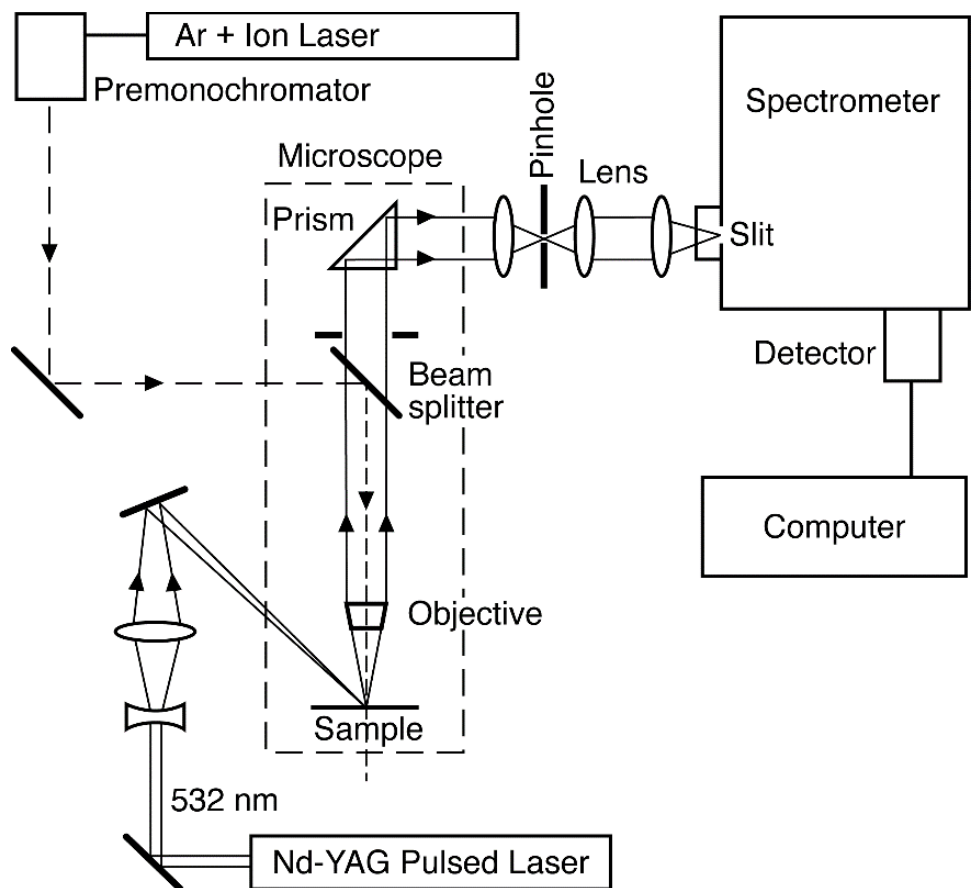


**Figure 1.4** Schematics of a confocal micro-Raman system with 180- and 135-degree scattering geometry with a CW Ar-ion laser and a pulse 532 nm laser, respectively.

Fully automated commercial confocal Raman instruments are available from many companies including HORIBA Instrument Inc. (Edison, NJ, USA), Renishaw inVia Raman microscope (Renishaw, Gloucestershire UK), WITec alpha300 confocal Raman system (WITec GmbH, Ulm, Germany), and F/1.8 RamanRXN microprobe (described by Battey 1993; Kaiser Optical Systems, Inc., Arbor, MI, USA). The inVia Raman microscope has the option of focusing the laser beam on a spot or line on the sample. The spectral image of the sample can be obtained by rastering the sample under the laser focus and moving from point to point on the sample until the desired area is mapped. By focusing the laser on a line rather than a spot, the resulting image can be focused on the slit and subsequently imaged on the CCD detector. The x-axis on the CCD will be the Raman shift and y-axis will show variation in the spectra of the sample. The line focus allows the use of higher laser power on the sample as compared to the point focus, and allows a faster spectral image of the sample as multiple points along the line are measured simultaneously.

Advances in notch and sharp edge filters have significantly reduced the size of the dispersive Raman systems. SuperNotch filters allows the rejection of the Rayleigh scattered light by a factor of  $\sim 10^8$ , thereby eliminating the need for a filter stage in modern Raman spectrometers. These advances have been used to develop research-grade miniature Raman spectrometers for space applications (Gasda et al. 2015; Wang et al. 1998) as well as commercial miniature Raman spectrometers (for a review see Dubessy et al. 2012).

#### **1.4.4.2 Advances in Remote Raman Instrumentation**

Telescopic Raman systems equipped with an intensified ICCD camera using 532 nm pulsed laser with 10-ns pulses have been developed for measuring time-resolved remote Raman spectra of minerals during daytime and nighttime (Lucey et al. 1998; Carter et al. 2005b; Misra et al. 2005; Sharma et al. 2005; Wiens et al. 2016). For a review, see Angel et al. (2012).

In recent years, remote Raman systems based on spatially heterodyne Raman spectrometer (SHRS) using both 532 nm and UV pulsed lasers are being developed for measuring time-resolved Raman spectra of both inorganic and organic compounds over a large area (e.g. Gomer et al. 2011; Lamsal et al. 2016). Using SHRS and 532 nm pulsed laser excitation, Egan et al. (2017) measured Raman spectra of feldspars and olivine minerals. These spectra show well-resolved Raman fingerprint modes of four-membered  $TO_4$  rings in microcline at 475, 484, and  $513\text{ cm}^{-1}$ , and in plagioclase at 481 and  $509\text{ cm}^{-1}$  (McKeown 2005; Freeman et al. 2008). The Raman fingerprints of olivine, which includes a doublet consisting of well-resolved lines at 824 and 855, have been observed with SHRS.

## **1.5 Raman Spectra of Planetary Ices and Geologic Materials**

### **1.5.1 Raman Spectra of Planetary Ices**

Raman spectroscopy can detect homopolar molecules such as  $H_2$ ,  $N_2$ ,  $O_2$ , etc..., which do not absorb in IR as well as heteropolar molecules. Raman spectrometry has been successfully adopted by a number of scientists for in-situ investigation of irradiated frozen ices containing organic molecules (Spinella et al. 1991; Ferini et al. 2004), and crystalline and amorphous water ice films on metal surfaces (Sonwalker et al. 1991). Micro-Raman techniques are used in the laboratories to study the effects of ion-induced lattice damage in carbonaceous solids and organic

compounds in frozen planetary ice analogs (Elman et al. 1981; Strazzulla & Baratta 1992; Strazzulla et al. 2001; Ferini et al. 2004). Bennett et al. (2013) developed a novel high-sensitivity Raman spectrometer to study pristine and irradiated interstellar ice analogs. These scientists measured in situ Raman spectra of thin films of CO<sub>2</sub> ices of 10 to 396 nm thickness at 4.5 K under ultrahigh vacuum. The Fermi resonance doublet of CO<sub>2</sub> ice was detected at 1385 and 1278 cm<sup>-1</sup>, which is in good agreement with previous studies. To evaluate the effect of irradiation on CO<sub>2</sub> ice, a CO<sub>2</sub>-ice film (450 nm thick) was deposited at 4.5 K and subjected to 1 h of irradiation from 5 keV electron beam over an area of 1.6 cm<sup>2</sup>. The Raman spectrum of the irradiated CO<sub>2</sub> film detected the presence of two new species, namely CO at 2145 cm<sup>-1</sup> and O<sub>2</sub> at 1545 cm<sup>-1</sup>, in the film (Bennett et al. 2013).

### **1.5.2 Raman Spectra of Geologic Materials**

Advances in the Raman instrumentation have enhanced the applications of Raman spectroscopy in nearly all geologic and planetary disciplines. Fluid inclusions in various geologic and extraterrestrial materials have been studied with Raman spectroscopy (Rosasco et al. 1975; Pasteris et al. 1986; Fries & Steele 2011; Frezzotti et al. 2012). The major strength of Raman spectroscopy in studying fluid inclusions is that the technique is capable of nondestructively analyzing single small (>5 μm) inclusions (Roedder 1984). Raman spectra of minerals, glasses, and melts of mineral compositions have also been investigated, as these provide information about short range and intermediate range structural orders (Sharma 1979a,b, 1981, 1985, 1988, 1996, 1997; Sharma & Simons 1981; Matson et al. 1983, 1986; Rai et al. 1983; Cooney & Sharma 1990; Wang et al. 1993, 1995).

Raman spectroscopy can provide structural information about minerals, glasses, and melts. For example, a comparative study of the Raman spectra silicate minerals and corresponding glasses led to reassignment of the two weak, sharp, and polarized peaks at 490 and 606  $\text{cm}^{-1}$  in the Raman spectrum of  $\text{SiO}_2$  glass (see **Fig. 1.5**). The 490 and 606  $\text{cm}^{-1}$  bands have been assigned, respectively, to symmetric stretching of oxygen atoms of four and three-membered rings of  $\text{SiO}_4$  tetrahedra in the disordered three-dimensional network (Sharma & Simmons 1981; Galeener et al. 1982a,b; McMillan & Wolf 1995 and references therein).

These ring modes are vibrationally decoupled from rest of the network, remaining highly localized within the rings, which explains their narrow width compared to the rest of the glass spectrum. A micro-Raman study of a new silica polymorph moganite, which contains four-membered rings of  $\text{SiO}_4$ , found a strong Raman band at 501  $\text{cm}^{-1}$  (Kingma & Hemley 1994; Götze et al. 1998; Nasdala et al. 2004). This observation further confirmed that the lines in the range 500 to 512  $\text{cm}^{-1}$  are the Raman fingerprints of the four-membered rings of tetrahedra in tectosilicate minerals, glasses, and melts of mineral compositions.

A number of scientists have reviewed extensive work on Raman spectroscopic investigations of the structure of silicate glasses and melts of interest in earth science (McMillan & Wolf 1995; McMillan et al. 1996; Nasdala et al. 2004; Mysen & Richet 2005; Rossano & Mysen 2012). The results of these investigations have had a profound effect on our understanding of magmatic processes.

Micro-Raman and confocal Raman instruments are being used for identification of mineral phases in rocks and meteorite samples (Haskin et al. 1997; Wang et al. 2001; Kuebler et al. 2006). For example, Acosta et al. (2013) used micro-Raman mapping of mineral phases in a thin section of a strongly shocked Taiban ordinary chondrite. The Raman spectra was excited with

various laser excitation wavelengths (e.g. 244, 514.5, 785, and 830 nm), which allowed identification of mineral phases such as olivine, wadsleyite, ringwoodite, high-Ca clinopyroxene, majorite-pyrope, jadeite, maskelynite, and lingunite. Olivine was found to be Fe depleted (Fo<sub>88</sub>) in contact with the ringwoodite as compared to olivine (Fo<sub>94</sub>) separated from ringwoodite grains, which suggests chemical fractionation during a solid-state olivine-ringwoodite transformation. Raman imaging revealed a close correlation between the blue ringwoodite color and the peak observed at 877 cm<sup>-1</sup>. This signal showed a strong near-resonance Raman enhancement when measured with near-IR laser excitations (785 and 830 nm) close to the optical absorption bands of four-fold coordinated Fe<sup>2+</sup> in the ringwoodite (Acosta et al. 2013). The near-IR optical absorption is assigned to the transition  ${}^5T_{2g} \rightarrow {}^5E_g$  of  ${}^{VI}Fe^{2+}$  split by the trigonal distortion or Jahn–Teller effect (Taran et al. 2009).

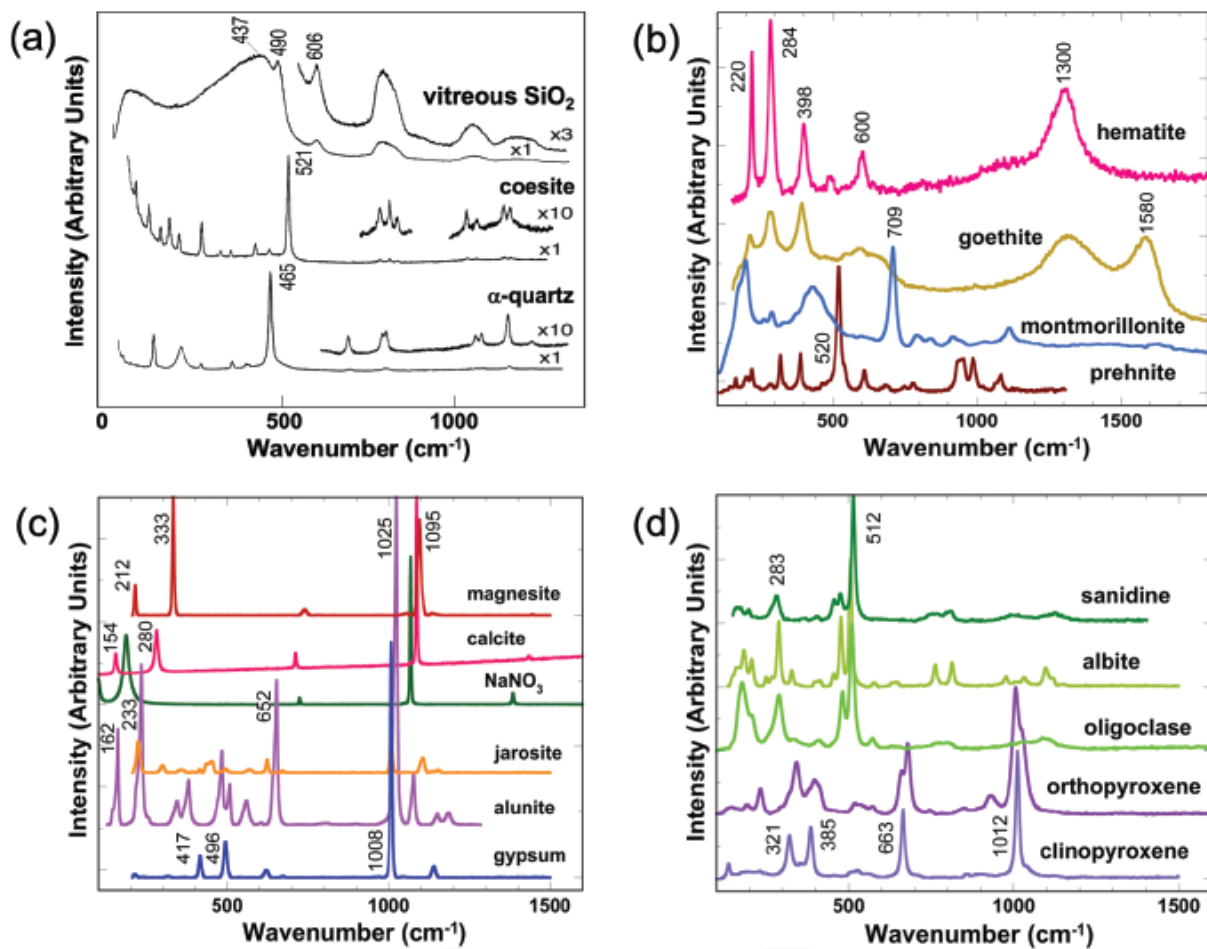


**Figure 1.5** Raman spectra of selected minerals. (a) spectra of  $\alpha$ -quartz, coesite and vitreous-SiO<sub>2</sub> (data from Sharma 1981), (b) spectra of iron oxides/hydroxides and phyllosilicates (data from Edwards 2004; Bishop & Murad 2004), (c) spectra of carbonates, nitrates and sulfates (data from Bishop 2017; RRUFF database: <http://rruff.info>), (d) spectra of feldspar and pyroxene minerals (data from Bishop & Murad 2014).

Micro-Raman spectroscopy has also been successfully used to investigate mineralogy and phase transitions under high pressure and temperature to gain insight into the Earth and planetary interiors (for reviews, see Hemley et al. 1987; Sharma 1989; Gillet 1993; McMillan et al. 1996; Gillet et al. 2000; Goncharov 2012; Reynard 2012).

## 1.6 Summary

In this chapter, we have introduced theory of Raman scattering based both on classical electrodynamics and quantized nature of the energy levels. Basic applications of group theory is discussed as it relates to the symmetry of the molecules and the crystal unit cells for prediction of number of Raman and IR active modes, and degree of polarization. For crystalline solids, the factor group and site group approaches allow qualitative description of the association of normal modes with the symmetry species. Advances in instrumentation have facilitated the application of Raman spectroscopy in a number of geological and planetary disciplines. Laboratory measurements on a variety of geological materials and planetary analogs with micro-Raman, confocal Raman, and small telescopic Raman systems with CW and pulsed-lasers are providing valuable reference datasets for nondestructively identifying minerals, disordered solids, fluids, glasses, and melts of mineral compositions. Miniaturization of Raman spectrometers with CCD, ICCD, and SPAD detectors and use of CW and pulsed-laser excitation sources have made Raman spectroscopy much more practical for identifying Earth and planetary materials. The development of online databases, such as RRUFF (<http://rruf.info>), is useful and valuable resources for Earth and planetary scientists.

## **Chapter 2. One Mirror, One Grating Spatial Heterodyne Spectrometer for Remote Sensing Raman Spectroscopy**

Recently, we evaluated a new type of Fourier transform Raman spectrometer, the spatial heterodyne Raman spectrometer (SHRS), that provides high-resolution spectra without the need for an entrance slit. A spatial heterodyne Raman spectrometer is a variant of a Michelson interferometer in which the mirrors in the arms of a Michelson interferometer are replaced by two stationary diffraction gratings. Instead of sampling path length differences temporally, as in the case of a Michelson interferometer, SHRS samples path length differences spatially at a 2D-array detector. Applying a Fourier transform to the resulting interferogram recovers the desired spectrum. In the modified SHRS (mSHRS) instrument used in the present work, one of the diffraction gratings has been replaced by a stationary  $\lambda/10$  mirror. This modification has a few effects. First, the detector records a greater number of photons as spectral light is not lost into unused diffraction orders in the mirror arm of mSHRS. Second, the free spectral range (bandpass) is doubled while the spectral resolution is cut in half. In this work, the authors present remote-sensing Raman spectra of minerals, organics and biomarkers using this mSHRS for the first time.

### **2.1 Development of Spatial Heterodyne Spectrometers for Planetary Science Applications**

Raman scattering is the natural phenomenon whereby light is inelastically scattered by molecular vibrations whose oscillations possess an instantaneous dipole moment. In a Raman scattering event, a photon imparts an amount of energy equal to a molecule's vibrational mode, leaving behind a molecule in an excited vibrational state and a photon whose energy loss equals

that vibrational energy gap (or vice versa). Recovery of the Raman scattered light yields a vibrational energy spectrum. Since every molecule has a unique set of vibrational modes, analysis of Raman spectra can be utilized to unambiguously identify a wide range of compounds, including minerals, organics and biomarkers.

In recent years, a wide range of authors (Jorge Villar & Edwards 2006; Edwards et al. 2005; Bishop & Murad 2004; Maurice et al. 2015; Beegle et al. 2014) have recognized Raman spectroscopy's ability to characterize such diverse materials, which in turn has led to the selection of Raman spectrometers, such as SuperCam, SHERLOC and ExoMars, for use in planetary surface exploration missions. Raman spectrometers intended for space flight must attain a minimum sensitivity, spectral resolution and free spectral range while being able to withstand extreme vibrations, pressures and temperatures incurred during spaceflight. Therefore, spectrometers that achieve high spectral resolution, wide free spectral range, and high throughput in compact, light footprint packages without moving components are desirable.

Recently, Harlander (Harlander 1991) developed a new type of spatial interferometer, called a spatial heterodyne spectrometer (SHS), which is capable of measuring high-resolution sparse emission and scattered light spectra in a compact, light footprint system. SHS is a variant of a Michelson interferometer in which the moving mirror of a Michelson is replaced by a stationary diffraction grating. When light enters SHS, it is reflected off diffraction gratings at wavenumber dependent angles that produce crossed wavefronts in space that can be imaged by a plane array detector. The crossed wavefronts, which represent a superposition of spatial interference fringes, are converted to a spectrum upon applying a Fourier transform. Since Harlander's pioneering work, SHS has been used for many applications, including the measurement of emission spectra and wind velocities in gas clouds (Harlander et al. 1993, 2004, 2002; Englert et al. 2010),

measurement of Raman spectra (Gomer et al. 2011; Lamsal et al. 2015, 2016; Strange et al. 2016; Hu et al. 2015; Barnett et al. 2017; Egan et al. 2017, 2018) of organics, inorganic salts and minerals, and laser-induced breakdown spectroscopy (Gornushkin et al. 2014) of brass alloys.

In 2014, Gornushkin (Gornushkin et al. 2014) published laser-induced breakdown spectra using a modified SHS. Using one grating instead of two in an SHS has a few effects. First, the detector records a greater number of photons, as light in the mirror arm is not diffracted into orders outside the field-of-view of the detector. Second, the bandpass of this modified SHS is doubled while the spectral resolution is cut in half. The instrument design used in this project achieves a  $4915 \text{ cm}^{-1}$  maximum bandpass, and a  $7.5 \text{ cm}^{-1}$  minimum full-width at half maximum of Raman spectral features. In this work, the authors present remote-sensing Raman spectra using mSHRS for the first time. The purpose of this work is to demonstrate the efficacy of using this mSHRS in measuring materials relevant to the planetary science community.

## 2.2 Design of a Modified Spatial Heterodyne Spectrometer

**Fig. 2.1** depicts the instrument utilized in this work. The excitation source used in this experiment was a pulsed, frequency-doubled neodymium-doped yttrium aluminum garnet (e.g. Nd:YAG) laser (Geusic et al. 1964; McClung & Hellwarth 1962), which produced 10 ns pulses of 532 nm light at 8.5 mJ per pulse and 100 Hz. Laser light was directed through an 8x beam expander, reflected off a plane mirror and sent to a sample. The diameter of the laser spot size at the sample location was 50 mm to measure the Raman spectrum of the large area of the sample and also reduce any sample damage by the laser beam.

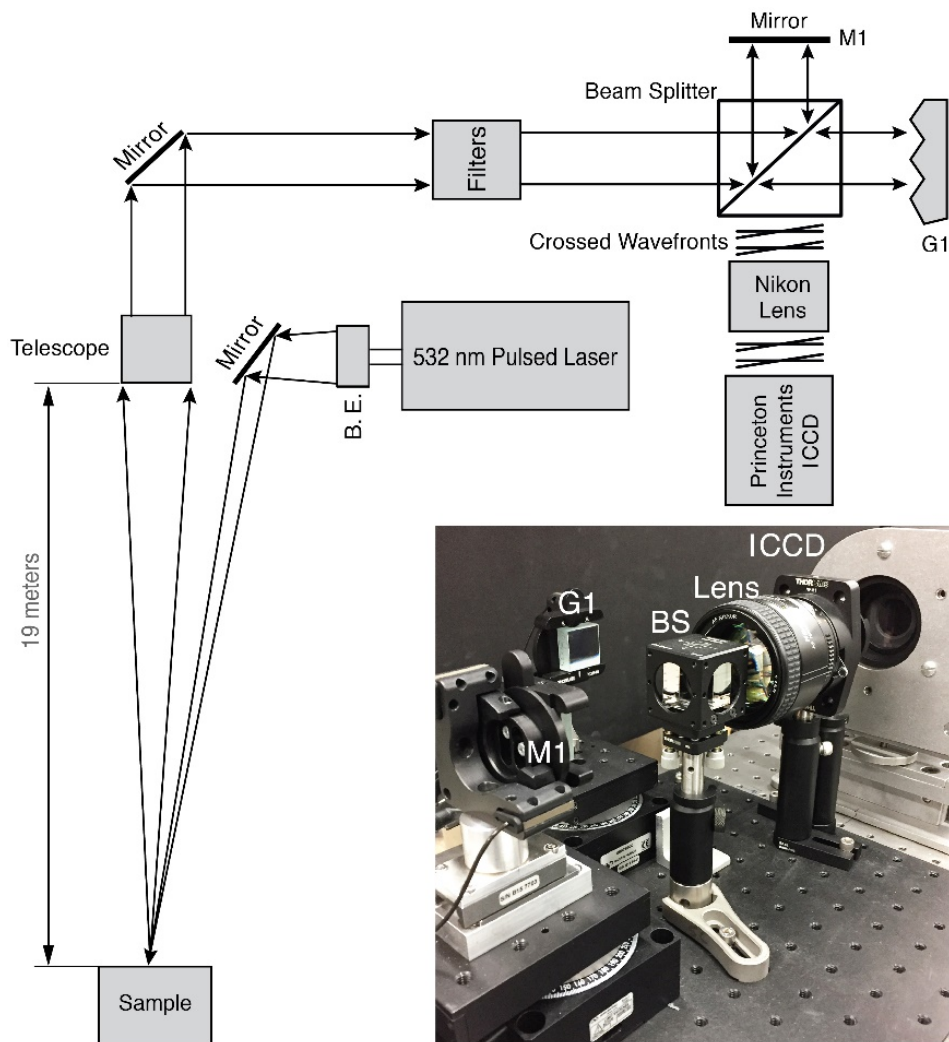


**Figure 2.1** A schematic diagram of the mSHRS used in this work.

Mineral samples were measured without cutting or polishing. Pure chemicals were sandwiched between one-foot square glass plates. The samples produced reflected and scattered light, and the Rayleigh and Raman scattered light was collected by a Questar telescope. The Questar telescope has a collection mirror 96.5 mm in diameter with a 25.4 mm central obstruction. The collected light was then collimated at infinity. The Rayleigh scattered light was attenuated by a 532 nm long-pass filters. Raman scattered light was permitted to enter the spatial

heterodyne interferometer whereafter the amplitude was divided 50/50 by a silica glass cube beam-splitter into two equidistant arms of the interferometer. In one arm of the interferometer, a  $\lambda/10$  plane mirror reflected incident light; in the other arm, a 150 groove per mm diffraction grating diffracted light at wavenumber-dependent angles, thus creating path length differences that can be sampled at the output of the interferometer. The angle at which the diffraction grating will diffract incident light is governed by the grating equation, as shown in Eq. (2.1)

$$d(\sin \theta_i + \sin \theta_r) = m\sigma \quad (2.1)$$

where  $\sigma$  is the wavenumber of incident light,  $m$  is the order of diffraction,  $d$  is the groove density per centimeter,  $\theta_i$  is the angle of incident light, and  $\theta_r$  is the angle of reflected light. A special case, called the Littrow condition, is attained when the angle of incidence (e.g.  $\theta_i$ ) equals the angle of reflectance (e.g.  $\theta_r$ ), as described by Eq. (2.2)

$$\theta_L = \sin^{-1} \left( \frac{m\sigma_0}{2d} \right) \quad (2.2)$$

where  $\theta_L$  is the Littrow angle and  $\sigma_0$  is the wavenumber of light whose angle of incidence and reflectance upon the diffraction grating are equal. In the Littrow condition,  $\sigma_0$  is retro-reflected from the grating, producing a planar wavefront of constant intensity across the fiber-coupled intensified charge-coupled device (ICCD). Wavenumbers not equal to  $\sigma_0$  are diffracted at angles relative to the optical axis, which recombine as crossed wavefronts in space at the beam-splitter, producing cosinusoidal spatial fringes when imaged by the ICCD as described by Eq. (2.3)

$$I(x, y) = \int_0^\infty B(\sigma)(1 + \cos[2\pi(2(\sigma - \sigma_0)x \tan \theta_L + \sigma y \alpha)])d\sigma \quad (2.3)$$

where  $B(\sigma)$  represents the input spectral intensity as a function of wavenumber,  $\alpha$  represents a slight tilt in the grating about its x-axis, x and y represent a given location within the two-

dimensional plane array detector, and the wavenumber of a spatial fringe along the x and y axes are defined by Eq. (2.4) and (2.5), respectively.

$$f_x = 2(\sigma - \sigma_0) \tan(\theta_L) \quad (2.4)$$

$$f_y = \sigma\alpha \quad (2.5)$$

The crossed wavefronts at the output of the beam-splitter are focused by a Nikon f/1.8D camera lens and recorded by a Princeton Instruments fiber-coupled ICCD. Interferograms are measured in 30 ns gate exposures, which permits the acquisition of interference patterns generated by the Raman scattered light yet severely limits the contribution of ambient light to the resulting image. Finally, the Raman spectrum is recovered after applying several steps as described in a previous paper (Egan et al. 2018), including apodization of the interferogram, application of the Fourier transform upon the interferogram, phase correction of the FT by Mertz's method (Mertz 1967), intensity calibration by modeling the wavenumber-dependent intensity distribution of the shot noise, and windowing the regions of the FT that contain Raman peaks.

### 2.3 Samples

The rock-forming minerals used as samples in this work (e.g. plagioclase, forsterite, gypsum, anhydrite, milky quartz, dolomite, barite, calcite, and  $\alpha$ -quartz) were purchased from Ward's Natural Science Establishment, Inc. (Rochester, NY, USA). The carbonate minerals calcite and dolomite were, respectively, from Chihuahua, Mexico, and Bamble, Norway. The sulfate minerals barite, anhydrite and gypsum samples were, respectively, from Potosi, Missouri, USA, Windsor Nova Scotia, Canada, and Washington County, Utah, USA. The silicate minerals

plagioclase, forsterite, milky quartz and  $\alpha$ -quartz were sourced from Crystal Peak, Colorado, USA, Jackson County, North Carolina, USA, Dekalb, New York, USA, and Hot Springs, Arkansas, USA, respectively. Electron microprobe analysis of the plagioclase sample determined that the phase composition of the sample was  $Ab_{70.09}An_{21.18}Or_{2.78}$  where Ab = albite ( $NaAlSi_3O_8$ ); An = anorthite ( $CaAl_2Si_2O_8$ ); and Or = orthoclase ( $KAlSi_3O_8$ ). The composition of the sample called forsterite was found to be  $Fo_{91}Fa_9$  where Fo = forsterite ( $Mg_2SiO_4$ ) and Fa = fayalite ( $Fe_2SiO_4$ ). Finally, samples of analytical grade chemical compounds, such as  $KClO_3$ , naphthalene and urea, were prepared by placing said sample between two one-foot square glass plates.

## **2.4 Experimental Results**

### **2.4.1 Raman Spectra of Minerals, Salts and Organics as Measured by mSHRS**

The identification of minerals, organics and biomarkers on planetary surfaces is vitally important to the understanding of the chemical evolution of said planets since chemical substances require specific environmental conditions to be present in order to materialize. Therefore, characterization of minerals, organics and biomarkers yields insight into the prevailing environmental conditions in the past. For example, identification of the composition of olivine serves as an indicator (Christensen et al. 2005) of the degree of silica saturation of primitive, mantle derived magmas, and as a proxy to the prevalence of aqueous environments via quantifying the degree of weathering a given olivine sample has undergone. Hence, characterization of a particular phase of olivine present in a given locale yields information pertaining to the bulk composition of a planet as well as the prevalence of water throughout its

history. In a recent study, Hoefen (Hoefen et al. 2003) characterized the compositional variation of olivine within the Nili Fossae region of Mars using thermal emission spectroscopy and found that forsterite compositions ranged from Fo<sub>30</sub> to Fo<sub>70</sub>. Importantly, Raman spectroscopy is capable of identifying a particular phase of forsterite by careful analysis of the peak centers of the olivine doublet (Breitenfeld et al. 2018) between 800 and 880 cm<sup>-1</sup>. Likewise, characterization of other minerals yields valuable information as well, such as determination of the bulk composition of radioactive <sup>26</sup>Al by quantification of feldspar composition (Milam et al. 2010), determination of the prevalence of aqueous environments and pH by quantification of evaporitic minerals such as carbonate (Bridges 2001; Brown 2018) and sulfate (Gendrin et al. 2005; Nachon et al. 2014) minerals, etc...

In the following section, the authors present Raman spectra of minerals, organics and biomarkers obtained by mSHRS at remote-sensing distances of 3 to 19 meters. In all spectra presented in this section, the laser energy was 8.5 mJ per pulse, the pulse rate was 100 pulses per second, the laser spot size at the sample was 50 mm in diameter, the ICCD's intensifier gain was set to maximum, and the total accumulation time was 10 seconds. Raman photons are collected over the entire extent of the 50 mm in diameter laser spot.

In **Fig. 2.2**, the Raman spectra of plagioclase and forsterite are presented as measured by mSHRS at 3 meters. The characteristic Raman vibrational mode of plagioclase (McKeown 2005; Freeman et al. 2008) is the doublet that occurs at 479 and 508 cm<sup>-1</sup> caused by the ring breathing motions within the four-membered rings of TO<sub>4</sub> tetrahedra where T equals Si or Al. In an earlier work, the authors (Egan et al. 2017) demonstrated SHRS' ability to differentiate between different phases of feldspars. The fingerprint band for forsterite (Lam et al. 1990; Kuebler et al.

2006) is the doublet occurring at 824 and 855  $\text{cm}^{-1}$ , where the olivine doublet originates from the mixing of the symmetric and antisymmetric stretching of  $\text{Si-O}_{\text{non-bridging}}$  bonds of  $\text{SiO}_4^{4-}$  anions.

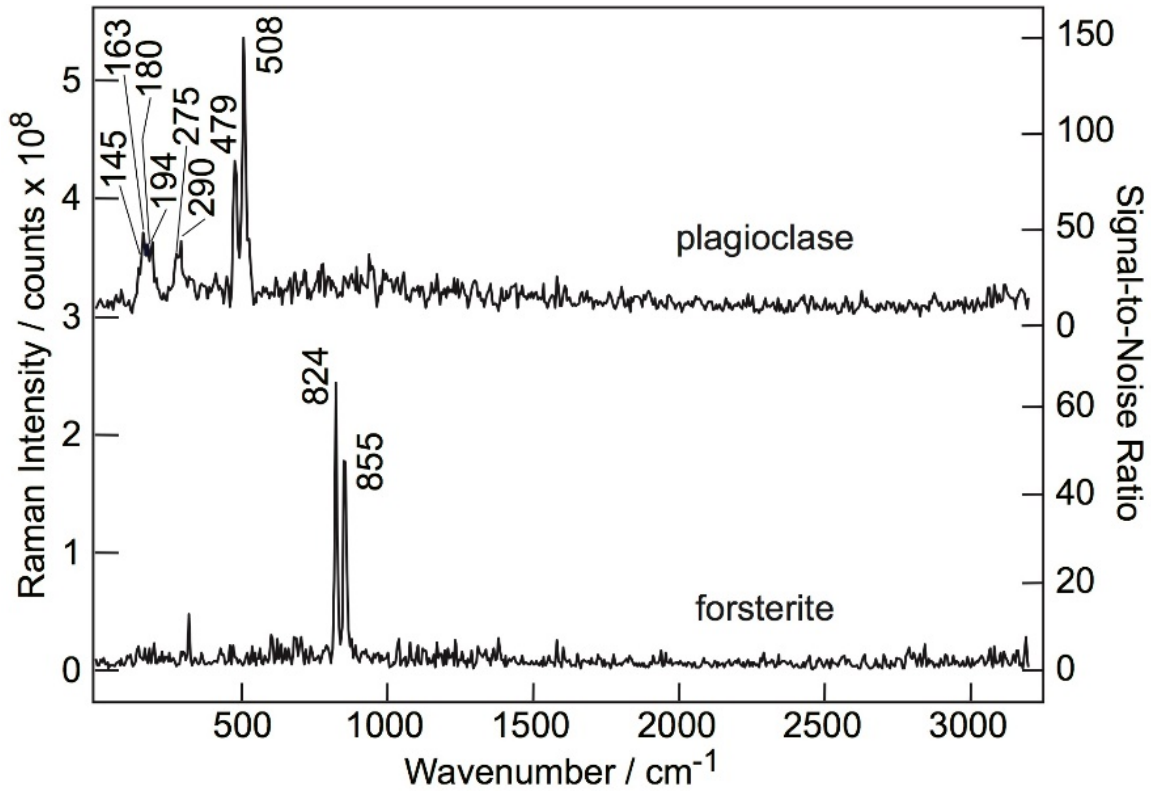


**Figure 2.2** The Raman spectra of plagioclase and forsterite as recorded by mSHRS at 3 meters distance. The Littrow angle was set to retro-reflect 554 nm ( $\sim 744 \text{ cm}^{-1}$ ) light.

The effective free spectral range of mSHRS used in this work was determined by precisely calibrating the x-axis with known Raman peak positions, and thereafter calculating the difference in wavenumber between the first and last bins within the spectral array. The maximum effective bandpass was found to be  $4915 \text{ cm}^{-1}$ . In a similar manner, the effective spectral resolution was determined by curve fitting real spectral peaks presented in this article. The authors found that the peak with the narrowest linewidth occurred in the forsterite spectrum at  $824 \text{ cm}^{-1}$ , which had a full-width at half maximum of  $7.5 \text{ cm}^{-1}$ .

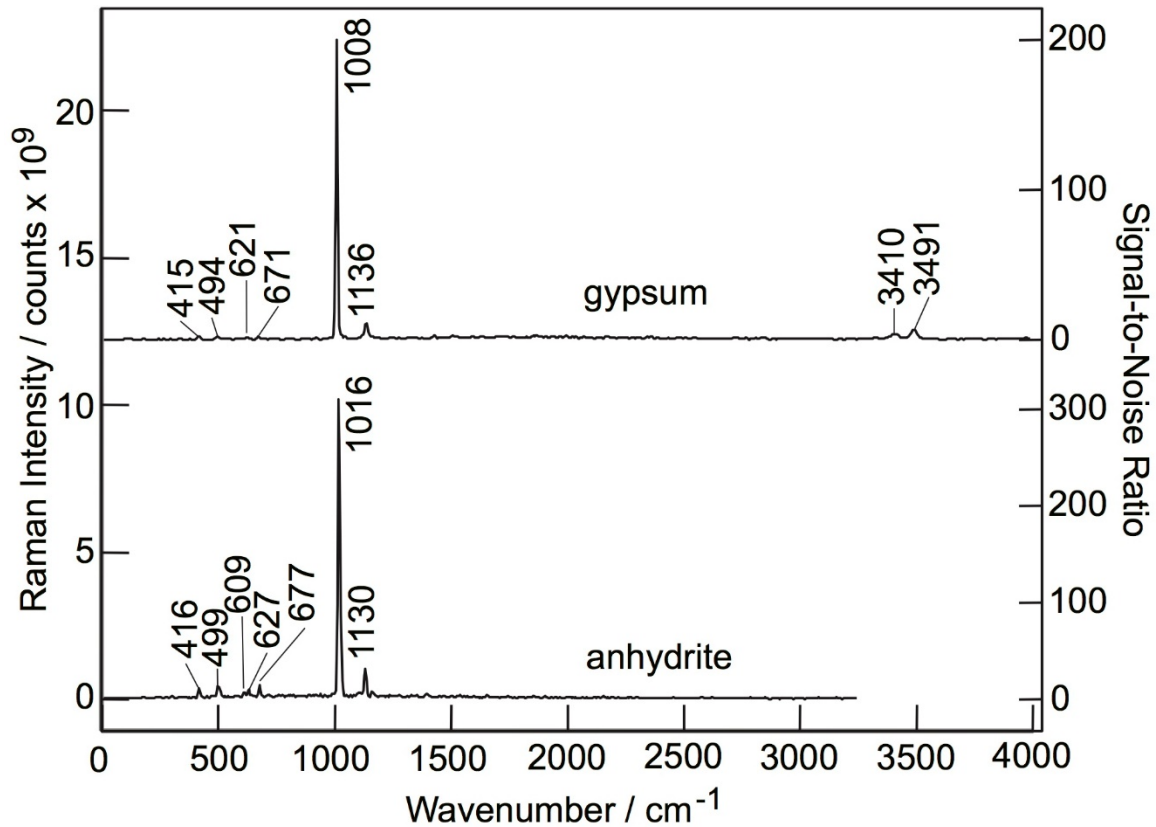


**Figure 2.3** The Raman spectra gypsum and anhydrite as recorded by mSHRS at 3 meters distance. The Littrow angle for gypsum and anhydrite was set to 584 nm ( $\sim 1671 \text{ cm}^{-1}$ ) and 554 nm ( $\sim 744 \text{ cm}^{-1}$ ), respectively.

In **Fig. 2.3**, the Raman spectra of calcium sulfate minerals (Chio et al. 2004) gypsum and anhydrite are presented as measured by mSHRS at 3 meters distance. The characteristic vibrational modes of both gypsum and anhydrite result from the vibrational motions of the sulfate anion. The strongest peak in each spectrum results from the symmetric stretch ( $\nu_1$ ) of the sulfate anion. Symmetric bending motions account for the modes present in the  $400 \text{ cm}^{-1}$  to  $500 \text{ cm}^{-1}$  region while antisymmetric bending motion account for the modes in the  $600 \text{ cm}^{-1}$  to  $700 \text{ cm}^{-1}$  region. Lastly, gypsum contains two water molecules that give rise to the peaks occurring at  $3410$  and  $3491 \text{ cm}^{-1}$ . The Raman peaks of water (Walrafen 1964) within gypsum shown here are

a superposition of the symmetric stretching mode ( $\nu_1$ ), the antisymmetric stretching mode ( $\nu_3$ ), and an overtone of the symmetric bending mode ( $2\nu_2$ ).

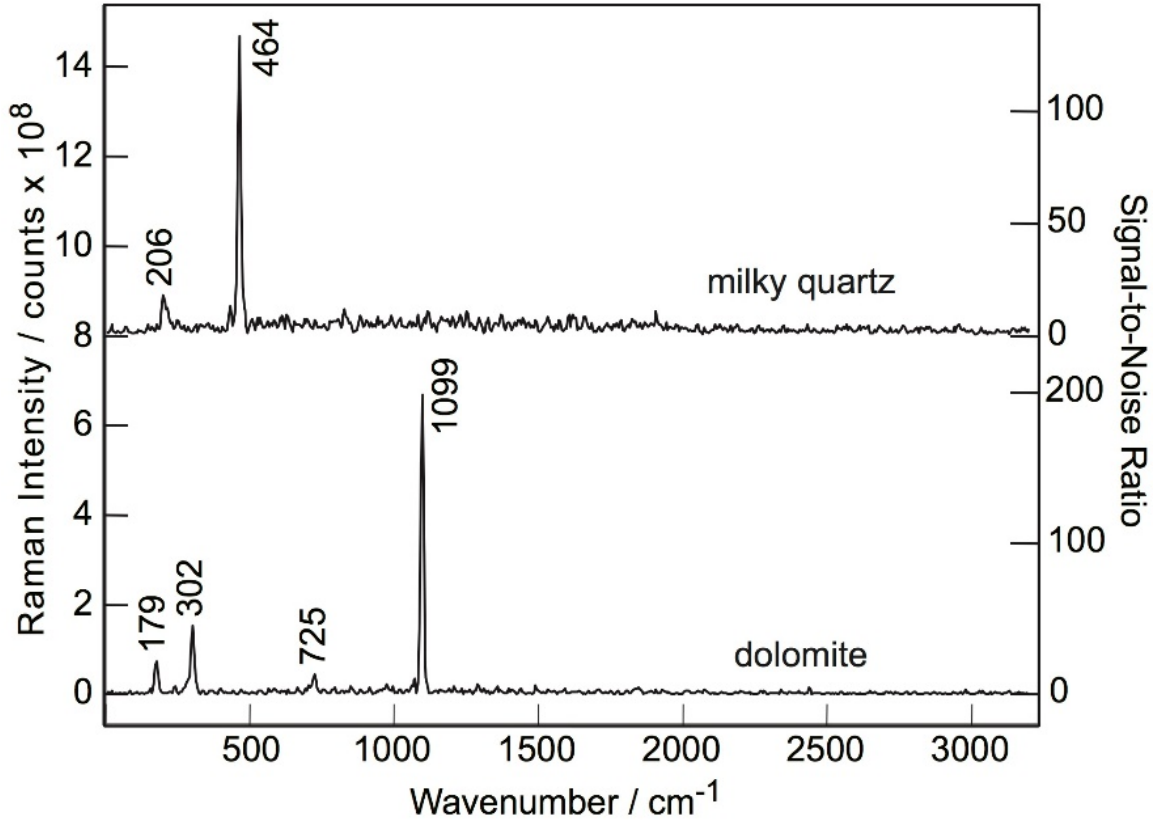


**Figure 2.4** The Raman spectra of milky quartz and dolomite as recorded by mSHRS at 10 meters. The Littrow angle for both minerals was set to retro-reflect 554 nm ( $\sim 744\text{ cm}^{-1}$ ) light.

In **Fig. 2.4**, the Raman spectra of milky quartz (Sharma & Simons 1981) and dolomite (Bischoff et al. 1985) as measured by SHRS at 10 meters are presented. The Raman spectrum of milky quartz shown here contains two Raman fingerprints, one appearing at 206 and 464  $\text{cm}^{-1}$ , which is attributable to a soft lattice mode and a strong six-member ring breathing mode of  $\text{SiO}_4$  tetrahedra, respectively. In the dolomite Raman spectrum, four peaks are clearly evident. The two lowest wavenumber modes are the result of long-range lattice vibrations while the peaks at

725 and 1099  $\text{cm}^{-1}$  result from the antisymmetric bending ( $\nu_4$ ) and symmetric stretching ( $\nu_1$ ) of the sulfate anion, respectively.

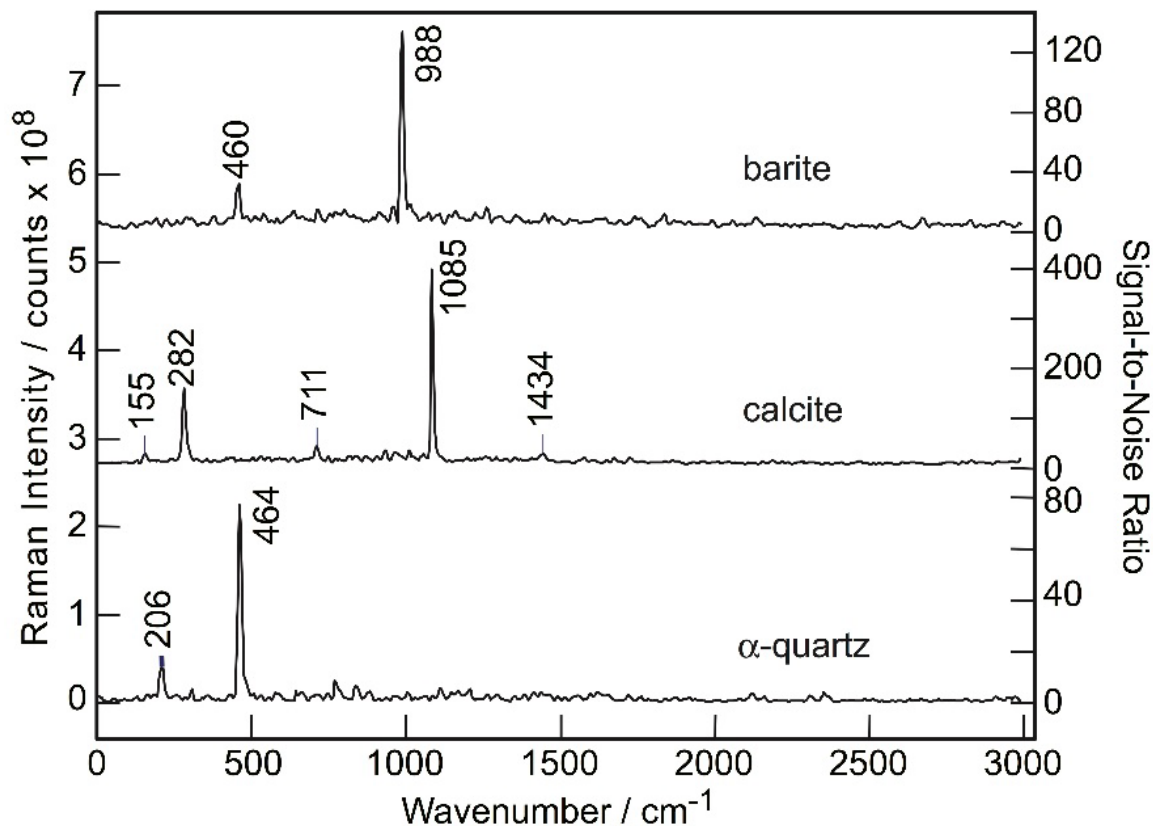


**Figure 2.5** The Raman spectra of barite, calcite, and  $\alpha$ -quartz as recorded by mSHRS at 19 meters. The Littrow angle for all minerals was set to retro-reflect 554 nm ( $\sim 744 \text{ cm}^{-1}$ ) light.

In **Fig. 2.5**, the Raman spectra of three minerals, barite (Misra et al. 2006), calcite (Bischoff et al. 1985) and  $\alpha$ -quartz (Sharma & Simons 1981), are presented as measured by mSHRS at 19 meters. The spectrum of barite displays two peaks, one at 460  $\text{cm}^{-1}$  attributable to a symmetric bending motion ( $\nu_2$ ) of the sulfate anion and another peak at 988  $\text{cm}^{-1}$  caused by the symmetric stretching motion ( $\nu_1$ ) of the sulfate anion. Five modes appear in the Raman spectrum of calcite shown in **Fig. 2.5**. Two lattice modes of vibration appear at 155 and 282  $\text{cm}^{-1}$ , an antisymmetric

bending motion ( $\nu_4$ ) at  $711\text{ cm}^{-1}$ , a symmetric stretch of the carbonate anion ( $\nu_1$ ) at  $1085\text{ cm}^{-1}$  and an antisymmetric stretch ( $\nu_3$ ) of the carbonate anion at  $1444\text{ cm}^{-1}$ . The spectrum of  $\alpha$ -quartz contains the same vibrational modes as those described earlier in this article.

Potassium chlorate (Hanley et al. 2012; Ming et al. 2014; Leshin et al. 2013), naphthalene (Srivastava & Singh 2007) and urea (Rousseau et al. 1998) are important organic and biomarker molecules that may have played an important role in the production of biological materials on other planets, if any ever existed. Potassium chlorate may serve as a pH buffer in aqueous solution; naphthalene is the simplest polycyclic aromatic hydrocarbon, a category of molecules that many authors speculate may have played a vital role in producing a wide variety of organic molecules necessary for life; urea is one of the simplest biomarkers identified within carbonaceous chondrites and a molecule whose presence is known to favor the polymerization of amino acids into peptides.

In **Fig. 2.6**, the Raman spectra of potassium chlorate (i.e.  $\text{KClO}_3$ ), naphthalene and urea are presented. The Raman spectrum of potassium chlorate consists of four peaks pertaining to the oscillations of the chlorate anion: a symmetric bending motion ( $\nu_2$ ) at  $487\text{ cm}^{-1}$ , an antisymmetric bending motion ( $\nu_4$ ) at  $616\text{ cm}^{-1}$ , a symmetric stretching motion ( $\nu_1$ ) at  $938\text{ cm}^{-1}$ , and an antisymmetric stretching motion ( $\nu_3$ ) at  $976\text{ cm}^{-1}$ . The vibrational modes of naphthalene include the C-C-C bending motion at  $514\text{ cm}^{-1}$ , a ring-breathing motion at  $764\text{ cm}^{-1}$ , a C-C stretch at  $1021\text{ cm}^{-1}$ , a ring deformation and C-C stretch at  $1382\text{ cm}^{-1}$ , a C-H bending and C-C stretching motion at  $1464\text{ cm}^{-1}$ , an in-phase C=C stretch at  $1577\text{ cm}^{-1}$  and C-H stretch at  $3056\text{ cm}^{-1}$ . The Raman spectrum of urea contains a C-N symmetrical stretching vibration ( $\nu_1$ ) at  $1010\text{ cm}^{-1}$  and a symmetric bending motion ( $\nu_2$ ) at  $548\text{ cm}^{-1}$ .

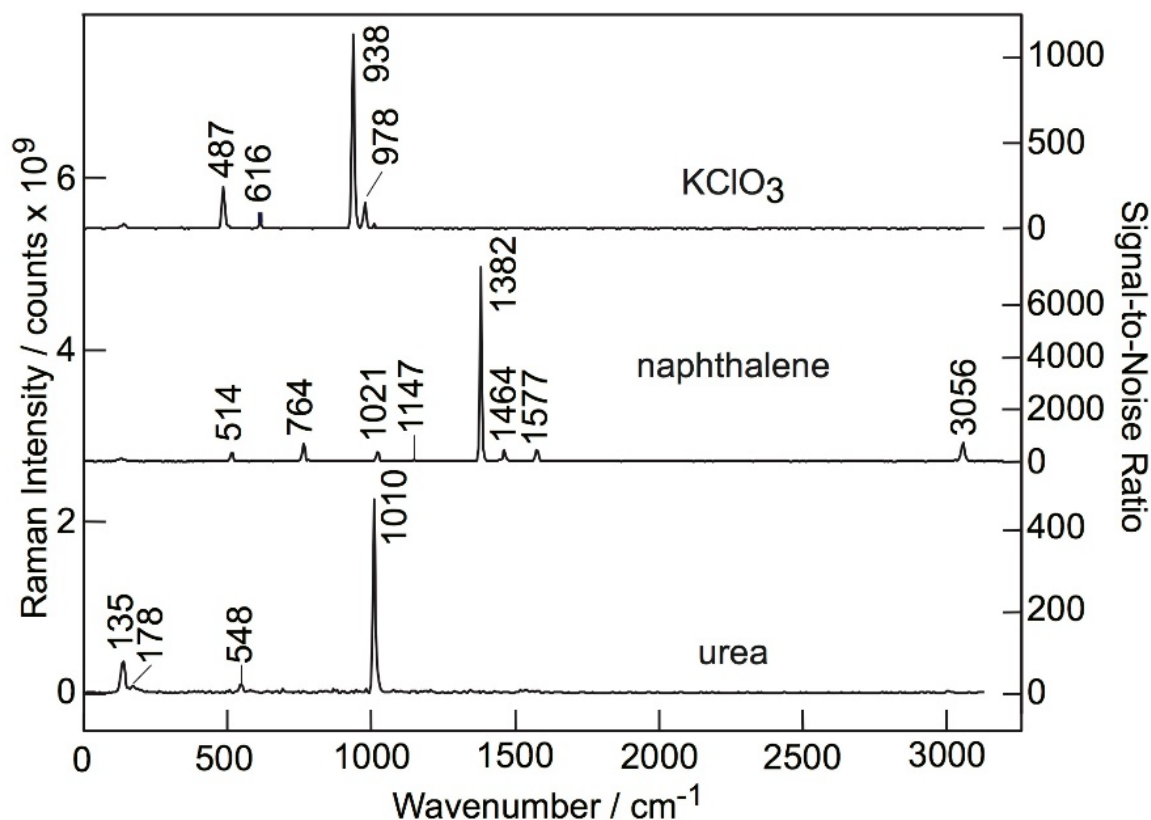


**Figure 2.6** The Raman spectra of  $\text{KClO}_3$ , naphthalene, and urea as recorded by mSHRS at 19 meters. The Littrow angle for  $\text{KClO}_3$  and urea was set to retro-reflect 554 nm ( $\sim 744 \text{ cm}^{-1}$ ) light, and the Littrow angle for naphthalene was set to retro-reflect 584 nm ( $\sim 1671 \text{ cm}^{-1}$ ) light.

## 2.4.2 Other Applications of mSHRS

In addition to the mineral, salt and organic compounds already discussed, we measured a variety of compounds commonly found in industrial commercial products, specifically saturated alkanes, cyclical hydrocarbons, and members of the benzene, toluene, ethylbenzene, and xylene (BTEX) class of compounds. The purpose of this section is to demonstrate that the modified SHRS can unambiguously identify these compounds that are essential to industry and maintaining living standards and yet toxic to living things.

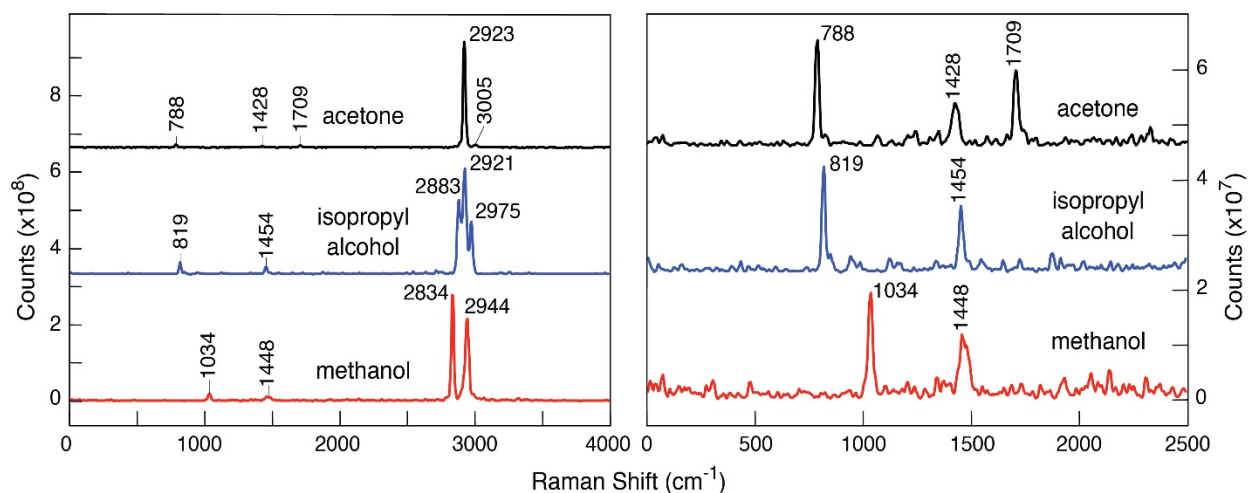


**Figure 2.7** The Raman spectra of three organic calibration targets as measured by SHRS at a distance of 19 meters from the telescope. The Littrow angle was set to retro-reflect 595 nm light in order to maximize SHRS’s sensitivity to the C-H stretching region and the Raman fingerprint region (e.g.  $<1800\text{ cm}^{-1}$ ). The accumulation time was 10 seconds. The left panel shows the complete spectra of these three organic compounds while the right panel is windowed to highlight the Raman bands in the fingerprint region of the same spectra.

The Raman spectra of three simple organics – acetone ( $(\text{CH}_3)_2\text{CO}$ ), isopropyl alcohol ( $(\text{CH}_3)_2\text{CHOH}$ ) and methanol ( $\text{CH}_3\text{OH}$ ) are presented in **Fig. 2.7**. These organic compounds are frequently used to calibrate Raman spectra owing to their high Raman scattering efficiencies and sharp Raman peaks. The Raman peaks illustrated here match those published in the literature (Mammone et al. 1980; Shimanouchi 1972) to within the  $\pm 2\text{ cm}^{-1}$  accuracy of SHRS. The most prominent features in these spectra are the C-H stretching modes that occur between 2800 and  $3000\text{ cm}^{-1}$ . In these spectra, the symmetric stretching mode of the methyl groups can be seen at 2923, 2883, and  $2834\text{ cm}^{-1}$  for acetone, isopropyl alcohol, and methanol, respectively. In addition, anti-symmetric C-H stretching vibrations appear at  $2944\text{ cm}^{-1}$  for methanol, and at 2921 and  $2975\text{ cm}^{-1}$  for isopropyl alcohol. At lesser energies, C- $\text{CH}_3$  in-plane deformations give rise to

Raman peaks at 1428 and 1454  $\text{cm}^{-1}$  for acetone and isopropyl alcohol, and C-O symmetric stretches appear at 1709, 1033, and 819  $\text{cm}^{-1}$  for acetone, methanol, and isopropyl alcohol, respectively, where the C-O stretch of acetone occurs at a higher frequency due to the greater electron density shared between carbon and oxygen atoms in a C=O bond as opposed to a C-OH bond.

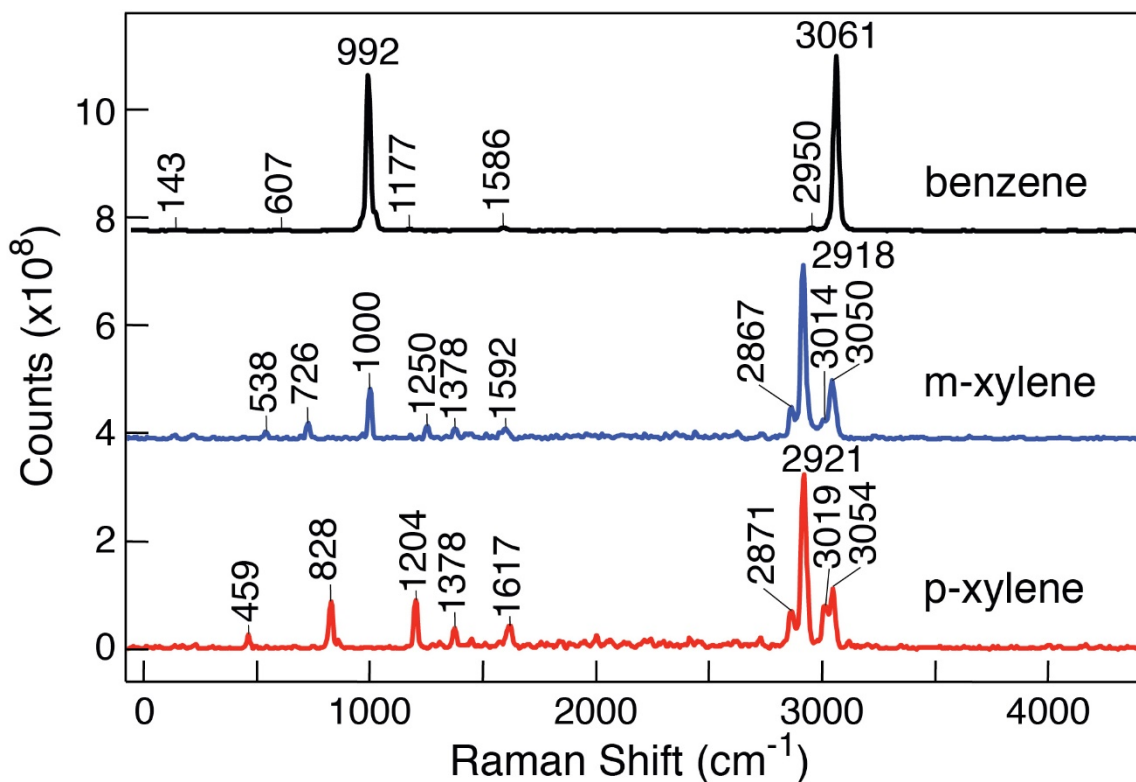


**Figure 2.8** The Raman spectra of three aromatic hydrocarbons, benzene, m-xylene and p-xylene, as measured by SHRS 19 meters from the collecting optic.

The Raman spectra of three organic liquids are presented in **Fig. 2.8**: benzene ( $\text{C}_6\text{H}_6$ ); m-xylene ( $\text{C}_6\text{H}_4(\text{CH}_3)_2$ ); and p-xylene ( $\text{C}_6\text{H}_4(\text{CH}_3)_2$ ). These aromatic hydrocarbons were selected for inclusion in this study due to the enormous consumption of these compounds by industry in the production of polyester fibers and resin as well as their importance in the petroleum industry

as either contaminants (e.g. benzene) or anti-knock agents (e.g. xylenes). These spectra demonstrate the efficacy of Raman spectroscopy in distinguishing between closely related species on the basis of minute changes in the chemical environment. The spectral features (Shinamouchi 1972; Lindenmaier et al. 2017) in **Fig. 2.8** may be separated into two regions of interest. The first region occurs between 2800 and 3100  $\text{cm}^{-1}$  and is the result of carbon-hydrogen stretching vibrations. The second region lies between 400 and 1700  $\text{cm}^{-1}$  and is made up of two components, specifically, carbon-carbon ring vibrations and carbon-hydrogen bending motions. Benzene's two most prominent features occur at 992 and 3061  $\text{cm}^{-1}$ , caused by the symmetric stretching of the aromatic ring and the symmetric stretching of carbon-hydrogen bonds, respectively. The Raman spectra of xylenes is more intricate than that of benzene because the methyl functional groups attached to the aromatic ring reduces the symmetry of the molecule, leading to changes in the symmetry-allowedness of normal modes of vibration. The symmetric carbon-hydrogen stretch found in benzene at 3061  $\text{cm}^{-1}$  arises at 3050 and 3054  $\text{cm}^{-1}$  for m-xylene and p-xylene, respectively. The other features measured in the carbon-hydrogen stretching region of xylenes when viewing the figure from left to right may be attributed to out-of-phase methyl symmetric C-H stretch, in-phase symmetric methyl C-H stretch, and an in-plane interior ring C-H stretch. The most conspicuous element of the Raman spectra of m-xylene and p-xylene is the presence of a ring-breathing mode at 1000  $\text{cm}^{-1}$  in m-xylene's spectrum that is absent in p-xylene's spectrum. The absence of this band in p-xylene's spectrum is caused by a change in the point group of the molecule, which, in consultation with the appropriate point group, makes that particular peak symmetry forbidden in p-xylene's spectrum according to well-known selection rules (Lindenmaier et al. 2017).

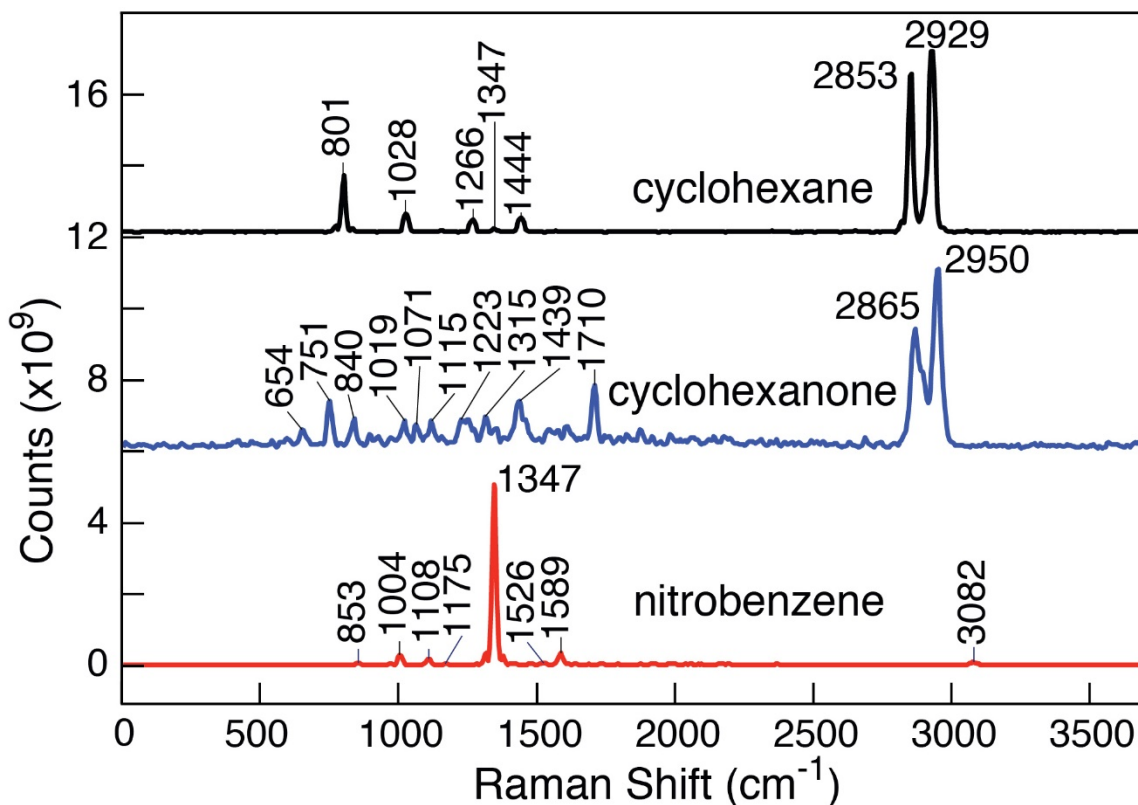


**Figure 2.9** The Raman spectra of three cyclical hydrocarbons (e.g., cyclohexane, cyclohexanone and nitrobenzene) as measured by SHRS at a distance of 19 meters from the telescope. The Littrow angle was set to retro-reflect 562 nm light so as to maximize the sensitivity of SHRS to peaks near  $1000\text{ cm}^{-1}$ . The accumulation time was 10 seconds.

The Raman spectra of three cyclic organic compounds – cyclohexane ( $\text{C}_6\text{H}_{12}$ ), cyclohexanone ( $\text{C}_6\text{H}_{10}\text{O}$ ) and nitrobenzene ( $\text{C}_6\text{H}_5\text{NO}_2$ ) – are depicted in **Fig. 2.9**. The spectrum of cyclohexane is comprised (Shimanouchi 1972) of three categories of vibrational motions, including C-C stretches at  $801$  and  $1028\text{ cm}^{-1}$ ,  $\text{CH}_2$  twists, wags and scissor motions occurring at  $1266$ ,  $1347$  and  $1444\text{ cm}^{-1}$ , and C-H stretches appearing at  $2853$  and  $2929\text{ cm}^{-1}$ . The Raman peak of cyclohexane shown at  $2929\text{ cm}^{-1}$  is not itself a true Raman peak but rather a convolution of two unresolved C-H antisymmetric stretches that should appear at  $2323$  and  $2938\text{ cm}^{-1}$ . The Raman

spectrum of cyclohexanone (Fuhrer et al. 1972) is more intricate than that of cyclohexane because the ketone functional group bonded to the hexagonal ring reduces the symmetry of the molecule and brings about a change in distribution of electron density within the ring, thus leading to a greater variety of vibrational modes seen in its spectrum. The most characteristic Raman mode of the cyclohexanone spectrum occurs at  $1710\text{ cm}^{-1}$ , which is caused by the symmetric stretching of the ketone group. Other features include the C-H stretches arising between  $2800$  and  $3000\text{ cm}^{-1}$ ,  $\text{CH}_2$  motions occurring between  $1200$  and  $1500\text{ cm}^{-1}$ , and C-C motions appearing between  $600$  and  $1200\text{ cm}^{-1}$ . Lastly, the Raman spectrum of nitrobenzene (Clarkson & Smith 2003), shown in **Fig. 2.9**, contains the  $\text{NO}_2$  symmetric stretch and bend at  $1347$  and  $853\text{ cm}^{-1}$ , respectively, along with a C-N stretch at  $1108\text{ cm}^{-1}$ .

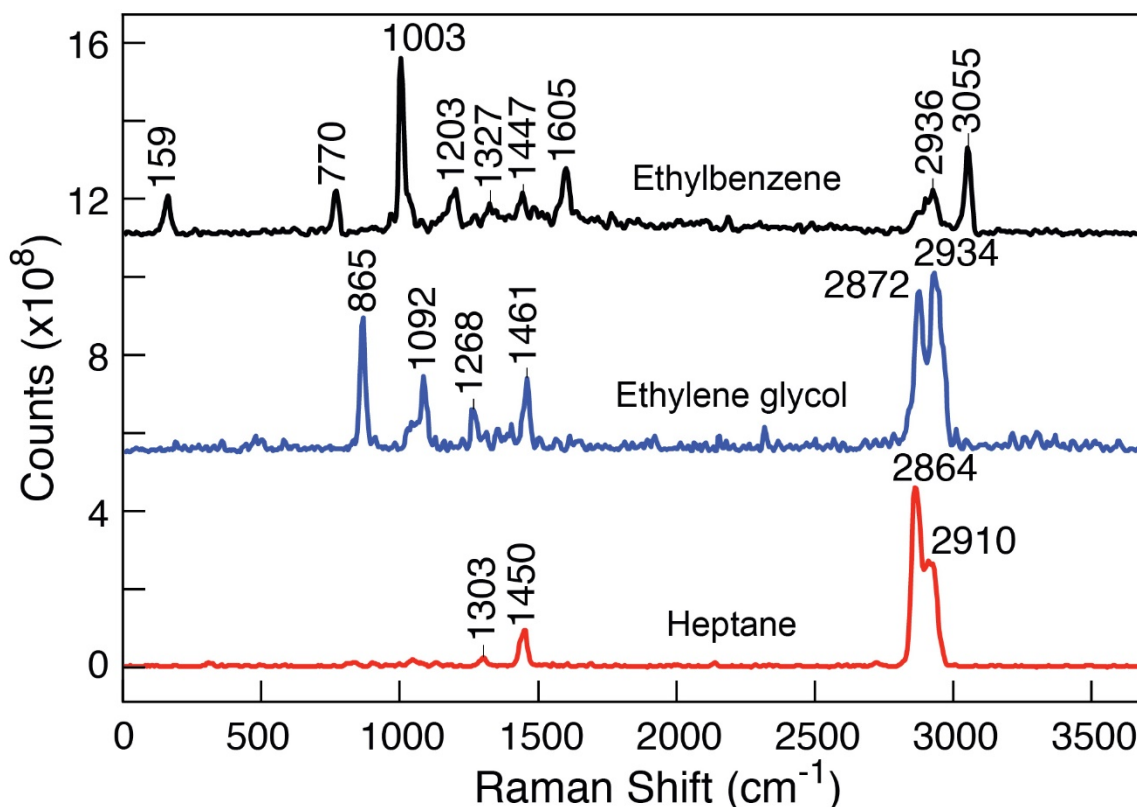


**Figure 2.10** The Raman spectra of three common constituents in hydrocarbon energy sources as measured by SHRS at a range of 19 meters from the collecting optic.

The Raman spectra of ethylbenzene ( $C_6H_5CH_2CH_3$ ), ethylene glycol ( $(CH_2OH)_2$ ) and heptane ( $C_7H_{16}$ ) are illustrated in **Fig. 2.10**. Ethylbenzene and ethylene glycol are common contaminants found in carbohydrate energy sources and other industrial products, making their identification important for commercial purposes. Heptane is commonly found in petroleum products as well as playing a vital role in the formation of cell membranes, micelles and biomarkers. The authors show how SHRS can be used to disentangle chemical contaminants from desired chemical constituents, such as ethylbenzene from heptane, by using SHRS. The vibrational mode assignments (Shimanouchi 1972; Krishnan & Krishnan 1966; Ma et al. 2011) for these spectra follow the same general trends as the previous figures. Once again, the C-H stretches are found near  $3000\text{ cm}^{-1}$ , C-H bending motions occur between  $1200$  and  $1650\text{ cm}^{-1}$ , and the C-C vibrations arise between  $700$  and  $1200\text{ cm}^{-1}$ . **Fig. 2.10** demonstrates the selectivity of Raman spectroscopy in identifying closely related hydrocarbons and SHRS' efficacy in measuring their spectra at 19 meters distance.

### **2.4.3 Comparison of Raman Spectra of Minerals as Measured by SHRS and a Diffraction Grating Spectrometer**

We measured the Raman spectra of calcite at a distance of 2.845 meters from the collecting optic and compared the spectral resolutions and signal-to-noise ratios of a traditional grating spectrometer, traditional two-grating SHRS, and the one-grating SHRS presented in this paper. The diffraction grating spectrometer utilized for this measurement has been described (Gasda et al. 2015) previously. Each Raman spectrum was the summation of one-hundred 12.5 mJ laser

pulses. For each spectrometer, one-hundred Raman spectra were acquired of calcite so that the signal-to-noise ratio calculations could be performed by defining the signal as the median of one-hundred Lorentzian peak amplitude fits of the carbonate symmetric stretch of calcite, and the noise defined as the median absolute deviations of those one-hundred peak amplitude fits. Median and median absolute deviation were selected as the metrics for central tendency and dispersion in lieu of mean and standard deviation because the former are insensitive to outliers. In the spectra presented in **Fig. 2.11**, the solid lines represent the median quantity for those one-hundred spectra, and the shaded region about that solid line represents the median absolute deviation. **Fig. 2.11** demonstrates that the grating spectrometer has the highest SNR as its median absolute deviation error bars are so small that the width of the line used to plot the spectra is greater than the median absolute deviation itself. **Fig. 2.11** also makes clear that one-grating SHS consistently outperforms two-grating SHS in terms of sensitivity to weaker Raman scattering modes and SNR for all Raman bands. Of course, the signal to noise ratio in the Raman spectra measured with SHRS can be improved by integrating the signal for a longer time as is shown in **Figs. 1-6**. The advantage of the SHRS is that one could simultaneously measure the spectrum of a large area of the sample and SHRS is not sensitive to the alignment as it does not use slit.

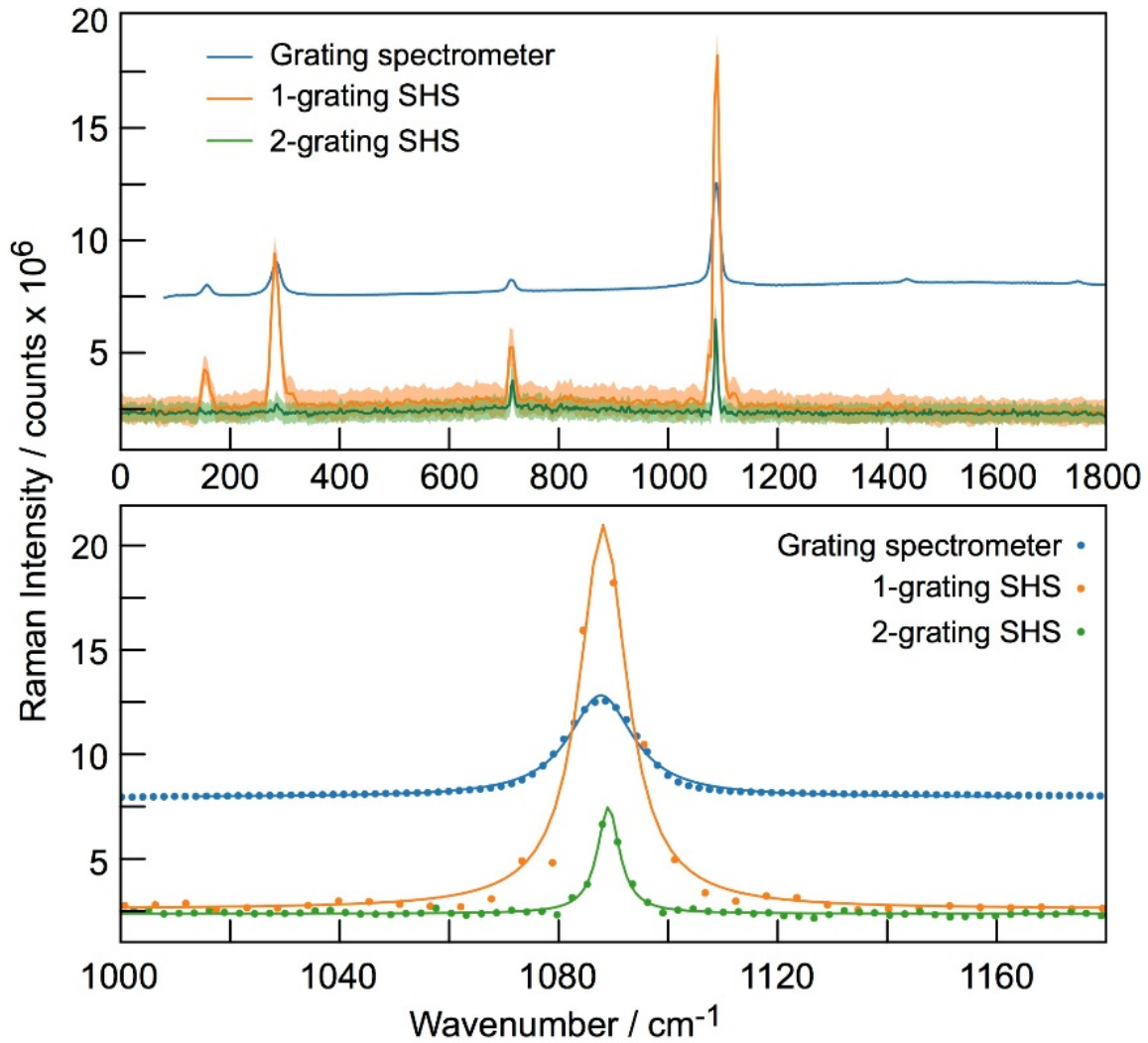


**Figure 2.11** The Raman spectrum of calcite as measured by a diffraction grating spectrometer, two-grating SHRS and one-grating SHRS. The diffraction grating spectrometer attains the highest SNR, followed by the one-grating SHRS, followed by the two-grating SHRS while the spectral resolution characterized by the FWHM of this Raman band follows the reverse trend.

## 2.5 Summary

Spatial heterodyne spectrometers measure Raman spectra by imaging crossed wavefronts produced by wavenumber-dependent diffraction angles of light incident upon a grating. The

crossed wavefronts produce a superposition of spatial interference fringes that may be converted to a Raman spectrum upon applying a Fourier transform. Until now, spatial heterodyne Raman spectrometers have utilized a two grating design whereupon a stationary diffraction grating is placed equidistant from a beam-splitter in each arm of the interferometer. In the present work, a stationary  $\lambda/10$  mirror has replaced one of the diffraction gratings. This modification has a two principle effects. First, the detector records a greater number of photons as spectral light is not lost into unused diffraction orders in the mirror arm of mSHRS. Second, the bandpass is doubled while the spectral resolution is cut in half. In the instrumental design used in the present work, we report achieving a maximum bandpass of  $4915\text{ cm}^{-1}$ , and a minimum FWHM of  $7.5\text{ cm}^{-1}$  for the forsterite peak centered at  $824\text{ cm}^{-1}$ . In addition, we report the remote-sensing Raman spectra of minerals, organic and biomarker compounds at 19 meters distance, which is the furthest remote-sensing distance achieved by any SHRS known to the authors.

## **Chapter 3. Suppressing the multiplex disadvantage in photon-noise limited interferometry via cross-dispersed spatial heterodyne spectrometry**

Spatial heterodyne spectrometers (SHS) are members of the static Fourier transform class of spectrometers, well-regarded for their ability to acquire high-resolution, high wavelength precision emission spectra in compact, small footprint packages. In an SHS experiment, a Fizeau fringe is generated for every spectral feature in a given spectrum, and SHS records the superposition of all Fizeau fringes in the spectrum on a detector. Hence, the sensitivity of spatial heterodyne spectrometer is constrained by uncorrelated, multiplicative photon-noise that limits the detection of spectral features to those that are more luminous than the square root of the total incident flux onto the detector. In essence, powerful spectral features create a rising floor of noise that wash out less luminous features. In the present work, we introduce a novel spectrometer coupling, that being an Amici prism spectrometer in series with SHS, that correlates photon shot noise along one axis of a detector and suppresses multiplicative noise within each row of the interferogram image. We demonstrate that this spectrometer pairing facilitates the measurement of weak Raman spectral features that, in a traditional SHS measurement, would be washed out by multiplicative photon-noise.

### **3.1 Development of Dispersed Fourier Transform Spectrometers**

Spatial heterodyne spectrometers (SHS) are amplitude-modulating interferometers, capable of producing wavenumber-dependent Fizeau fringes that can be imaged onto a charge-coupled device (CCD). The principle benefit of SHS is that its acceptance angle is greater than dispersive

spectrometers of similar dimension because spectral resolution (Lenzner & Diels 2016) is defined by the minimum change in wavelength that causes a change of half a fringe period across the CCD. For dispersive spectrometers, spectral resolution (Hobbs 2009) is proportional to slit width over focal length. One can attempt to increase the throughput transmitted through a fixed slit width by increasing the acceptance angle, but this causes aberrations to occur in the spectral reconstruction that in turn diminishes the spectral resolution. The larger acceptance angle of SHS is useful in many practical applications, including measuring spectra with large laser spot sizes or field instruments that experience wide temperature variations where aligning laser spots onto the field-of-view (FOV) of a dispersive spectrometer is challenging at remote-sensing distances. However, SHS' throughput advantage does not typically result in increased sensitivity. When an SHS interferogram is limited by photon-noise (e.g. in the UV-Vis domain), SHS suffers from the multiplex disadvantage, meaning that photon-noise associated with any one spectral feature is distributed multiplicatively into every other spectral bin as well. In effect, a multiplex noise floor, known as the grass, is generated that is proportional to the square root of the total incident flux in the interferogram. As the total incident flux increases, so does the multiplex noise floor, thus limiting the detection of weak spectral features.

When Connes (Connes 1958) invented the predecessor to SHS, known as SISAM, Jacquinet (Jacquinet 1960) noted that such an instrument could still be useful in the photon-noise limited domain when spectral density is low (e.g. Raman spectroscopy (Gomer et al. 2011; Lamsal & Angel 2015; Egan et al. 2018; Zettner et al. 2020)). The key to attaining SHS spectra with high signal-to-noise ratios (SNR) is to limit the total incident flux present in the interferogram relative to the desired spectral feature as much as possible. Typically, this is achieved by utilizing bandpass filters (Sweedler et al. 1990; Harlander et al. 2002) that reject spectral light beyond the

Nyquist wavelength or that select for desired spectral features. This design choice, although effective in limiting multiplicative noise, undermines the throughput advantage and wavelength coverage of SHS. Other attempts have been made to limit the spectral density within an SHS interferogram, notably the echelle grating SHS variant (Sheinis et al. 2008) that utilizes various high diffraction grating orders to spatially offset narrow bandpasses onto an CCD. The echelle grating SHS variant has been demonstrated in a proof-of-concept sense, although wavelength calibration must be performed separately for each diffraction order and cross-interference from different orders makes interpreting echelle SHS spectra non-trivial.

In the past decade or so, a new class of hybrid dispersive-interferometric spectrometers, sometimes referred to as dispersed Fourier transform spectrometers (Behr et al. 2009; Hajian et al. 2007; Erskine et al. 2016; Kim et al. 2015) (dFTS), has come to fruition. In practice, this class of instruments typically find use in replacing cumbersome cross-dispersed echelle spectrometers in experiments where large resolving powers and high wavelength precision are required. Recently, a few authors (Morgan et al. 2016; Riebe et al. 2014) interested in isotopic quantification via laser-induced breakdown and laser ablation molecular emission spectroscopies have developed novel spectrometers that pair a dispersive element (i.e. prism or grating) in series with a Fabry-Perot etalon. This combination achieves ultra-high resolution (on the order of 10 pm) and wider wavelength coverages than stand-alone Fabry-Perot etalons by spatially offsetting degenerate harmonics in Airy's function on a CCD.

In the present work, we describe the creation of a new interferometer variant, named the cross-dispersed spatial heterodyne spectrometer (xSHS), that pairs an Amici prism spectrometer in series with an SHS. The benefits of xSHS are manyfold. First, the multiplex disadvantage is severely diminished by limiting the spectral density present in a given row of the CCD to a

narrow wavelength coverage. Second, wavenumber-dependent Fizeau fringes attain higher fringe visibility and wider fringe envelopes when compared to traditional SHS measurements as a result of the wavelength coverage represented in a given row being constrained. Third, spectral features beyond the Nyquist limit do not contribute noise as a consequence of cross-dispersion, thus eliminating the need for bandpass filtering. Fourth, the degeneracy of Fizeau fringes is broken by cross-dispersion, facilitating unambiguous sampling of spatial fringes equidistance from the Littrow wavelength and aliased fringes beyond the Nyquist limit. Fifth, the Amici prism spectrometer provides a low-resolution spectrum covering hundreds of nanometers, which in turn allows an experimentalist to tune the grating angles of SHS to a spectral region of interest with foreknowledge. The first proof-of-concept demonstration of this Amici prism and SHS coupling is presented herein.

### **3.2 Theory of Multiplicative Gain**

The formulation of SHS figures of merit have been explained in detail (Lenzner 2016; Harlander 2002, 2018) elsewhere, and will not be reiterated here. Instead, attention will be focused on UV-Vis interferometers and multiplicative noise. Multiplex gain is defined as the ratio of  $\text{SNR}_{\text{FTS}}/\text{SNR}_{\text{dispersive}}$  under the limiting assumption that the throughput of the FTS and dispersive instruments under comparison are equal. Kahn (Kahn 1959) was the first to give a mathematical treatment for single-channel, photon-noise limited interferometers, stating that such instruments experience a multiplex gain relative to scanning spectrometers when the signal intensity for a spectral feature of interest is twice the mean intensity of the wavelengths covered by the free spectral range of the interferometer. Later authors (Hirschfeld 1976; Luc &

Gerstenkorn 1978; Gerstenkorn & Luc 1976; Everall & Howard 1989; Zhao & McCreery 1997) have formulated the multiplex gain as follows.

$$G_{SNR} = [I(\sigma) / N \overline{I(\sigma)}]^{1/2} \quad (3.1)$$

where  $I(\sigma)$  is the intensity of a single spectral feature,  $\overline{I(\sigma)}$  is the mean intensity of the whole spectrum and  $N$  is the number of resolution elements. When a single spectral feature is present in the spectrum,  $G_{SNR}$  equals one and FTS attains the same SNR as a dispersive grating spectrometer. However, as the number of spectral features increases, the multiplex gain factor, dynamic range of the detector, and SNR of all spectral features decrease simultaneously for multiplexed instruments in the photon-noise domain. Therefore, the only way to increase the sensitivity of SHS in this domain is to manipulate the multiplex gain factor in such a way as to minimize  $\overline{I(\sigma)}$  relative to  $I(\sigma)$ . In the following sections, we demonstrate how this can be accomplished via xSHS.

### 3.3 Design of a Cross-Dispersed Spatial Heterodyne Spectrometer

xSHS is an Amici prism spectrometer coupled to an SHS (see **Fig. 3.1**). Spectral light is collected by a 50 mm focal length Nikon lens and collimated by a 1" f/2 achromatic lens. The spot size of the collimated beam is 8 mm in diameter. The spot size of the beam was chosen so that the entirety of the spot could transmit through a commercial, off-the-shelf double Amici prism (hereafter referred to simply as the Amici prism) that possessed a 10 by 10 mm entrance window. After transmitting and refracting through the Amici prism, spectral light was focused onto the stationary gratings of SHS by a 75 mm focal length, achromatic cylindrical lens. The transmission efficiency of the Amici prism was 0.78 at 532 nm. The Fizeau fringes produced at

the gratings surface were imaged by an 85 mm f/4 Nikon lens onto a Princeton Instruments PIXIS II CCD. The PIXIS CCD had 2048 pixels along the x-axis and 512 pixels along the y-axis. Each pixel was 13.5 by 13.5 microns. The detector was cooled to  $-70^{\circ}\text{C}$  and so thermal signal was essentially zero (i.e. 0.001 electrons per pixel per second). The resolution of xSHS is governed by the number of lines on the gratings illuminated and the pixel width of the detector. The grating groove density was 150 lines per mm. The maximum resolving power was 2116. The linear dispersion provided by the Amici prism on the CCD was approximately 37.7 nm per mm, and the magnification of the gratings onto the CCD was 0.90. Two light sources were used to collect spectra during this experiment. First, a Hg calibration lamp manufactured by Ocean Optics (now Ocean Insight). Second, Raman spectra excited by a 532 nm continuous-wave Nd:YAG laser, operating at 115 mW. For the Hg measurements, a Semrock FF01-571/572 bandpass filter was used where indicated, and for the Raman measurements, a Semrock E grade edge filter was used to attenuate Rayleigh scattered radiation.

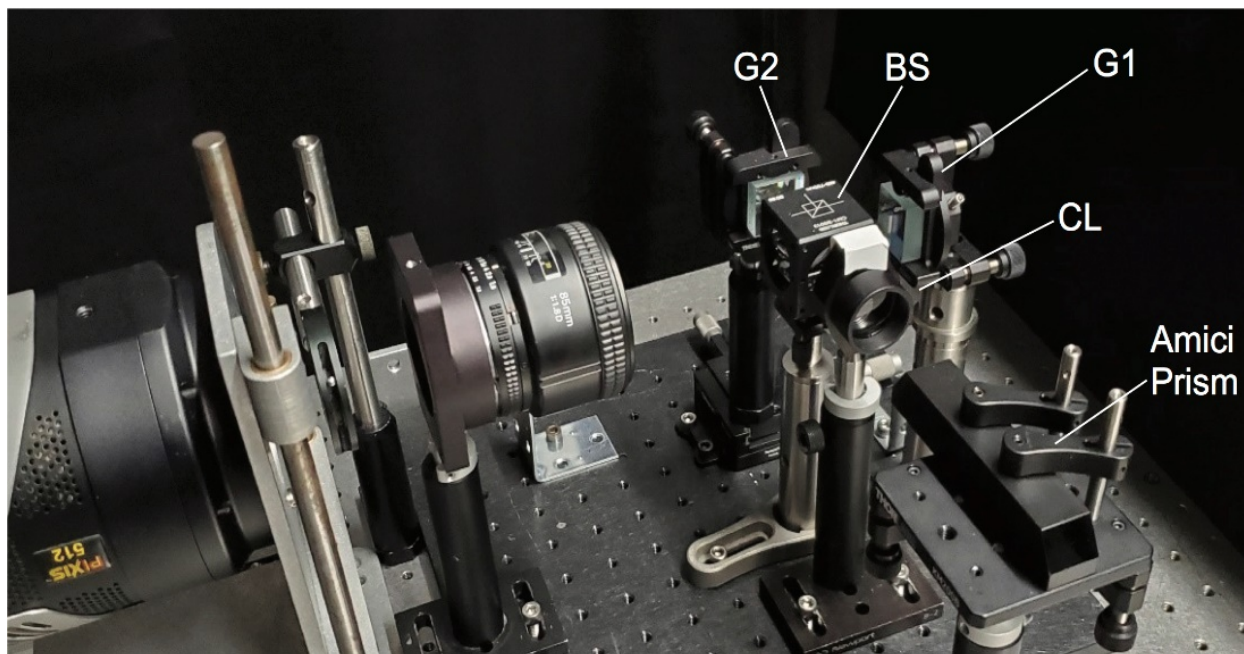


**Fig. 3.1** – An image of xSHS used in the present work. Collimated light enters the Amici prism. Spectral light is refracted, then focused onto the gratings within SHS by a cylindrical lens. SHS generates Fizeau fringes, which are imaged by a lens and recorded by a CCD.

### **3.3.1 First Light**

A Hg calibration lamp provided the spectral light for the first interferogram measured by xSHS. The purpose of the experiment was to show that the 546 nm Hg singlet could be spatially resolved by cross-dispersion from the 577 and 579 nm Hg doublet. The xSHS interferogram of the Hg lamp was collected twice, once with a Semrock FF01-571/572 bandpass filter and once without any bandpass filtering whatsoever. If the cross-dispersion was successful, no degradation in the fringe contrast should be observed whether filters were used or not. In addition, the envelope of the interferogram should be broader than a typical SHS interferogram as the breadth of an interferogram envelope is reciprocally dependent upon the wavelength coverage used to generate the interferogram. The raw, unprocessed xSHS interferogram images are presented in **Fig. 3.2**. Alongside the xSHS interferograms are SHS interferograms of Hg emission lines where the SHS instrument design is identical in every way to the instrument shown in **Fig. 3.1** except that the Amici prism and cylindrical lens were removed.

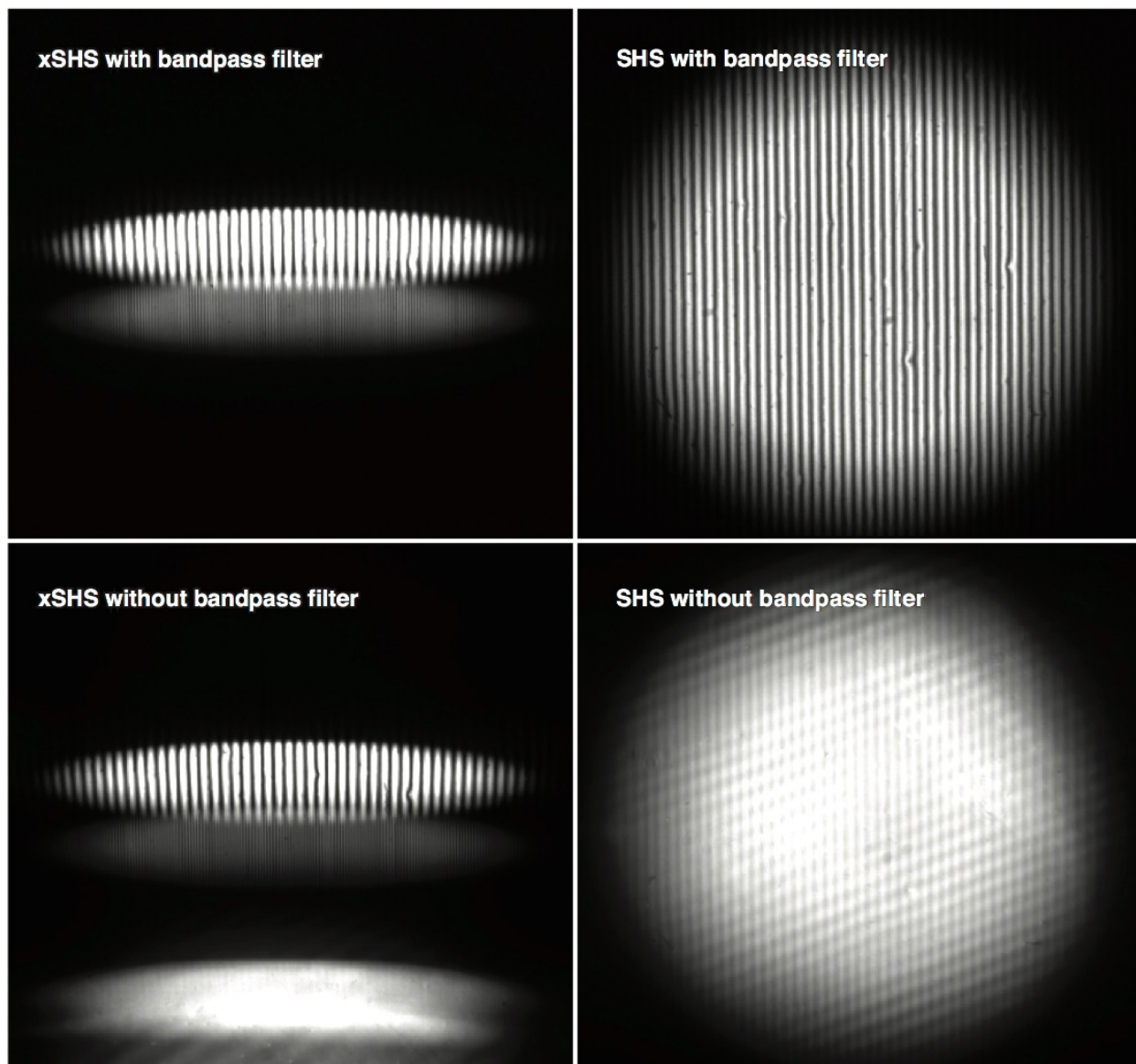


**Fig. 3.2** – The interferograms of a Hg calibration lamp as measured by xSHS and SHS with and without bandpass filters. Note that the fringe contrast appears brighter for xSHS, even though  $\sim 22\%$  of incident light is lost due to reflections at the Amici prism surfaces, as a result of spectral light being focused along the y-axis by a cylindrical lens.

Clearly, the fringe contrast present in the xSHS interferograms is higher than its SHS counterparts. Three Hg lines (i.e. 546.075, 576.961 and 579.067 nm) are present within the

wavelength coverage of the bandpass filter. In the xSHS interferograms, two distinct interferogram groupings are readily distinguishable. The first, brightest interferogram, located near the top of the image, represents the 546 nm spectral line while the fainter interferogram directly beneath it is generated by the 577 and 579 nm Hg doublet. For xSHS, the presence of, or lack thereof, bandpass filters played no role in the fringe visibility. This claim is quantified by the fringe visibility numbers quoted in **Fig. 3.3**. For SHS, the lack of bandpass filtering increased the background from aliased spectral features, which in turn diminished the fringe visibility dramatically. It is important to emphasize at this point that xSHS attains these higher fringe visibilities while losing  $\sim 22\%$  of light due to reflections at surfaces of the Amici prism by focusing the remaining light along the y-axis of the grating by the cylindrical lens.

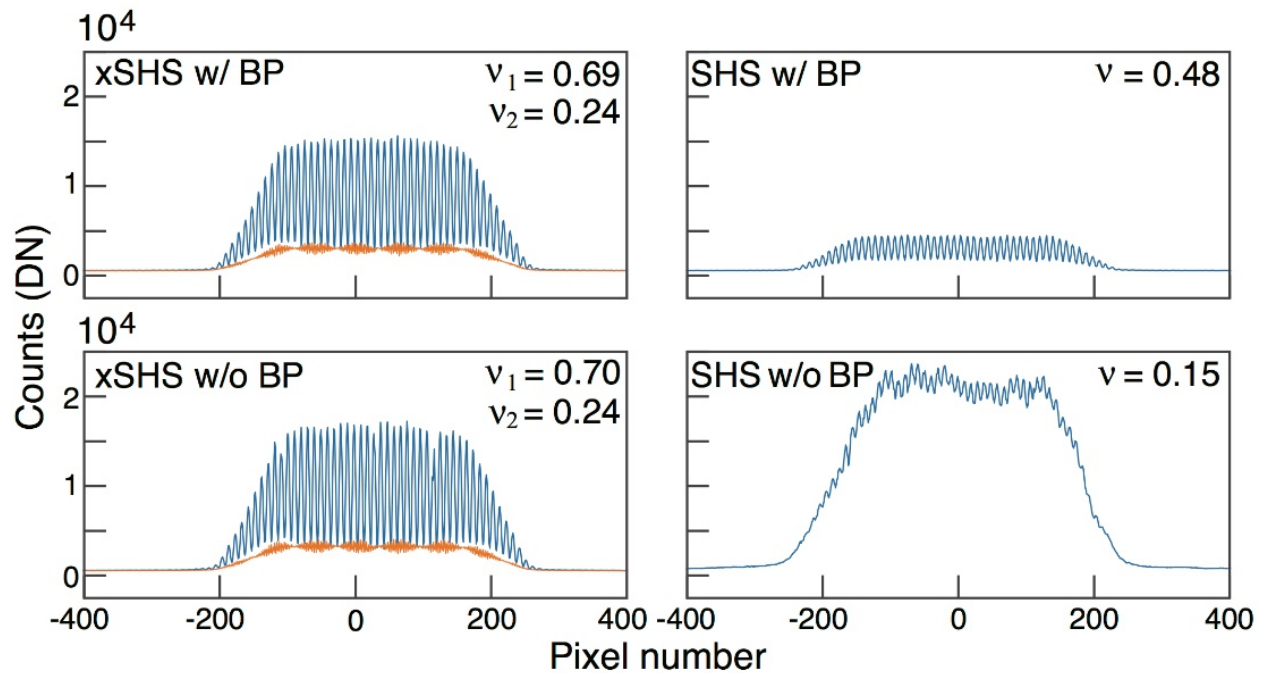


**Fig. 3.3** – Fringe visibilities were calculated for each interferogram presented in **Fig. 3.2** by taking the brightest row and applying the standard formula  $v = I_{\max} - I_{\min} / I_{\max} + I_{\min}$ . For the xSHS interferograms,  $v_1$  represents the 546 nm fringe (in blue), and  $v_2$  represents the 577 and 579 nm

fringes (in orange). Note that no change in the fringe visibility occurs for xSHS when bandpass (BP) filters are removed, while a significant degradation in fringe contrast does occur for SHS.

### 3.3.2 Raman xSHS Interferograms

In addition to Hg spectra, several Raman xSHS interferograms were acquired, namely cyclohexane, acetone, acetonitrile and methanol. For demonstration purposes, we have elected to focus our attention on the acquisition, processing and noise analysis of cyclohexane's xSHS interferogram alone. The first unprocessed Raman xSHS interferogram of cyclohexane is presented in **Fig. 3.4**. The Littrow wavelength was  $\sim 532$  nm, although the exact wavelength was not known at the time the interferogram was acquired because the grating angles were tuned by manual micrometer screws. The integration time was 10 seconds. The Raman shift increases as one scans the image from bottom to top. The brightest band, at the top of the image, was contributed by cyclohexane's C-H stretches occurring between  $2800$  and  $3000$   $\text{cm}^{-1}$ . Those C-H stretching modes lie beyond the Nyquist limit for the defined Littrow angle and pixel width, yet were still sampled unambiguously by xSHS, as will be shown later. The fringe with the highest contrast near the center of the image is cyclohexane's  $801.3$   $\text{cm}^{-1}$  Raman mode. Raman modes spaced more than  $\sim 350$   $\text{cm}^{-1}$  apart are completely resolved spatially on the CCD by cross-dispersion.

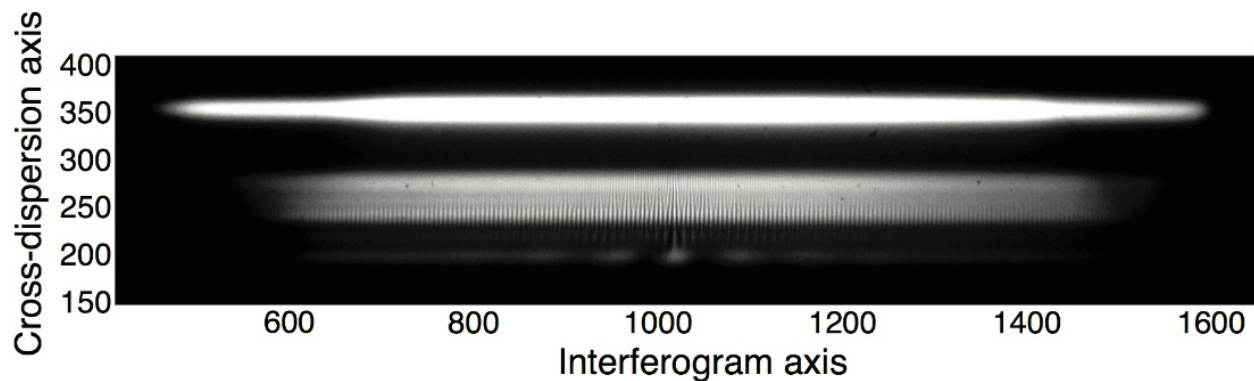


**Fig. 3.4** – The xSHS interferogram of cyclohexane’s Raman spectrum. The Littrow wavelength was  $\sim 532$  nm. As one scans from the bottom of the image to the top, the Raman shift increases. The brightest band at the top of the image is cyclohexane’s C-H stretching region. The fringe with the highest contrast at the center of the image is cyclohexane’s  $801.3\text{ cm}^{-1}$  Raman mode. The xSHS interferogram was windowed to those pixels where spectral light occurred.

### 3.3.3 Visualizing the Multiplex Disadvantage

xSHS interferograms may be treated as  $N$  SHS interferograms where  $N$  equals the number of rows on the detector. As mentioned previously, multiplex noise is proportional to the square root of the total incident flux. By processing xSHS interferograms via row-by-row FT (Barnett et al. 2017), the total incident flux becomes a function of row number and changes depending upon the summed intensities of spectral features present in that row. An illustration of this processing routine is depicted in **Fig. 3.5** as a visual guide. Note that the y-axis is calibrated by wavenumber, and the x-axis is calibrated by spatial frequency. If this same interferogram had been acquired by SHS, the C-H stretching modes between  $2800$  and  $3000\text{ cm}^{-1}$  would have been aliased into the  $\text{CH}_2$  bending region of the reduced spectrum between  $1000$  and  $1300\text{ cm}^{-1}$  since those modes produce the same number of fringes per unit length on the detector at this Littrow angle. However, Amici prism induced cross-dispersion breaks this degeneracy, leading to an

increase in the effective wavelength coverage beyond the Nyquist limit. The high-resolution x-axis wavelength sampling, generated by SHS, attains a spectral bin width of  $\sim 58.3$  pm, and the low-resolution y-axis wavelength sampling, produced by the Amici prism, possesses a spectral bin width of  $\sim 518$  pm. The dispersion provided by the Amici prism was linear within the wavelength coverage measured in these experiments ( $R^2 \sim 0.999$ ). Multiplicative noise, known affectionately as “the grass”, spans across the entirety of a row where a spectral feature occurs and can be most easily identified in the C-H stretching region for cyclohexane, occurring between  $2800$  and  $3000$   $\text{cm}^{-1}$ , and to a lesser extent in the C-C stretch and  $\text{CH}_2$  bending region between  $801.3$  and  $1444.4$   $\text{cm}^{-1}$ .

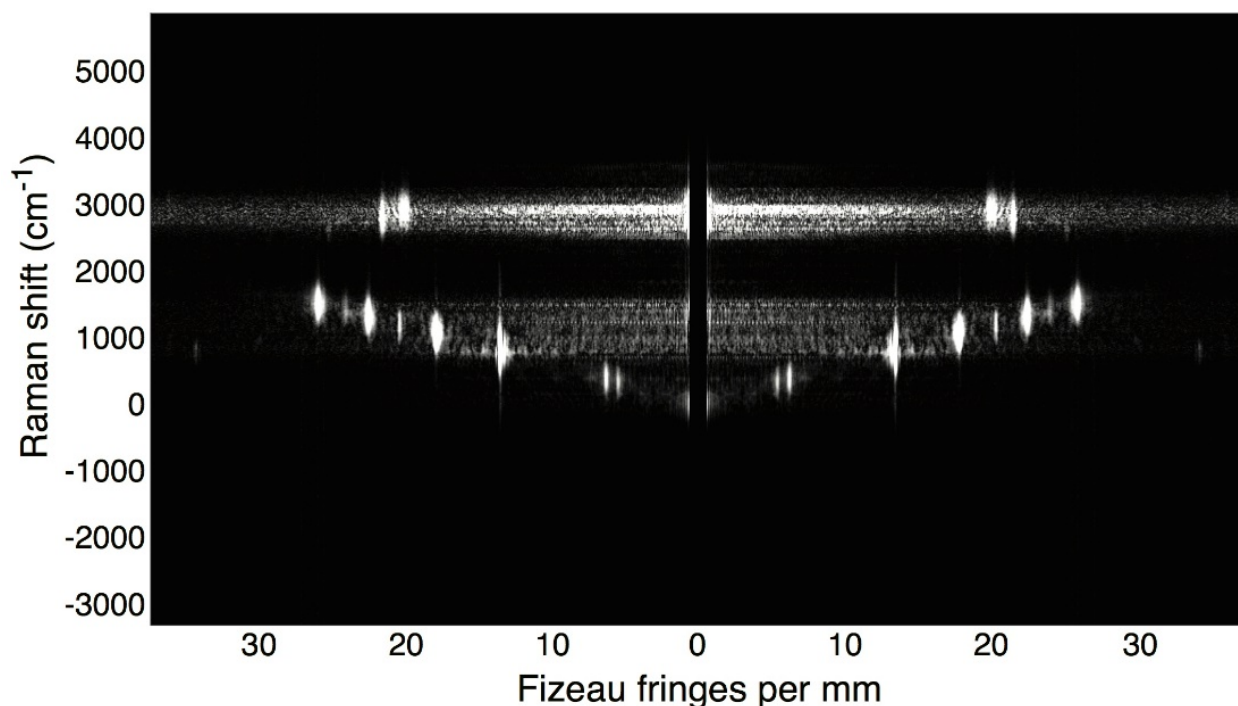


**Fig. 3.5** – The above image illustrates the row by row FT of cyclohexane’s xSHS Raman interferogram shown in **Fig. 3.4**. The low spatial frequencies near zero fringes per mm were masked so as to not skew the color scale by the first term in the Fourier series. Note that where a Raman feature occurs, multiplex noise is present across the entire row. This is the multiplex disadvantage (i.e. uncorrelated photon noise). By cross-dispersing spectral light before (or after)

generating Fizeau fringes, the photon noise becomes correlated and the multiplex disadvantage is defeated.

### 3.3.4 Mowing the Long Grass

Most of the pixels present in **Fig. 3.5** do not have, nor could have, Raman spectral information. The cross-dispersion provided by the Amici prism makes it so that particular spatial frequencies in the interferogram can only occur in specific columns of the row-by-row FT image. Therefore, we can create a mask to overlay **Fig. 3.5** that maintains FT image pixels that contain spectral information while rejecting those pixels that do not. After creating and applying this mask, we can then safely integrate the remaining pixels along the x-axis that contain useful information. The results of this data reduction strategy are presented in **Fig. 3.6**. Two points are important to spell out here. First, spectral features beyond the Nyquist wavelength can be unambiguously sampled without aliasing thanks to the cross-dispersion. Second, the weak Raman modes located at  $384.1$  and  $426.3\text{ cm}^{-1}$  are present with high SNR because their interferograms occurred at a local minimum in terms of total incident flux. This fact will become important later.

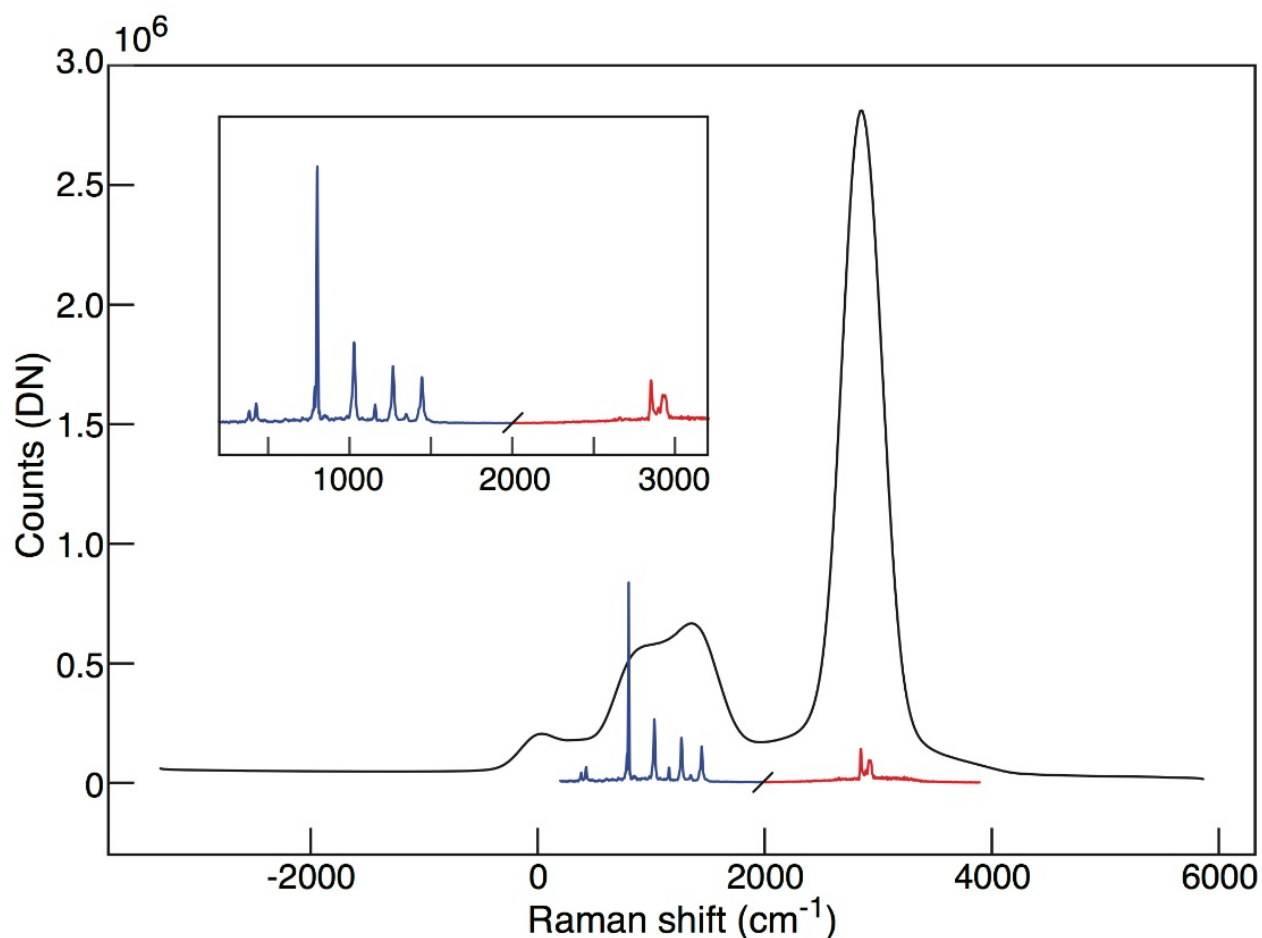


**Fig. 3.6** – The xSHS and Amici prism Raman spectra of cyclohexane. Three spectra are present here: the xSHS spectrum within the Nyquist limit (blue), the xSHS spectrum beyond the Nyquist limit (red) and the Amici prism spectrum (black). A slash was placed between the blue and red xSHS spectra as a visual aid to those viewing this figure in greyscale. The Amici prism spectrum is a proxy for total incident flux in a given row of the xSHS interferogram. Note that the Raman doublet at 384.1 and 426.3 cm<sup>-1</sup> occurs at a local minimum in incident flux.

### 3.3.5 Beating the Multiplex Disadvantage

The purpose of xSHS is to increase the sensitivity of the instrument, relative to traditional SHS, by increasing the multiplex gain factor. In order to demonstrate this, 100 xSHS

interferograms of cyclohexane were acquired and the SNR of the Raman peaks present there were calculated. To estimate SNR, we fit a Lorentzian to each peak, defined the signal as the median peak area and the noise as the median absolute deviation of those 100 peak area fits. For comparison purposes, 100 pseudo-SHS interferograms were created by summing up the columns present in the xSHS interferogram into a one-dimensional array so that the multiplex gain mimicked traditional SHS. The 100 xSHS and pseudo-SHS Raman spectra of cyclohexane are presented in **Fig. 3.7**. Clearly, the multiplex noise floor is higher in the pseudo-SHS spectra as a result of the total incident flux being higher. This point is further emphasized by the SNR calculations presented in **Table 3.1**.

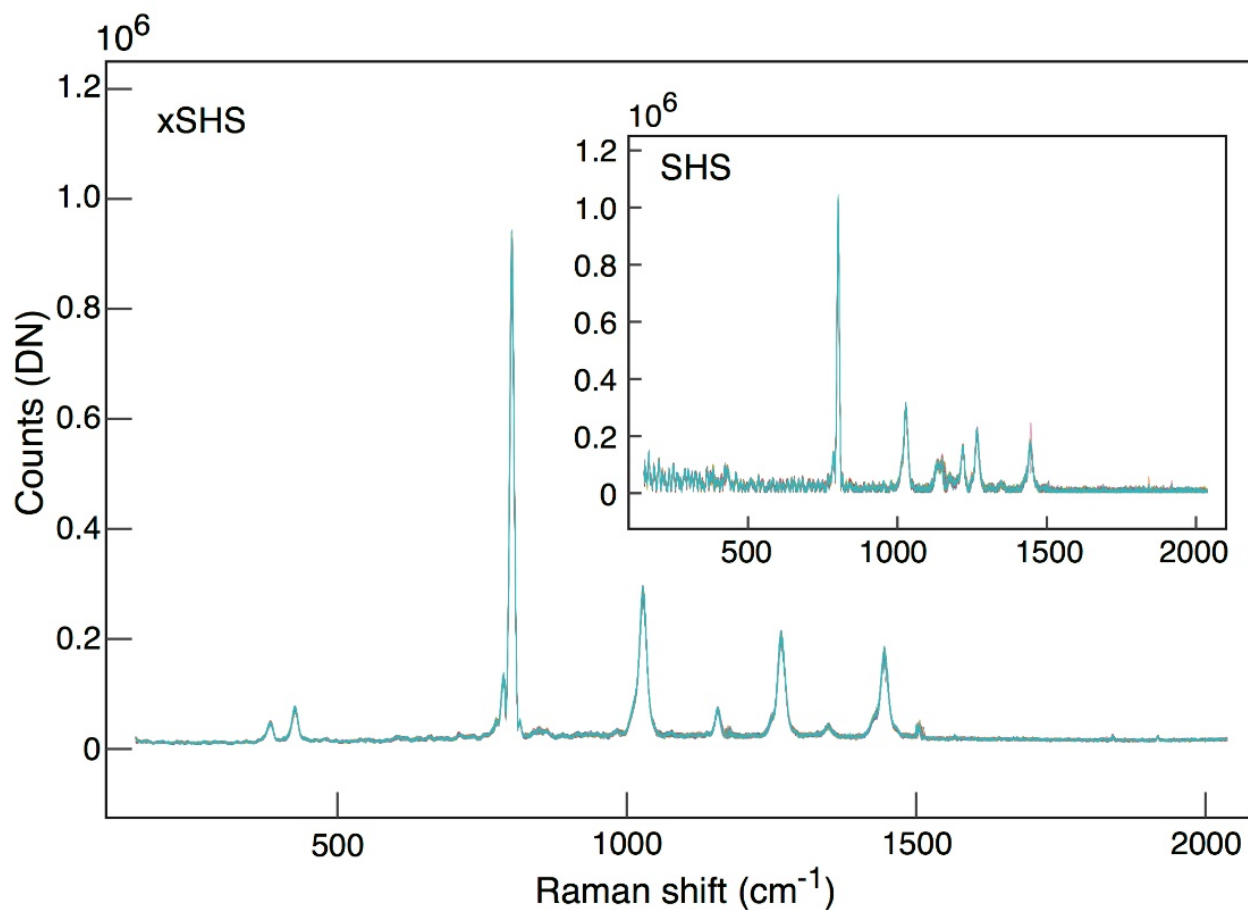


**Fig. 3.7** – Plotted above are 100 spectra measured with xSHS (main figure) and 100 pseudo-SHS (sub-figure) spectra plotted, superimposed. In the pseudo-SHS spectra, the total incident flux per interferogram is much larger, which causes the low Raman shift modes at 384.1 and 426.3  $\text{cm}^{-1}$  to be washed out by multiplicative photon noise. In the pseudo-SHS spectra, spurious peaks appear in the  $\text{CH}_2$  bending region caused by aliasing of the C-H stretching modes.

**Table 3.1** – SNR comparisons of Raman peaks of cyclohexane measured with xSHS and pseudo-SHS. xSHS outperforms pseudo-SHS in terms of SNR for all but the strongest 801.3  $\text{cm}^{-1}$  Raman line. For the weakest Raman features (i.e. 384.1, 426.3 and 1347.9  $\text{cm}^{-1}$ ), xSHS can detect these features whereas SHS cannot.

| Raman Shift ( $\text{cm}^{-1}$ ) | xSHS SNR | SHS SNR |
|----------------------------------|----------|---------|
| 384.1                            | 17.2     | < 1     |
| 426.3                            | 21       | < 1     |
| 801.3                            | 28.2     | 34.2    |
| 1028.3                           | 31.3     | 30.6    |
| 1157.6                           | 14.9     | N/A     |
| 1266.4                           | 25.5     | 20.7    |
| 1347.9                           | 8.3      | < 1     |
| 1444.4                           | 26.9     | 20.5    |

Earlier, we posited that SNR in FTS is proportional to the multiplex gain factor,  $G_{SNR}$ . Since the cross-dispersion provided by the Amici prism converts the total incident flux,  $\overline{I(\sigma)}$ , into a row-dependent parameter, xSHS interferograms can be used to verify this claim. From the row-by-row FT, the total incident flux,  $\overline{I(\sigma)}$ , may be approximated from the mean of the

interferogram in a given row, and the intensity of a spectral feature,  $I(\sigma)$ , may be estimated by a spectral feature's Lorentzian peak area in a single row. The results of this processing routine are presented in **Fig. 3.8**. Since a given Raman peak occurs in multiple rows of the xSHS interferogram, this processing routine allows one to track how SNR evolves as a function of the multiplex factor gain.

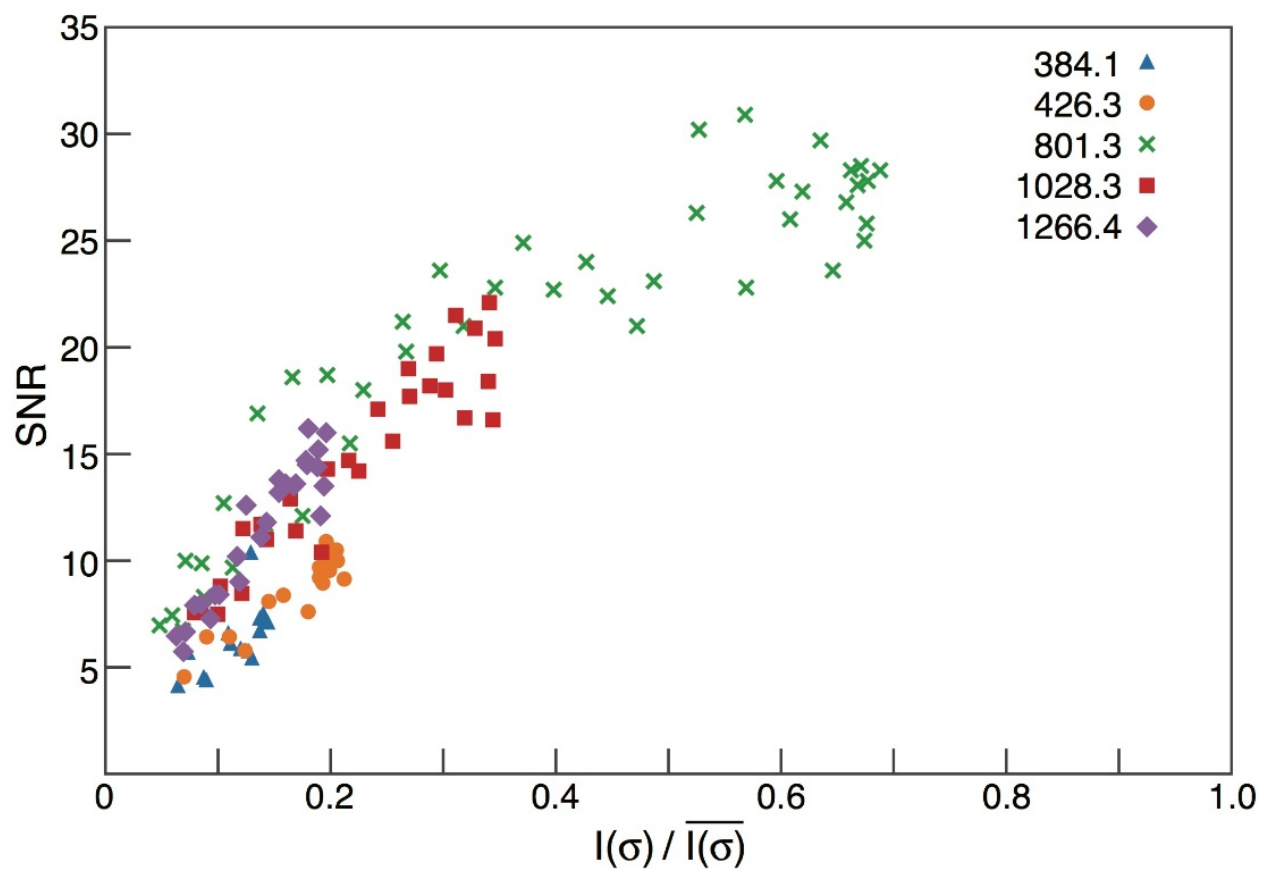


**Fig. 3.8** – The SNR vs.  $I(\sigma)/\overline{I(\sigma)}$  scatter plot presented here illustrates how SNR attained in an SHS experiment depends upon the ratio of the peak intensity divided by the mean of the interferogram. When the signal ratio becomes significantly small enough, the SNR equals one. Below this signal ratio, a spectral feature cannot be measured.

Finally, three Raman peaks present in the xSHS spectra (i.e. 384.1, 426.3 and 1347.9  $\text{cm}^{-1}$ ) were claimed to have a SNR of less than one in the pseudo-SHS spectra, as stated in **Table 3.1**. By defining  $I(\sigma)$  as the peak area from the xSHS spectra, and  $\overline{I(\sigma)}$  as the mean of the pseudo-SHS interferogram, we can now use the trends in **Fig. 3.8** to predict what the SNR of those three peaks should be in the pseudo-SHS spectra. Those predictions are presented in **Table 3.2**. Since the expected SNR is less than one, those Raman peaks in the pseudo-SHS spectra could never rise above the detection limit given their multiplex gain factors, even if an infinite number of photons were available.

**Table 3.2** – Predicted SNR of cyclohexane’s least luminous Raman features via SHS when acquiring interferograms in the full presence of the multiplex disadvantage.

| Raman Shift ( $\text{cm}^{-1}$ ) | $I(\sigma)_{xSHS}$ | $I(\sigma)_{xSHS}/\overline{I(\sigma)}_{SHS}$ | Expected SHS SNR |
|----------------------------------|--------------------|---|------------------|
| 384.1                            | 5.54e5             | 3.84e-3                                       | 0.61             |
| 426.3                            | 1.06e6             | 7.34e-3                                       | 0.95             |
| 1347.9                           | 3.25e5             | 2.25e-3                                       | 0.98             |

### 3.4 The Abstemious Spatial Heterodyne Spectrometer

Spatial heterodyne spectrometers are, by nature, hungry for photons. In a typical SHS experiment, a given spectral feature must produce a Fizeau fringe over  $N_x$  by  $N_y$  pixels and be at least as luminous as the square root of the total incident flux. These design limitations are quite severe, especially as the density of spectral lines present increases. xSHS quells this hunger, to some extent. In the ideal case, xSHS addresses these two constraints by setting  $\overline{I(\sigma)}$  equal to  $I(\sigma)$  and limiting the production of a Fizeau fringe to just  $N_x$  pixels. In this limit, no

multiplicative noise exists, so xSHS has the same noise profile as a dispersive spectrometer. If the throughputs of the two competing spectrometers were equal, the dispersive spectrometer would still maintain a sensitivity advantage by localizing the photons onto a smaller number of pixels. But the throughputs are not equal. SHS achieves  $10^2$  to  $10^4$  greater throughputs than dispersive spectrometers, depending on whether SHS is field-widened or not.

In Fellgett's era (Fellgett 1967), the multiplex advantage rested upon the assumption that spare channel capacity existed in detectors that could be utilized to increase the SNR relative to quantifying the spectral elements one by one. Light existed, or had the potential to exist, that could not be measured in the time allotted by a scanning spectrometer. In the modern era, analogous situations can arise for remote-sensing Raman spectrometers. For example, if a Raman sample covering the entire extent of the FOV of SHS and dispersive spectrometer is scattering Raman light at uniform spectral radiant exitance, then  $10^2$  to  $10^4$  more photons would be scattered in the FOV for SHS. If the dispersive spectrometer samples the Raman feature over a few pixels, and SHS samples the same feature over a few hundred pixels, SHS could attain a sensitivity advantage, depending upon the spectral radiance of the feature, if the increased throughput offsets diluting the detection of Raman photons associated with that feature over a greater number of pixels.

### **3.5 Summary**

In this work, we demonstrated that multiplicative photon-noise can be suppressed by coupling SHS to an Amici prism spectrometer. The principle benefits of this method are higher fringe visibilities, broader fringe envelopes, unambiguous sampling of fringes equidistant from Littrow

and beyond the Nyquist wavelength, eliminating the need for bandpass filtering, higher SNR for weak spectral features, and low-resolution sampling of spectral features over an extensive wavelength coverage. These benefits are offset by transmission losses at the prism interfaces and additional complexity in alignment. This work is the first experimental demonstration of cross-dispersing Fizeau fringes generated by SHS via an external spectrometer for the purposes of detecting weak Raman signatures.

## Chapter 4. SuperCam Thermal-Vacuum Testing and Raman Detection Limits

### 4.1 Raman Spectrometers Take Flight to Mars

The definitive identification of aqueously altered minerals on the surface of Mars by remote-sensing, rover and lander instrument suites has caused a resurgence in the belief that Mars was once capable of supporting life. The belief that Mars was once warm, wet and therefore habitable relies upon the convergence of many independent lines of evidence, namely the discovery of clay minerals (Murchie 2009; Vaniman 2014) weathered from source rocks of Martian basaltic composition, ferrous oxides and carbonates (McSween 2006; Morris 2006, 2010) aqueously altered from olivine, hydrated sulfates in fracture-filled veins of mudstones (Nachon 2014; Rapin 2016), elevated zinc concentrations (Squyres 2012), chloride minerals (Murchie 2009; Osterloo 2008) and heterogeneous distribution of phyllosilicates (Murchie 2009; Mustard 2008) indicative of ancient hydrothermal environments being extant on Mars. The recognition of widespread water-bearing mineral phases on the surface naturally led researchers to question the origin of the water reservoirs (Bibring 2006; Mouginit 2012), the transport and evolution of water and soluble ions through time, the state of hydration present in diverse modalities, the salinity and acidity of water sources that weather Martian source rocks (Gasda 2017; Martín-Torres 2015; Rapin 2016). To date, no instrument on Mars is capable of unambiguously identifying mineral stereochemistry via spectroscopic methods, which has limited the ability of scientists to disentangle formation mechanisms of the Martian mantle and altered minerals (Sautter 2015).

In 2013, NASA assembled a science definition team to formalize the requirements for a successor to Curiosity (Mustard 2013), determining that *context mineralogy* would be essential

for a follow-up mission, capable of detecting carbonates, phyllosilicates, sulfates, zeolites and silica at scales of 1 to 10 cm and remote-sensing distances up to 10 m for the threshold requirements, and crystal structure, cation composition and hydration states for the baseline requirements. Meanwhile, a sparse constellation of planetary science groups had been marketing the concept of sending a Raman spectrometer to Mars (Rull 2006; Sharma 2003; Wang 2003; Wiens 2005). The selling points were straightforward. Raman spectroscopy probes molecular stereochemistry. Raman peak positions are sensitive to polymorphs (Edwards 2013), compositional variation and hydration states (Freeman 2008; Jolliff 2006; Kuebler 2006; Wang 2001, 2004); Raman linewidths are sensitive to crystallinity (Wang 2004); Raman intensities are sensitive to grain size (Wiens 2021) and polarization; Raman laser spot sizes can probe individual grains at fine-scale (i.e.  $\sim 20 \mu\text{m}$  spot) via  $\mu\text{Raman}$  (Wang 2015) or ensembles of mineral assemblages at context-scale (i.e.  $\sim \text{mm}$  spot) via remote-Raman spectroscopy (Maurice 2021; Wiens 2021).

In the end, the arguments in favor of Raman spectroscopy for planetary science missions were convincing, and four separate Raman spectrometers were selected for missions to the Mars system, namely SuperCam (Maurice 2021; Wiens 2021) and SHERLOC (Beegle 2015) as part of the Mars 2020 rover headed to Jezero crater, RLS aboard the ExoMars rover (destination TBD), and RAX aboard MMX destined for Phobos (Hagelschuer 2019). The Raman spectrometers selected for these missions can be categorized by their excitation sources where SuperCam is a pulsed, time-resolved, remote-sensing Raman spectrometer (i.e. context spectroscopy), and the others are continuous-wave (CW), fine-scale Raman spectrometers (i.e. contact spectroscopy). The disparate philosophies inherent to the design of these two classes of Raman spectrometers present different challenges. In the case of CW Raman systems, the principle challenges stem

from the need to bring samples to the spectrometer, either by a movable arm or roving, and the need to block out ambient background light (e.g. solar reflectance) in order to obtain high signal-to-noise ratio (SNR) Raman spectra. For pulsed Raman systems, the main challenges originate from large laser spot sizes that irradiate multiple phases in a given measurement, coupling efficiencies between the Raman target and collection optics at large distances, and aligning the laser spot within the field-of-view of the spectrometer. Regardless of the philosophy employed, the success of Raman spectrometers on planetary surfaces depends upon their ability to collect enough Raman photons to surpass the background noise floor. Details of SuperCam's background signal and concomitant noise is presented herein.

## **4.2 Thermal-Vacuum Testing**

In order to characterize SuperCam's response to temperature and pressure, the spectrometer portion of the instrument (known as the body unit or BU) was placed in a Tenney chamber where pressure was lowered to Martian atmospheric conditions (i.e. 2 to 10 torr), and chamber temperature was cycled through those temperatures expected to be experienced by SuperCam on Mars. The pressure and temperature cycles utilized in this thermal-vacuum testing (TVAC) are depicted in **Fig. 4.1**. At pre-defined temperatures (known as test points), the chamber and spectrometer were allowed to come to thermal equilibrium, and a series of optical, wavelength and background experiments were performed. The background signal consists of three primary components, specifically CCD bias, dark current and effective background illumination (EBI). In this analysis, CCD bias is defined as the rest-charge per pixel at zero-second integration time; dark current as the number of electrons liberated thermally in a given pixel, dependent both upon detector temperature and time, and EBI defined as electrons liberated from the intensifier's

photocathode, dependent upon intensifier temperature, gate width and gain. Since experiments performed in TVAC testing sampled time, temperature and gain parameter space, the dependency of the background on the above-mentioned parameters can be modeled, and background noise present at arbitrary integration times, intensifier gate-widths, detector temperature, intensifier temperature and intensifier gain quantified.

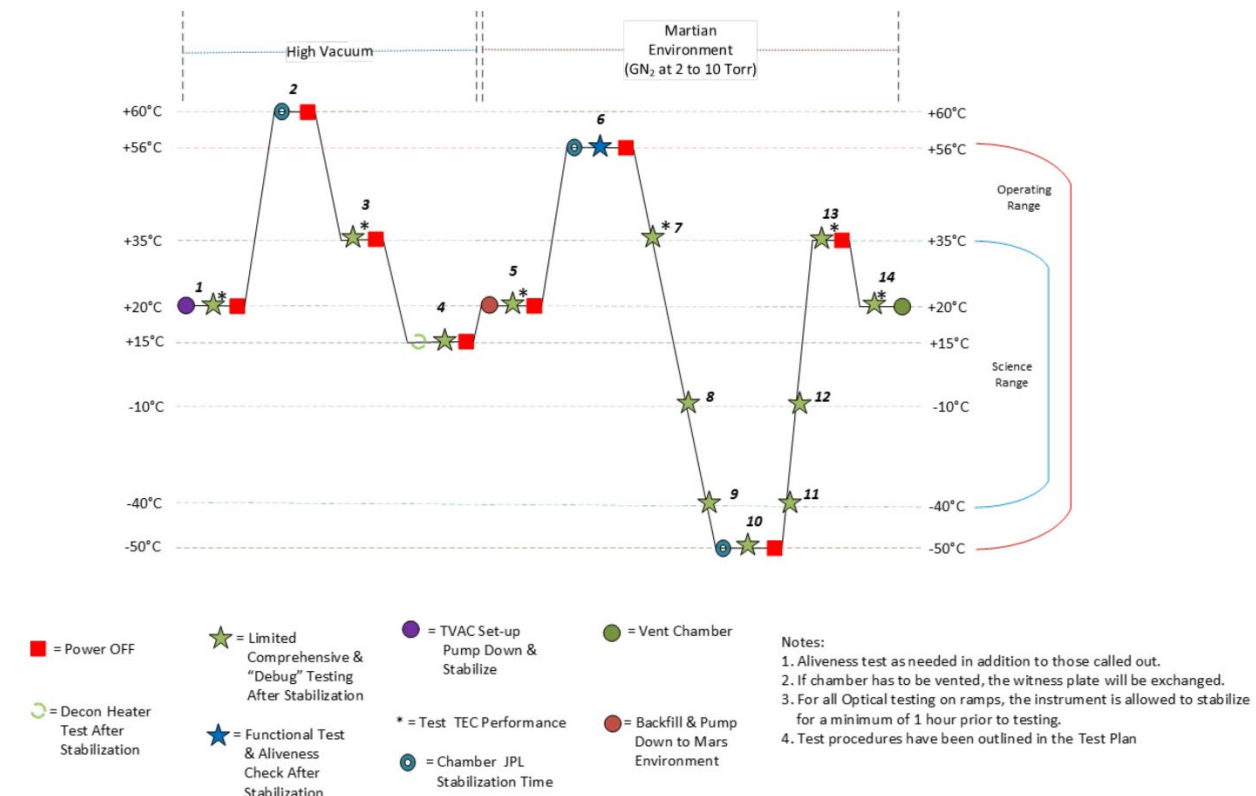


**Fig. 4.1** – A depiction of thermal-vacuum testing (TVAC) performed in order that the temperature-dependence of SuperCam’s CCD bias, dark current, EBI, wavelength and resolution could be quantified.

#### 4.2.1 CCD Bias

Before a given background or spectral acquisition, remnant charge in each CCD pixel is dumped in order that, in theory, only charge generated during spectral acquisition is recorded.

However, the CCD cleaning process is not instantaneous as detector rows are cleared sequentially, and so charge is generated by thermal processes between CCD cleaning and the start of a spectral acquisition. The temperature-dependence of SuperCam's CCD bias was modeled as a function of channel number and detector temperature. Note, the terms channel number and Transmission spectrometer are idiosyncratic labels used within the SuperCam team to describe a column of a detector where a single wavelength is recorded, and the part of the spectrometer where visible light is recorded, respectively. The detector temperature value is the average of 3 thermocouple temperature measurements taken before and after each measurement, and the CCD bias values increases exponentially with detector temperature. The origin of the CCD bias values will be discussed in the dark current section to follow shortly. For each channel in SuperCam, the temperature-dependence of the CCD bias was modeled in a likewise fashion, and the composite of all of these N models gives the CCD bias at arbitrary channel numbers and detector temperatures. The CCD bias model for the Transmission spectrometer is shown in **Fig. 4.2.**

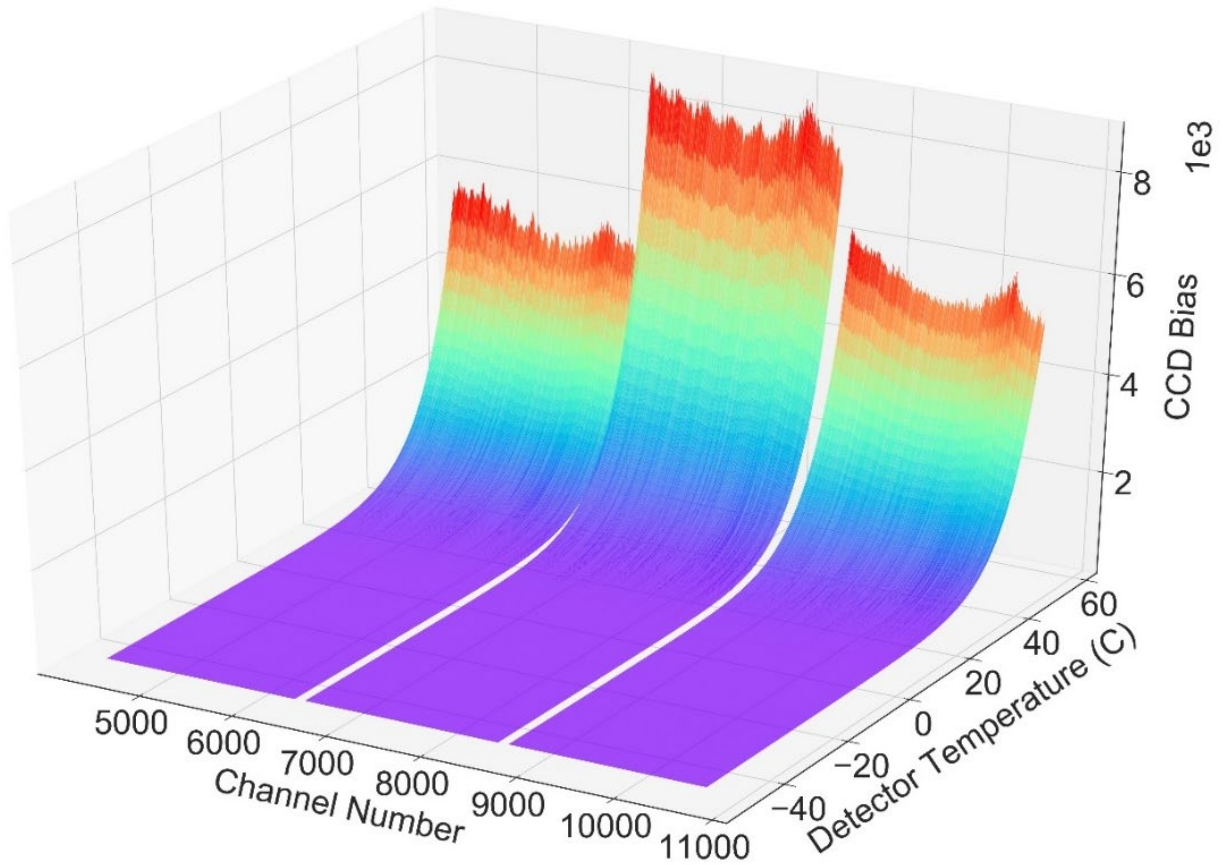


**Fig. 4.2** – The CCD bias as a function of channel number and detector temperature for the Transmission spectrometer.

#### 4.2.2 Dark Current

Dark current is generated when electrons transition from the ground-state to the conduction band in a CCD pixel by overcoming the silicon bandgap energy. The silicon bandgap energy may be approximated by the empirical formula (Pankove 1971) described in Eq. (4.1). Note that as the temperature increases, the silicon bandgap energy narrows and therefore the transition probability increases.

$$E_g = 1.1557 - \frac{7.021 \times 10^{-4} T^2}{1108 + T} \quad (4.1)$$

The rate of dark current generation is exponentially dependent upon temperature, and follows the relations stated in Eq. (4.2) and (4.3).

$$D_R(e^-) = CT^{1.5}e^{-E_g/2kT} \quad (4.2)$$

$$D = D_R(e^-)t \quad (4.3)$$

where  $D_R(e^-)$  is the average dark current in units of electrons per second per pixel,  $C$  is a constant, and  $T$  is the temperature in Kelvin. Note that  $D$ , dark counts per pixel, is linearly dependent upon  $t$ , the integration time.

In TVAC testing, backgrounds were collected at varying integration times and temperatures. The rate of dark count generation was found by plotting dark counts per channel versus integration time at fixed temperature, where the slope of the linear regression represents  $D_R(e^-)$ , and the y-intercept represents the CCD bias. After completing the dark current time-dependence for each channel and test point, the resulting  $D_R(e^-)$  values were plotted against detector temperature for each channel, and the dark current temperature-dependence was calculated via Eq. (4.2). An illustration of the dark current temperature-dependence for the Transmission spectrometer is modeled in **Fig. 4.3**.

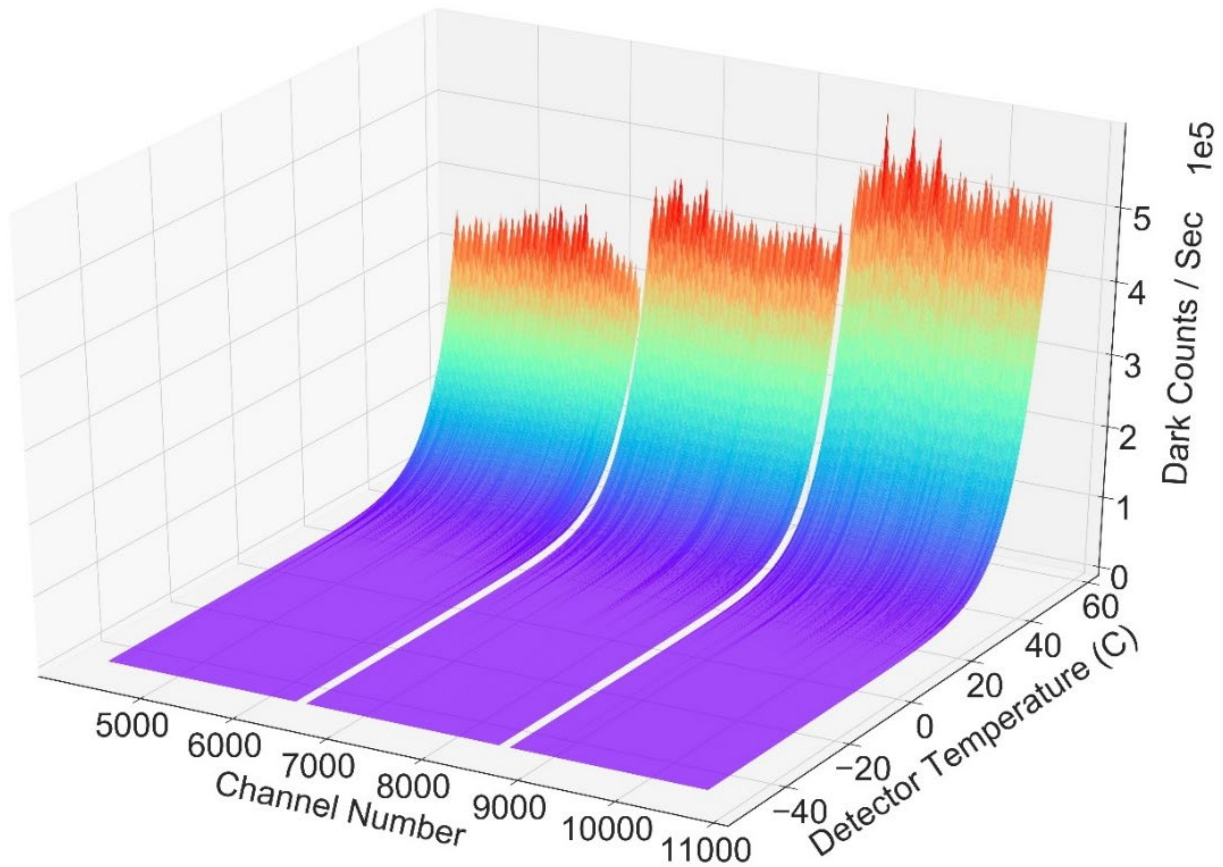


**Fig. 4.3** – Dark counts per second as a function of channel number and detector temperature for the Transmission spectrometer. As a general rule of thumb, dark signal doubles every  $\sim 7^{\circ}\text{C}$  for CCDs.

### 4.2.3 Effective Background Illumination

Effective background illumination (EBI) is an anachronistic expression for dark current produced by an image intensifier. As is the case for CCDs, electrons can be liberated at the intensifier by either heat or light. Unlike CCDs, these electrons are amplified as they transit through the micro-channel plate (MCP). Modeling EBI is more complicated than dark current though as it is exponentially dependent both on intensifier temperature and gain setting, as depicted in **Fig. 4.4** and **4.5**, respectively.

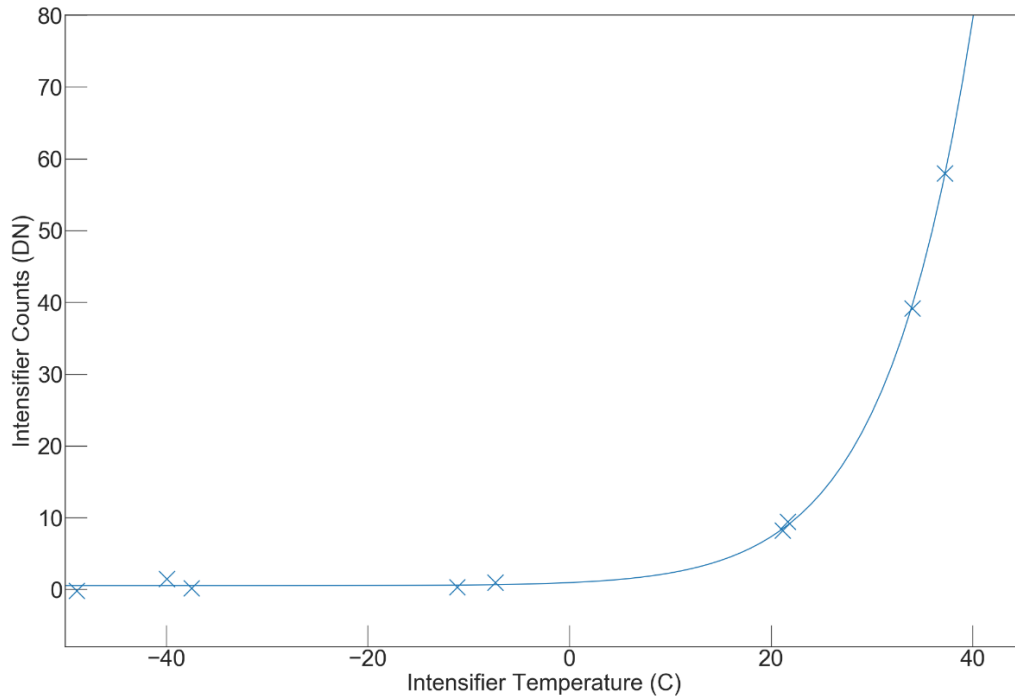


**Fig. 4.4** – The intensifier temperature-dependence on intensifier background counts (EBI) at gain setting 3200 and gate-width of 10 ms.

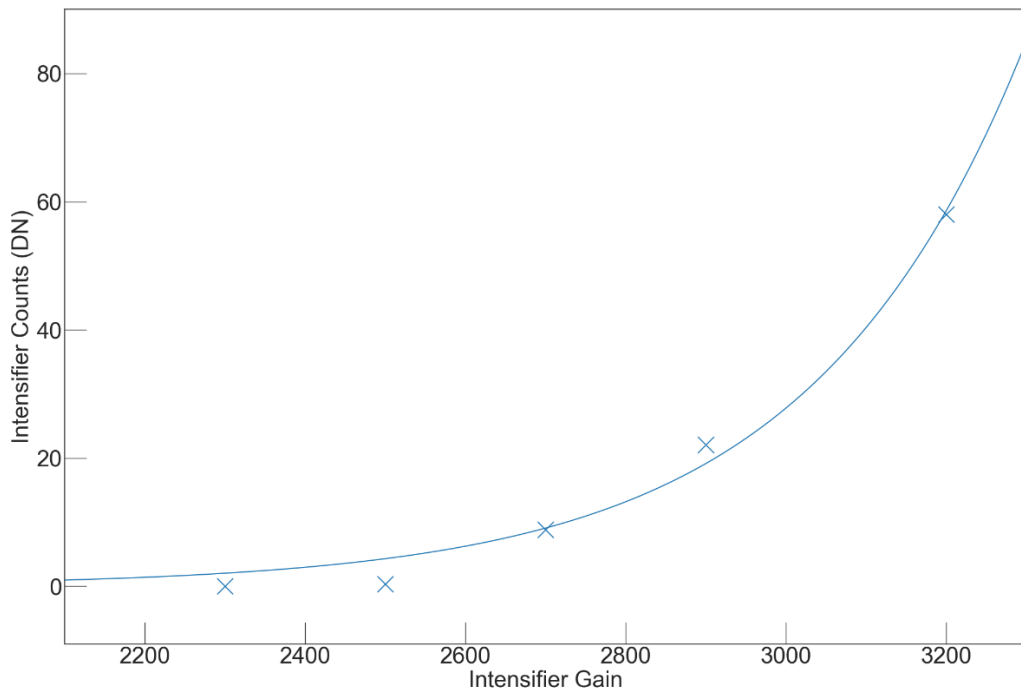


**Fig. 4.5** – The gain-dependence on intensifier background counts (EBI) for channel 5000 where the intensifier temperature was 37.2°C and the gate-width was 10 ms.

#### 4.2.4 Background Signal Model

Now that the principle contributors to the background signal have been characterized as a function of intensifier temperature, gain and gate width, along with detector temperature and integration time, it is possible to create artificial background signal estimates if environmental and acquisition parameters are known. Fortunately, SuperCam has temperature probes that return state-of-health data for each spectral acquisition, and so the ability to background-correct spectra via models is feasible. The benefit of utilizing background models in lieu of measured, in-situ backgrounds include minimizing opportunity cost by maximizing spectral acquisition time relative to background collection, monitoring the effect of radiation damage and lens darkening through time, and creating higher SNR background-corrected spectra via background models. To test the effectiveness of the background signal estimates, a background taken during TVAC, yet not included in the model, was compared with the model estimates for the reported temperatures and times. The results of this comparison are illustrated in **Fig. 4.6**. The background model performs exceedingly well in reproducing the measured background with the exception of dark spikes present in isolated channels. The prevalence of dark signal non-uniformity is quite evident in **Fig. 4.6**, which is typical for CCDs and can vary by as much as 10% at high signal levels (Janesick 2001 pg. 105).

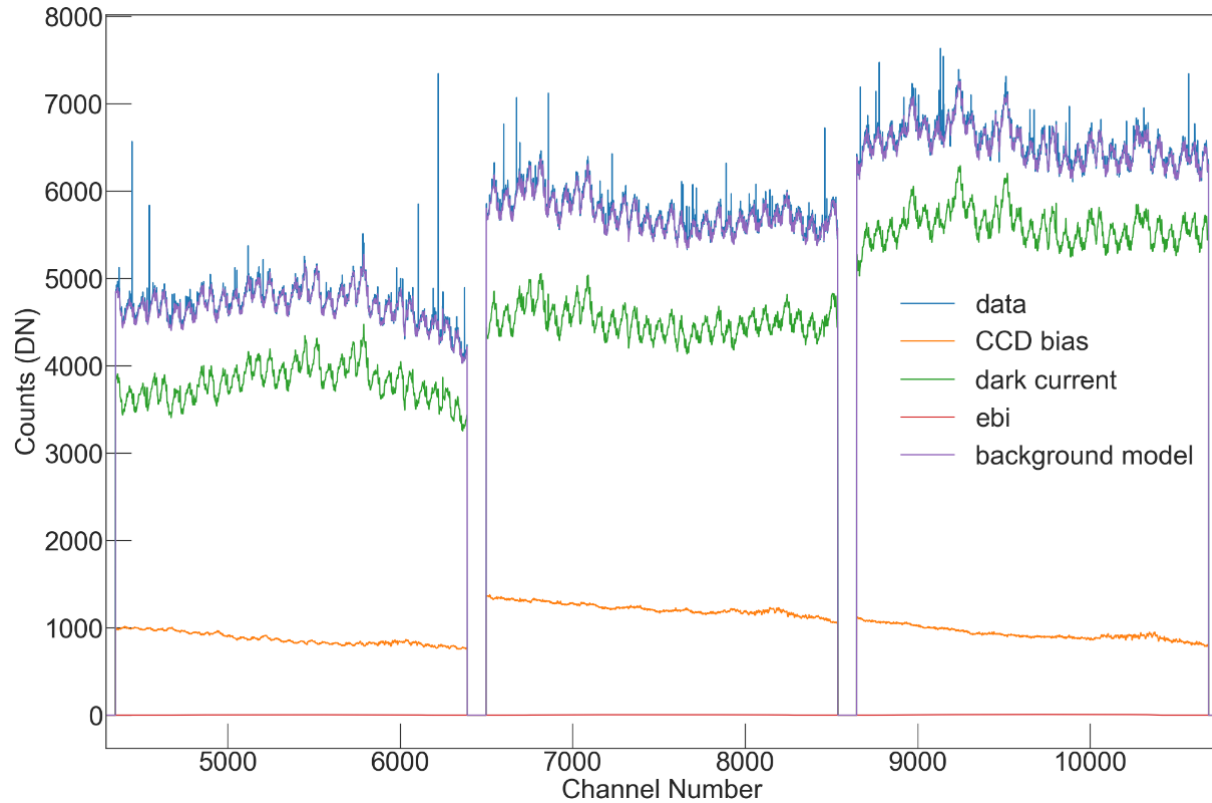


**Fig. 4.6** – Background model estimates versus measured background data. The background data was acquired with the following parameters  $T_{\text{detector}} = 38.9^{\circ}\text{C}$ ,  $T_{\text{intensifier}} = 37.2^{\circ}\text{C}$ ,  $t_{\text{detector}} = 106$  ms,  $t_{\text{intensifier}} = 100$  ms, and gain = 2300.

#### 4.2.5 Background Noise

The background signal sources described thus far are shot noise processes in that they generate constant DC currents with random fluctuations about that current. This claim can be verified qualitatively by plotting the mean of  $N$  backgrounds, the mean of  $N$  backgrounds  $\pm$  Poisson noise, and  $N$  individual backgrounds. Since the vast majority of datapoints of the  $N$  individual backgrounds fall within the shot noise bounds, the backgrounds can be accurately described by Poissonian noise. An instantiation of this claim is presented in **Fig. 4.7**.

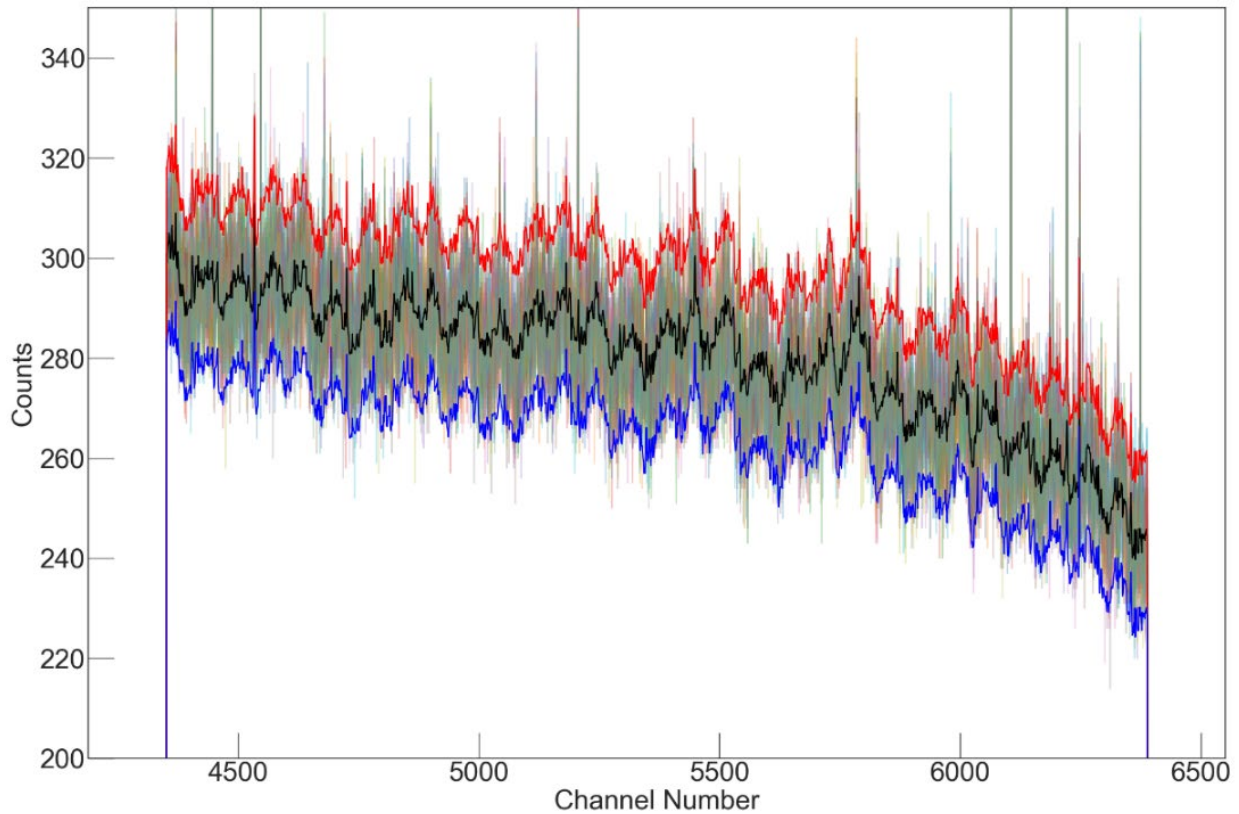


**Fig. 4.7** – A background model (black) for SuperCam with shot noise upper (red) and lower (blue) bounds versus 20 measured backgrounds plotted superimposed (semi-transparent). Nearly all the semi-transparent data points fall within the bounds, demonstrating that the background noise is a shot noise process.

#### 4.2.6 Photon Transfer Curves

Depending upon how many photon derived counts are present in a given pixel, that pixel will fall into differing noise regimes. As the number of photons striking a pixel increases, the pixel will transition from read to shot to fixed pattern to full well noise regimes. The boundary between these noise regimes can be defined from photon transfer curves (PTC) where signal-to-noise ratios are plotted against signal levels, and the slope of the curve determines which noise source is dominant. A generic PTC curve is shown in **Fig. 4.8** that illustrates the relevant trends.

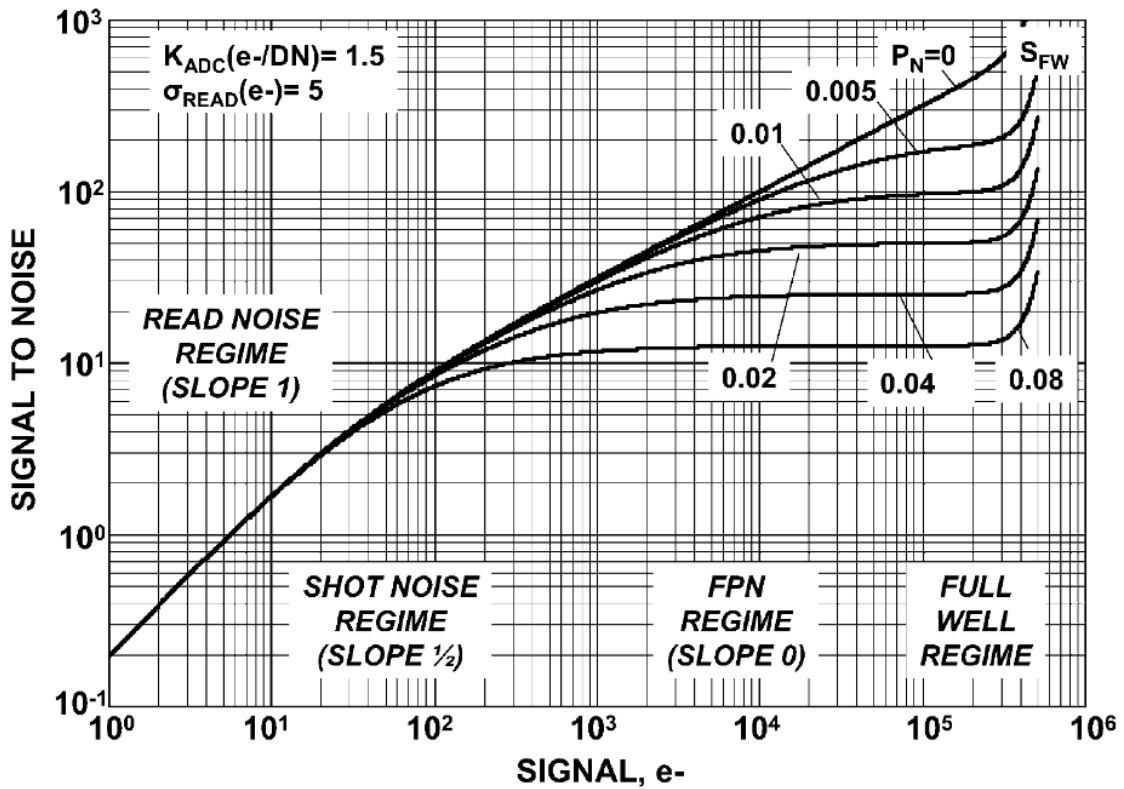
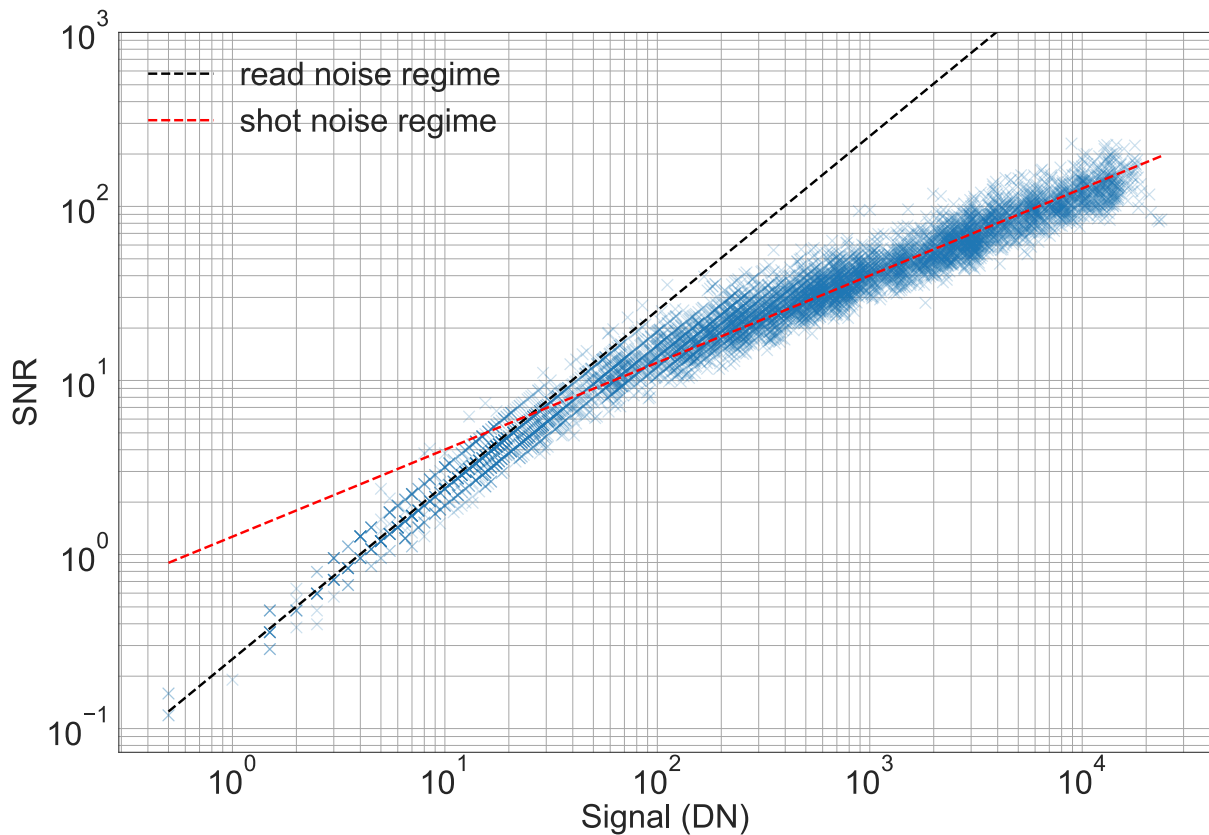


Fig. 4.8 – A typical photon transfer curve where SNR is plotted against signal, and the slope of the line defines the dominate noise source (see figure annotations). This figure copied from (Janesick 2007).

In TVAC testing, a deuterium-tungsten halogen lamp was measured repeatedly as a function of intensifier gain, intensifier gate width, intensifier temperature, detector integration time and detector temperature. The output of the lamp source is sufficiently stable to assume that the signal level is constant (i.e. light source output  $\leq 0.1\%$  per hour at 254 nm), and that the variation in recorded intensity in a given channel from measurement to measurement is the result of noise being sampled at different places in SuperCam’s noise profile. If  $N$  measurements are made at fixed experimental acquisition parameters, then the signal can be defined as the median signal per channel of  $N$  measurements, the noise as the median absolute deviation per channel of  $N$

measurements, and the SNR as the ratio of those two quantities. Plotting the result of this experiment in a form analogous to **Fig. 4.8** reveals the signal levels in which SuperCam is dominated by various noise regimes. Those results are presented in **Fig. 4.9**. The boundary between one noise regime and another defines the ideal set of acquisition parameters. From the read to fixed pattern noise regimes, the SNR increases with signal, and so increasing the integration time increases the SNR of the spectra obtained. However, once the detector transitions into the fixed-pattern noise regime, SNR remains flat with increasing signal and so integrating beyond this limit serves no purpose.



**Fig. 4.9** – SNR vs signal PTC plot for SuperCam’s Green ROI in the absence of dark current noise. The crossing of the read (slope = 1) and shot noise (slope = 1/2) regime lines indicates the transition from one noise regime to another.

In **Fig. 4.9**, the PTC shown possessed no dark current nor dark current shot noise because the data used to generate the plot was taken at a detector temperature of  $-46.2^{\circ}\text{C}$ . The purpose of the illustration was to demonstrate SuperCam's lower limits of sensitivity when background noise is minimal. However, SuperCam will not operate at such ideal conditions on Mars. SuperCam's detector is expected to operate at temperatures ranging from  $-20^{\circ}\text{C}$  to  $15^{\circ}\text{C}$  with thermoelectric coolers turned on, and SuperCam's intensifier is expected to operate at  $+20^{\circ}\text{C}$  warmer than that. Fortunately, data at such temperatures was collected in TVAC, which facilitates the quantification of SuperCam's SNR temperature-dependence. The negative effects of dark current shot noise on SNR is depicted in **Fig. 4.10**. As the temperature increases (indicated by the blue to red colormap), the SNR attained at fixed signal is diminished relative to the  $-46.2^{\circ}\text{C}$  measurement until the photon noise regime is reached around 2,000 counts. At this boundary, the magnitude of noise generated from the background is insignificant relative to the noise generated by photons. At  $\sim 5,000$  counts, SuperCam enters the fixed pattern noise regime, meaning that collection of additional photons would not result in increased SNR. Fixed pattern noise, caused by pixel-to-pixel nonuniformity in response to photons, can be corrected by appropriate application of flatfield corrections. Upon correction, fixed pattern noise is eliminated and the shot noise domain extended to full well (i.e.  $\sim 65,000$  counts).

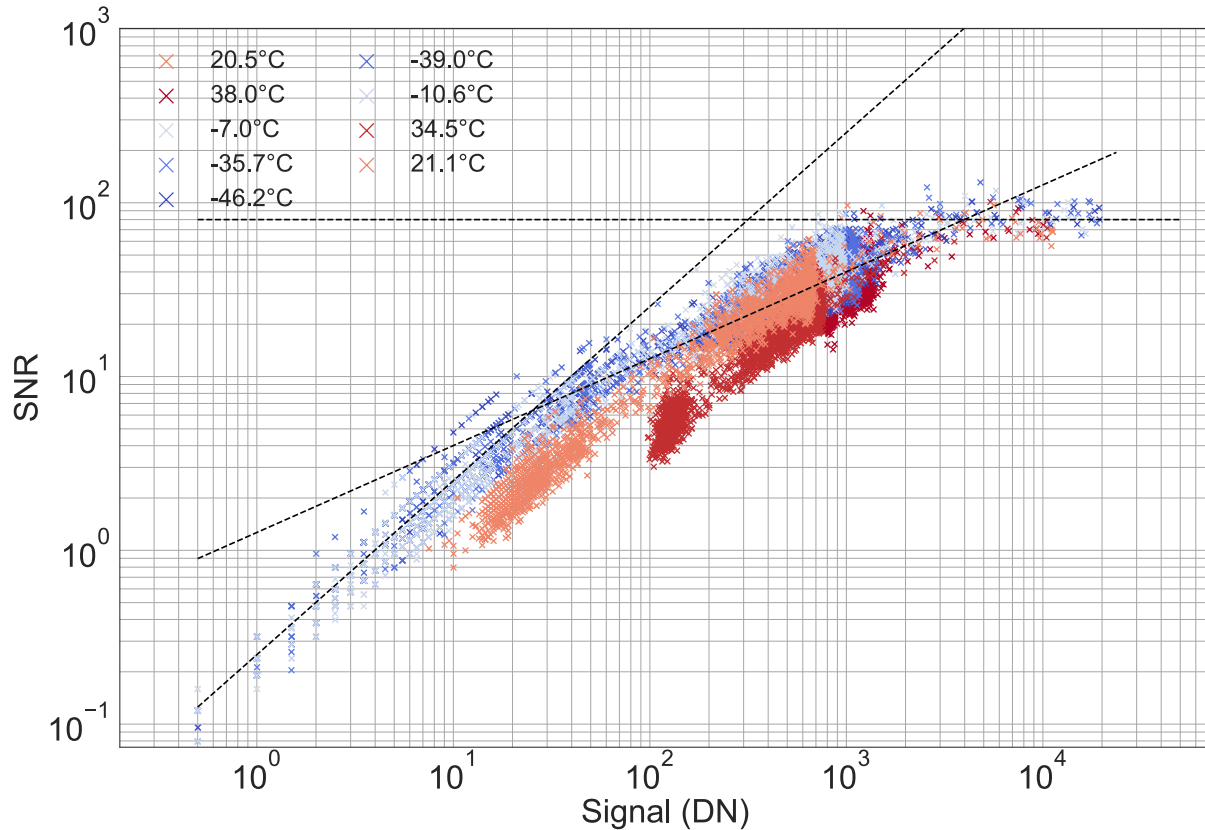


**Fig. 4.10** – The SNR vs signal PTC as a function of temperature (range  $-46.2^{\circ}\text{C}$  to  $38.0^{\circ}\text{C}$ ) for the deuterium-tungsten halogen lamp as measured by SuperCam’s Transmission spectrometer (Green ROI). The dotted lines represent three noise regimes experienced by SuperCam, namely read, shot and fixed pattern, that may be distinguished by their slopes. Read noise is defined by a slope of one; shot noise by slope of one-half; fixed pattern by slope of zero.

### 4.3 Raman and Luminescence Detection Limits

The deuterium-tungsten halogen lamp used to generate the photon transfer curves presented thus far are representative of passive-sensing spectroscopy (e.g. Vis-NIR), not laser-induced active-sensing spectroscopic measurements (e.g. LIBS, LAMES, Raman and luminescence). In active-sensing measurements, additional considerations must be taken into account, specifically fluctuations in laser irradiance within the field-of-view of the spectrometer. In pursuit of this

aim, photon transfer curves were generated from laser-induced Raman and luminescence spectra as well. As depicted in **Fig. 4.11**, SuperCam does not achieve shot-noise limited spectroscopy in active-sensing mode (i.e. slope  $\neq 0.5$ ) at high gain settings. Instead, the maximal slope achieved in the PTC is  $\sim 0.35$ , caused either by laser-induced flicker noise, spatial nonuniformities in response to photons of the micro-channel plate or detector. One reasonable conclusion by comparison of **Fig. 4.8** and **4.11** is that the Raman and luminescence PTC suffers from increased spatial nonuniformities (i.e.  $P_N = 0.04$ ), which could be caused by an increase in the intensifier gain setting used during Raman and luminescence measurements (i.e. gain setting 3200) relative to the deuterium-tungsten halogen lamp (i.e. gain 2300) measurements that amplifies those nonuniformities. As mentioned previously, this can be eliminated by appropriate flat-fielding. If the cause is laser flicker, then the reduced slope is intrinsic to the instrument design, and can be minimized only by summing multiple laser pulses on the CCD per spectral acquisition since the variance in laser irradiance within the field-of-view of  $N$  summed laser pulses will be less than the variance between individual pulses.

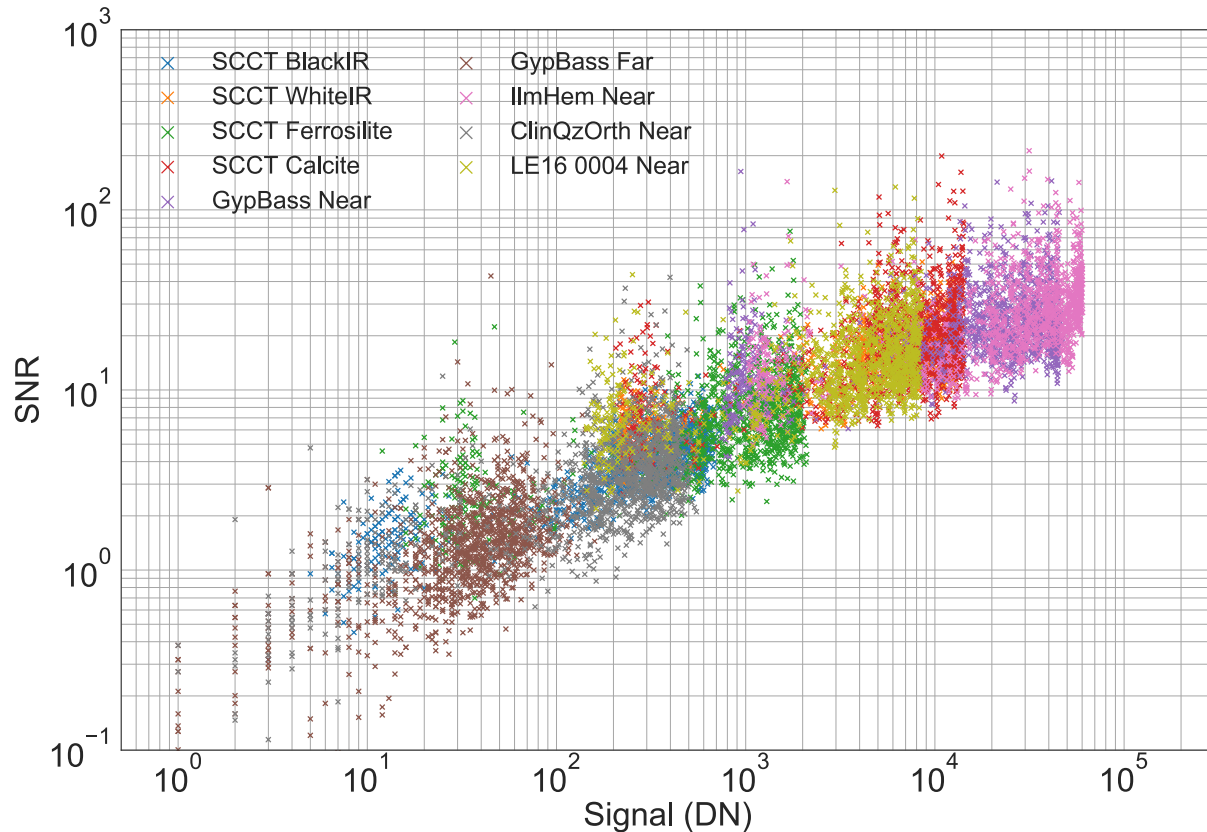


**Fig. 4.11** – SNR vs signal PTC for active-sensing Raman measurements of SuperCam’s transmission spectrometer (Orange ROI) taken during STT.

#### 4.4 Tracking Raman Photons from Source to Detector

An important detail in SuperCam’s Raman detection capabilities is the fact that the laser beam covers a significantly larger area than the 0.74 mrad FOV of the telescope and spectrometer for targets at close distance. As distance increases, losses due to the decreasing solid angle of the telescope from the target become significant and temperature-dependent co-alignment of the laser beam and spectrometer FOV affects the signal (Maurice 2021). Here we discuss the number of Raman photons detected from a test made at different distances.

The rate of Raman photon generation for a given sample is governed by the differential Raman scattering cross-section (i.e.  $\text{cm}^2 \text{sr}^{-1} \text{molecule}^{-1}$ ) of a target molecule, the number of molecules of a given species that are illuminated, and the irradiance of the excitation source within the FOV. To gauge the number of Raman photons collected at SuperCam's entrance aperture, and the photocathode of SuperCam's intensifier, a cross-calibration study was performed at the University of Hawai'i at Mānoa of the Raman scattering cross-section of cyclohexane and Raman efficiency of a pressed pellet sample of gypsum powder. In the cross-calibration study, UH's remote Raman spectrometer, described previously (Gasda 2015), was radiometrically calibrated by a Labsphere calibrated lamp. The radiometric calibration was verified by measuring the differential Raman-scattering cross section of cyclohexane's  $801.3 \text{ cm}^{-1}$  Raman mode. Measurements were made with both 1 cm and 1 mm length Starina cells, which agreed well. The measured differential Raman scattering cross-section was found to be  $4.58 \times 10^{-30} \text{ cm}^2 \text{sr}^{-1} \text{molecule}^{-1}$ , which was within 1% of the published values (Trulson 1986; Acosta-Maeda 2016) for that differential Raman cross-section. A field-stop, placed at the sample location 6.11 meters from the primary mirror of UH's Raman spectrometer, circumscribed the projection of the spectrometer's entrance slit at the sample location so that the laser energy within the FOV of the spectrometer at the sample location could be measured directly. After verifying the accuracy of the instrument response function (IRF), the Raman efficiency of gypsum's  $\nu_1$  emission at  $1008 \text{ cm}^{-1}$  was determined to be  $2.04 \times 10^{-8}$ , which is in general agreement with published values of gypsum samples (Stopar 2005).

The gypsum sample was observed by SuperCam as a function of distance. The Raman spectrum of gypsum was corrected from counts (DN) at the CCD to photons at the aperture by application of the IRF. Following the IRF correction, the spectra were corrected by geometrical

factors to convert photons at the entrance aperture to Raman photons emitted at the source, assuming Lambertian scattering into  $\pi$  sr. The results of this experiment are presented in **Fig. 4.12**. Three regions of the plot are readily distinguishable. First, the Raman photons per pulse within the FOV of the transmission spectrometer increases with distance as the FOV encapsulates a greater proportion of the laser beam (Maurice 2021). Second, the number of Raman photons plateaus as the portion of the laser beam with the highest energy density apparently starts to fall outside of the spectrometer FOV. Third, the number of Raman photons within the FOV declines as this effect outweighs the expanded spectrometer FOV. Three images indicating the laser beam profile and the spectrometer FOV as a function of distance are also shown in **Fig. 4.12**. The FOV, represented by the circle at the center of image, is shown in perfect alignment (i.e. 0 mrad) with the Raman laser spot. However, in real-world measurements, very slight (i.e.  $< 0.35$  mrad) misalignment results from telescope temperature variations (Maurice 2021), causing the laser spot to deviate relative to the spectrometer FOV, so more or less light is captured by the spectrometer FOV. As the distance increases, the coupling efficiency of the laser spot to the FOV decreases for a given misalignment angle.

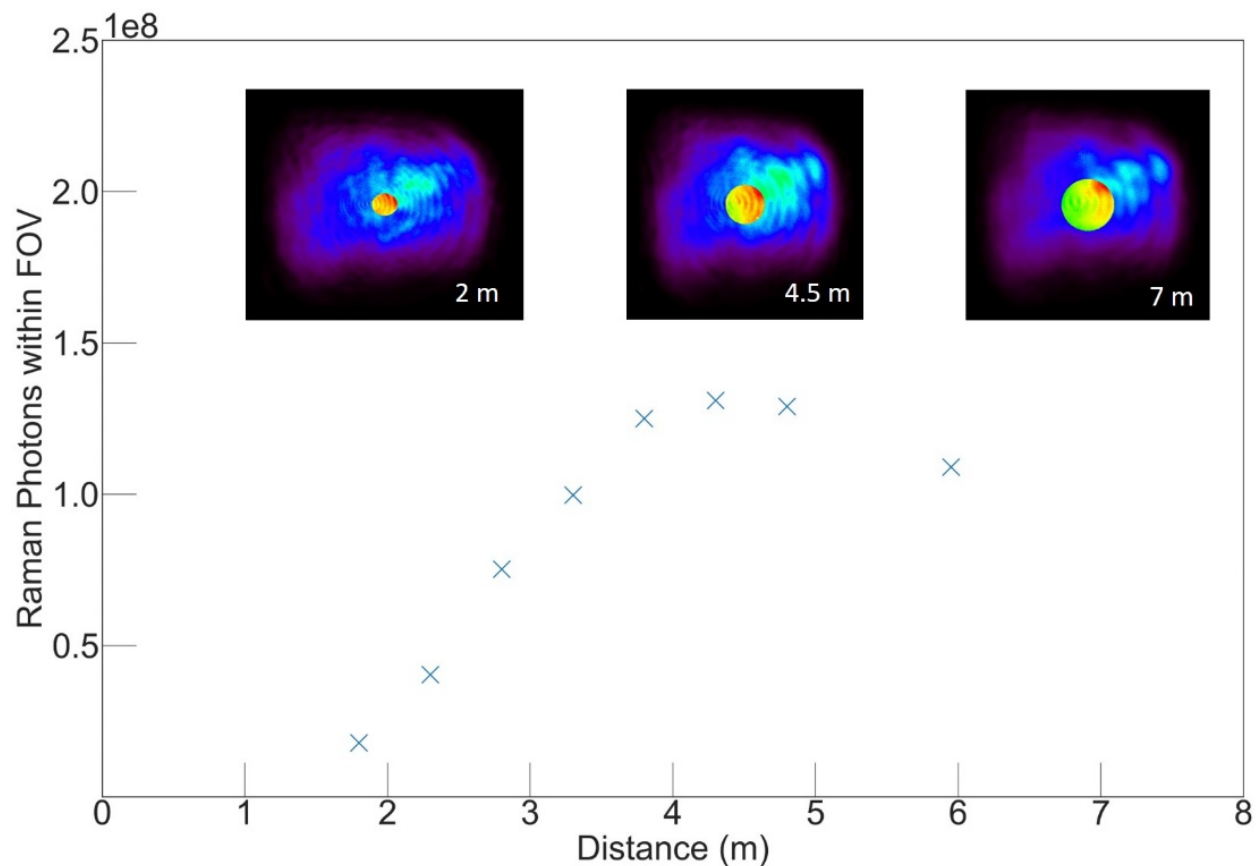


**Fig. 4.12** – An illustration of the number of Raman photons scattered (e.g. gypsum’s  $\nu_1$  band) within SuperCam’s FOV for as a function of distance. As distance increases, the overlap between SuperCam’s FOV and laser spot increases. At large distances, slight misalignment angles cause the total energy captured by the FOV to decline.

For highly amplified systems like SuperCam’s Raman spectrometer, detection limits may be understood by defining the minimum number of photons striking the photocathode, before amplification occurs, in order to achieve a signal-to-noise ratio (SNR) equal to one. This number is not given by the instrument response since the IRF also includes the amplification of the photons between the intensifier photocathode and the CCD. Analysis of the gypsum pellet vs. distance experiment, detailed in **Table 4.1**, determined that at least four photons are required to strike the photocathode for 562 nm light at  $-10^\circ\text{C}$  to achieve a SNR greater than one. Four

photons striking the photocathode represents a lower limit estimation of SuperCam’s detection limit as 562 nm light is near SuperCam’s transmission efficiency maxima of 6% and the CCD temperature was held constant at temperature lower than that expected in the field on Mars. In cases where the transmission efficiency is not as high (e.g. the lattice mode region below 541 nm) or at higher temperatures where thermal noise is more prevalent, a greater number of photons will need to be collected to attain a SNR greater than one.

**Table 4.1** Propagation of Raman photons from source to detector for gypsum  $\nu_1$  emission.

| <b>Distance (m)</b> | <b>Source</b> | <b>Aperture</b> | <b>Photocathode</b> | <b>Detector</b> | <b>SNR</b> |
|---------------------|---------------|-----------------|---------------------|-----------------|------------|
| 1.8                 | 1.79e7        | 4824            | 305                 | 8474            | 9.3        |
| 2.3                 | 4.04e7        | 4081            | 256                 | 7104            | 9.0        |
| 2.8                 | 7.52e7        | 3478            | 219                 | 6085            | 7.8        |
| 3.3                 | 9.97e7        | 2397            | 152                 | 4206            | 6.3        |
| 3.8                 | 1.25e8        | 1705            | 109                 | 3012            | 5.8        |
| 4.3                 | 1.31e8        | 1080            | 68                  | 1894            | 4.3        |
| 4.8                 | 1.29e8        | 686             | 43                  | 1194            | 3.0        |
| 5.95                | 1.09e8        | 247             | 14                  | 376             | 2.1        |

Units are photons between the FWHM of the Raman peak per laser pulse. For the source emission, only photons produced within the spectrometer FOV are counted, resulting in an increase between 1.8 and 3.8 m, a plateau between 3.8 to 4.8 m, and declining irradiance within the FOV at longer distances.

## 4.5 Summary

The ability of remote-sensing Raman spectrometers to record Raman spectra depends upon their ability to collect enough photons to surpass their background noise floors. For pulsed, time-resolved remote-sensing Raman spectrometers (e.g. SuperCam), background noise is dominated by three principle background signal sources, specifically CCD bias, dark current and EBI. In this work, we characterized the magnitude of these background signal sources as a function of temperature and time, finding that a minimum of four photons are required to strike the photocathode of the intensifier to attain a SNR greater than one when the instrument is kept at -10°C.

## Chapter 5. Summary

The advent of ChemCam's laser induced breakdown spectrometer (LIBS) aboard the Mars Curiosity rover brought about a new era of mid-range active laser remote-sensing on the surface of another planetary body. Laser remote-sensing is superior to contact science instruments in that laser remote-sensing instruments can acquire spectral data without the need for sample preparation, characterize a greater number of sample targets in a prescribed time period, and acquire spectral data from sample targets that are inaccessible to a rover's arm. While ChemCam successfully demonstrated active-sensing spectroscopy on the surface of another planetary body, its principle spectroscopic mode, LIBS, could only infer the arrangement of atoms in a given sample via stoichiometry, thus limiting the characterization of polymorph minerals that form in distinct environments. Raman spectroscopy, set for Mars aboard the Perseverance, ExoMars and MMX rovers, is highly sensitive to the arrangement of atoms within a given molecule, allowing for the unambiguous detection of biominerals and polymorphs. Unfortunately, Raman efficiencies are quite faint, producing only one Raman photon for every 100 million laser photons. Therefore, the ultimate goal in designing remote-sensing Raman spectrometers is to maximize the throughput-resolution product. In conventional grating Raman spectrometers, the entrance slit width is set to 50  $\mu\text{m}$  so that 10-12  $\text{cm}^{-1}$  wavenumber resolution can be achieved. The narrowness of the entrance slit width causes a diminution in the throughput of light through the spectrometer and thus limits sensitivity. Interferometers circumvent the need for narrow entrance slits to produce high-resolution spectra by sampling spectral light in Fourier space as amplitude or frequency modulated interferograms. In these cases, resolution is governed by the Rayleigh criterion, which states that the resolution limit is defined as the minimum change in wavelength that causes a change of half a fringe period across the N detector array elements. As

a tradeoff for the lack of an entrance slit, every spectral feature is sampled by all  $N$  detector elements simultaneously, meaning that photon noise associated with any one spectral feature contributes noise equally to every other spectral feature also, a phenomenon known as the multiplex disadvantage. In the present work, the capabilities of dispersive and interferometric remote-sensing Raman spectrometers have been effectively demonstrated.

## References Cited

- Acosta T.E, Scott E.R.D., Sharma S.K., & Misra A.K. (2013) The pressures and temperatures of meteorite impact: Evidence from micro-Raman mapping of mineral phases in the strongly shocked Taiban ordinary chondrite. *American Mineralogist*, 98, 859–869.
- Acosta-Maeda T.E., Misra A.K., Muzangwa L.G., Berlanga G., Muchow D., Porter J. & Sharma S.K. (2016) Remote Raman measurements of minerals, organics, and inorganics at 430 m range. *Applied Optics*, 55(36), 10283-10289.
- Acosta-Maeda T.E., Misra A.K., Porter J.N., Bates D.E. & Sharma S.K. (2017) Remote Raman efficiencies and Cross-Sections of Organic and Inorganic Chemicals. *Applied Spectroscopy*, 71(5), 1025-1038.
- Adams D.M. & Newton D.M. (1970a) Tables for factor group analysis of the vibrational spectra of solids. *Journal of the Chemical Society A*, 1970, 2822–2827.
- Adams D.M. & Newton D.M. (1970b) Tables for Factor Group Analysis. Beckman-RICC Ltd., Reading, UK.
- Adams D.M., Sharma S.K., & Appleby R. (1977) Spectroscopy at very high pressures: Part 14. Laser Raman scattering in ultra-small samples in the diamond anvil cell. *Applied Optics*, 16, 2572–2575.
- Aminzadeh, A. (1997) Fluorescence bands in the FT-Raman spectra of some calcium minerals. *Spectrochimica Acta*, A53, 693–797.
- Angel S.M., Carrabba M., & Cooney T.F. (1995) The utilization of diode lasers for Raman spectroscopy. *Spectrochimica Acta*, A51, 1779–1799.

- Angel S.M., Gomer N.R., Sharma S.K., & McKay C. (2012) Remote Raman spectroscopy for planetary exploration: A review. *Applied Spectroscopy*, 66, 137–150.
- Arns J.A. (1995) Holographic transmission gratings improve spectroscopy and ultrafast laser performances. *Proceedings of the Society of Photo-optical Instrumentation Engineers*, 2404, 174–181.
- Arns J.A., Colburn W.S., & Barden S.C. (1999) Volume phase gratings for spectroscopy, ultrafast laser compressors, and wavelength division multiplexing, *Proceedings of the Society of Photo-optical Instrumentation Engineers*, 3779, 313–323.
- Aroyo M.I., Perez-Mato J.M., Capillas C., et al. (2006a) Bilbao crystallographic server I: Databases and crystallographic computing programs. *Zeitschrift für Kristallographie*, 221, 15–27.
- Aroyo M.I., Kirov A., Capillas C., Perez-Mato J.M., & Wondratschek H. (2006b) Bilbao crystallographic server II: Representations of crystallographic point groups and space groups. *Acta Crystallographica*, A62, 115–128.
- Aroyo M.I., Perez-Mato J.M., Orobengoa D., Tasci E., de la Flor G., & Kirov A. (2011) Crystallography online: Bilbao crystallographic server. *Bulgarian Chemistry Communications*, 43, 183–197.
- Barnett P.D. & Angel S.M. (2016) Miniature Spatial Heterodyne Raman Spectrometer with a Cell Phone Camera Detector. *Applied Spectroscopy*, 71(5), 988-995.

- Barnett P.D., Strange K.A. & Angel S.M. (2017) Improving Spectral Results Using Row-by-Row Fourier Transform of Spatial Heterodyne Raman Spectrometer Interferogram. *Applied Spectroscopy*, 71(6), 1380-1386.
- Batley D.E., Slater J.B., Wludyka R., Owen H., Pallister D.M., & Morris M.D. (1993) Axial transmissive f/1.8 imaging Raman spectrograph with volume-phase holographic filter and grating. *Applied Spectroscopy*, 47, 1913–1919
- Beegle L.W., Bhartia R., DeFlores L., et al. (2014) SHERLOC: Scanning habitable environments with Raman and luminescence for organics and chemicals, an investigation for 2020. In: *Proceedings of the 45th Lunar Planetary Science Conference*, Abstract #2835.
- Beegle L., Bhartia R., White M., DeFlores L., et al. (2015) SHERLOC: Scanning habitable environments with Raman & Luminescence for organics & chemicals. 2015 IEEE Aerospace Conference.
- Behr B.B., Hajian A.R., Cenko A.T., Murison M., McMillan R.S., Hindsley R. & Meade J. (2009) Stellar Astrophysics with a Dispersed Fourier Transform Spectrograph I. Instrument Description and Orbits of Single-Lined Spectroscopic Binaries. *Astrophysical Journal*, 705, 543-553.
- Bennett C.J., Brotton S.J., Jones B.M., Misra A.K., Sharma S.K., & Kaiser R.I. (2013) A novel high sensitivity Raman spectrometer to study pristine and irradiated interstellar ice analogs. *Analytical Chemistry*, 85, 5659–5665.
- Bertie J.E. & Bell, J.W. (1971) Unit cell group and factor group in the theory of the electronic and vibrational spectra of crystals. *Journal of Chemical Physics*, 54, 160–162.

- Bhagvantam S. (1940) Effect of crystal orientation on the Raman spectrum of calcite. Proceedings of the Indian Academy of Sciences A, 11, 62–71.
- Bhagavantam S. & Venkatarayudu T. (1939) Raman effect in relation to crystal structure. Proceedings of the Indian Academy of Sciences A, 9, 224–258.
- Bhagavantam S. & Venkatarayudu T. (1969) Theory of Groups and Its Applications to Physical Problems. Academic Press, New York.
- Bibring J.P., Langevin Y., Mustard J.F., Poulet F., et al. (2006) Global Mineralogical and Aqueous Mars History Derived from OMEGA/Mars Express Data. *Science*, 312(5772), 400-404.
- Bischoff W.D., Sharma S.K. & MacKenzie F.T. (1985) Carbonate ion disorder in synthetic and biogenic magnesian calcites: a Raman spectral study. *American Mineralogist*, 70(5-6), 581-589.
- Bishop J.L. & Murad E. (2004) Characterization of minerals and biogeochemical markers on Mars: A Raman and IR spectroscopic study of montmorillonite. *Journal of Raman Spectroscopy*, 35(6), 480-486.
- Blacksberg J., Rossman G.R., & Gleckler A. (2010) Time-resolved Raman spectroscopy for in situ planetary mineralogy. *Applied Optics*, 49, 4951–4962.
- Blacksberg J., Alerstam E., Maruyama Y., Cochrane C.J., & Rossman G.R. (2016) Miniaturized time-resolved Raman spectrometer for planetary science based on a fast single photon avalanche diode detector array. *Applied Optics*, 55, 739–748.

- Breitenfeld L.B., Dyar M.D., Carey C.J., Tague T.J., et al. (2018) Predicting olivine composition using Raman spectroscopy through band shift and multivariate analyses. *American Mineralogist*, 103(11), 1827-1836.
- Bridges J.C., Catling D.C., Saxton J.M., Swindle T.D., Lyon I.C. & Grady M.M. (2001) Alteration Assemblages in Martian Meteorites: Implications for Near-Surface Processes. *Space Science Reviews*, 96, 365-392.
- Brown A.J., Viviano C.E. & Goudge T.A. (2018) Olivine-Carbonate Mineralogy of Jezero Crater. (2018) arxiv:1801.09841.
- Buback M. & Schulz K.R. (1976) Raman scattering of pure ammonia at high pressures and temperatures. *Journal of Physical Chemistry*. 80, 2478-2482.
- Carter J.C., Scaffidi J., Burnett S., Vasser B., Sharma S.K., & Angel S.M. (2005), Stand-off Raman detection using dispersive and tunable filter based systems. *Spectrochimica Acta*, A61, 2288–2298.
- Chase D.B (1986) Fourier transform Raman spectroscopy. *Journal of the American Chemical Society*, 108, 7485–7488.
- Chio C.H., Sharma S.K. & Muenow D.W. (2004) Micro-Raman studies of gypsum in the temperature range between 9 K and 373 K. *American Mineralogist*, 89(2-3), 390-395.
- Christensen P.R., McSween H.Y., Bandfield J.L., Ruff S.W., et al. (2005) Evidence for magmatic evolution and diversity on Mars from infrared observations. *Nature*, 436, 504-509.

- Clarkson J. & Smith W.E. (2003) A DFT analysis of the vibrational spectra of nitrobenzene. *Journal of Molecular Structure*, 655, 413-422.
- Colthup N.B., Daly L.H., & Wiberley S.E. (1975) *Introduction to Infrared and Raman Spectroscopy*, 2nd edn. Academic Press, New York.
- Connes P. (1958) Spectromètre interférentiel à selection par l'amplitude de modulation. *Journal de Physique et le Radium*, 19, 215-222.
- Cooney J.A. (1965) Remote Observations Using Raman Component of Laser Backscatter. *Proceedings of the Symposium on Electromagnetic Sensing of the Earth from Satellites*. Polytechnic Press.
- Cooney T.F. & Sharma S.K. (1990) Structure of glasses in the system  $Mg_2SiO_4$ - $Fe_2SiO_4$ ,  $Mn_2SiO_4$ - $Fe_2SiO_4$ ,  $Mg_2SiO_4$ - $CaMgSiO_4$  and  $Mn_2SiO_4$ - $CaMnSiO_4$ . *Journal of Non-Crystalline Solids*, 122, 10-32.
- Cooney T.F., Skinner H.T., & Angel S.M. (1995) Evaluation of external-cavity diode lasers for Raman spectroscopy. *Applied Spectroscopy*, 49, 1846-1851.
- Cooper J.B., Flecher P.E., Albin S., Vess T.M., & Welch W.T. (1995) Elimination of mode hopping and frequency hysteresis in diode laser Raman spectroscopy: The advantages of a distributed Bragg reflector diode laser for Raman excitation. *Applied Spectroscopy*, 49, 1692-1698.
- Cornell R.M. & Schwertmann U. (2003) *The Iron Oxides. Structure, Reactions, Occurrences and Uses*, 2nd edn. Wiley-VCH Verlag GmbH & Co. KGaA, Weinheim, Germany.
- Cotton F.A. (1963) *Chemical Applications of Group Theory*. Wiley-Interscience, New York.

- Damen T.C., Porto S.P.S., & Tell B. (1966) Raman Effect in zinc oxide. *Physical Review*, 142, 570–574.
- DeAngeles B. A., Newnham R.E., & White W.B. (1972) Factor group analysis of the vibrational spectra of crystals: A review and consolidation. *American Mineralogist*, 57, 255–268.
- de Faria D.L.A., Venâncio Silva S, & de Oliveira M.T. (1997) Raman microspectroscopy of some iron oxides and oxyhydroxides. *Journal of Raman Spectroscopy*, 28, 873–878.
- De La Pierre M., Carteret C., Maschio L., André E., Orlando R., & Dovesi R. (2014) The Raman spectrum of CaCO<sub>3</sub> polymorphs calcite and aragonite: A combined experimental and computational study. *Journal of Chemical Physics*, 140, 164509/1–12.
- Delhaye M. & Dhamelincourt P. (1975), Raman microprobe and microscope with laser excitation. *Journal of Raman Spectroscopy*, 3, 33–43.
- Denson S.C., Pommier C.J.S., & Denton M.V. (2007) The impact of array detectors on Raman spectroscopy. *Journal of Chemical Education*, 84, 67–74.
- Dhamelincourt P., Wallart F., Leclercq M., N’Guyen A.T., & Landon D.O. (1979) Laser Raman molecular microprobe (MOLE). *Analytical Chemistry*, 51, 414A–421A.
- Dubessy J., Caumon M.-C., Rull F., & Sharma S. (2012) Instrumentation in Raman spectroscopy: Elementary theory and practice. In: *Applications of Raman Spectroscopy to Earth Sciences and Cultural Heritage* (J. Dubessy, F. Rull, & M.-C. Caumon, eds.). *EMU Notes in Mineralogy*, 12, European Mineralogical Union and the Mineralogical Society of Great Britain & Ireland, 83–172.

- Edwards H.G.M, Moody C.D., Jorge Vilalr S.E. & Wynn-Williams D.D. (2005) Raman spectroscopic detection of key biomarkers of cyanobacteria and lichen symbiosis in extreme Antarctic habitats: Evaluation for Mars Lander missions. *Icarus*, 174(2), 560-571.
- Edwards H.G.M., Hutchinson I.B., Ingley R., Parnell J., et al. (2013) Raman Spectroscopic Analysis of Geological and Biogeological Specimens of Relevance to the ExoMars Mission. *Astrobiology*, 13(6), 543-549.
- Egan M.J., Angel S.M. & Sharma S.K. (2017) Standoff spatial heterodyne Raman spectrometer for mineralogical analysis. *Journal of Raman Spectroscopy*, 48(11), 1613-1617.
- Egan M.J., Angel S.M. & Sharma S.K. (2018) Optimizing Data Reduction Procedures in Spatial Heterodyne Raman Spectroscopy with Applications to Planetary Surface Analogs. *Applied Spectroscopy*, 72(6), 933-942.
- Elman B.S., Dresselhaus M.S., Dresselhaus G., Maby E.W., & Mazurek H. (1981) Raman scattering from ion-implanted graphite. *Physical Review B*, 24, 1027–1034.
- Englert C.R., Harlander J.M., Emmert J.T., Babcock D.D. & Roesler F.L. (2010) Initial ground-based thermospheric wind measurements using Doppler asymmetric spatial heterodyne spectroscopy (DASH). *Optics Express*, 18(26), 27416-27430.
- Erskine D.J., Edelstein J., Wishnow E., Sirk M., Muirhead P.S. & Muterspaugh M.W. (2016) High-resolution broadband spectroscopy using externally dispersed interferometry at the Hale telescope: Part 2, Photon Noise Theory. *Journal of Astronomical Telescopes, Instruments, and Systems*, 2(4), 1-22.

- Everall N.J. & Howard J. (1989) Signal-to-Noise Considerations in FT-Raman Spectroscopy. *Applied Spectroscopy*, 43(5), 778-781.
- Fateley W.G., Dollish F.R., McDevitt N.T., & Bentley F. F. (1972) *Infrared and Raman Selection Rules for Molecular and Lattice Modes*. Wiley-Interscience, New York.
- Fellgett P. (1967) Conclusions on Multiplex Methods. *Le Journal de Physique Colloques*, 28(C2), 165-171.
- Ferigle S.M. & Meister A.G. (1952) Selection rules for vibrational spectra of linear molecules. *American Journal of Physics*, 20, 421–428.
- Ferini G., Baratta G.A., & Palumbo M.E. (2004) A Raman study of ion irradiated icy mixtures. *Astronomy & Astrophysics*, 414, 757–766.
- Ferraro J.R. (1975) Factor group analysis for some common minerals. *Applied Spectroscopy*, 29, 418–420.
- Ferraro J.R. & Ziomek J.S. (1969) *Introductory Group Theory and Its Application to Molecular Structure*. Plenum Press, New York.
- Freeman J.J., Wang A., Kuebler K.E., Jolliff B.L & Haskin L.A. (2008) Characterization of Natural Feldspars by Raman Spectroscopy for Future Planetary Exploration. *Canadian Mineralogist*, 46(6), 1477-1500.
- Frezzotti M.L., Tecce F., & Casagli A. (2012) Raman spectroscopy for fluid inclusion analysis. *Journal of Geochemical Exploration*, 112, 1–20.
- Fries M. & Steele A. (2011) Raman spectroscopy and confocal Raman imaging in mineralogy and petrography. In: *Confocal Raman Microscopy* (T. Dieing, O. Hollricher, & J. Toporski,

eds.), Springer Series in Optical Sciences, 158. Springer-Verlag, Berlin and Heidelberg, 111–133.

Fuhrer H., Kartha V.B., Krueger P.J., Mantsch H.H. & Jones R.N. (1972) Normal modes and group frequencies – Conflict or Compromise? An in-depth vibrational analysis of cyclohexanone. *Chemical Review*, 72(5), 439-456.

Gaft M. & Nagli L. (2009) Time-resolved laser based spectroscopies for mineralogical research and applications. In: *Micro-Raman Spectroscopy and Luminescence Studies in the Earth and Planetary Sciences* (A. Gucsik, ed.). Mainz, Germany, April 2–4, 2009, American Institute of Physics (AIP) Conference Proceedings, 1163, 3–14.

Gaft M., Reinsfeld R., & Panczer G. (2005) *Modern Luminescence Spectroscopy of Minerals and Materials*. Springer-Verlag, Berlin and Heidelberg.

Galeener F.L. (1982a) Planner rings in glasses. *Solid State Communication*, 44, 1037–1040.

Galeener F.L. (1982b) Planner rings in vitreous silica. *Journal of Non-Crystalline Solids*, 49, 53–62.

Gasda P.J., Acosta-Maeda T.E., Lucey P.G., Misra A.K., Sharma S.K., & Taylor G.J. (2015) Next generation laser-based standoff spectroscopy techniques for Mars exploration. *Applied Spectroscopy*, 69, 173–192.

Gasda P.J., Haldeman E.B., Wiens R.C., Rapin W., et al. (2017) In situ detection of boron by ChemCam on Mars. *Geophysical Research Letters*, 44(17), 8739-8748.

Gendrin A., Mangold N., Bibring J.P., Langevin Y., et al. (2005) Sulfates in Martian Layered Terrains: The OMEGA/Mars Express View. *Science*, 307(5715), 1587-1591.

- Gerstenkorn S. & Luc P. (1976) Emission Spectra Studies by Means of Fourier Transform Spectroscopy in the Visible Range. *Nouvelle Revue d'Optique*, 7(3), 149-157.
- Geusic J.E., Marcos H.M. & Van Uitert L.G. (1964) Laser Oscillations in Nd-doped Yttrium Aluminum, Yttrium Gallium and Gadolinium Garnets. *Applied Physics Letters*, 4(10), 182-184.
- Gillet P. (1993) Stability of magnesite ( $\text{MgCO}_3$ ) at mantle pressure and temperature—A Raman spectroscopic Study. *American Mineralogist*, 78, 1328–1331.
- Gillet P., Daniel I., Guyot F., Matas J., & Chervin J.C. (2000) A thermodynamic model for  $\text{MgSiO}_3$ -perovskite derived from pressure and temperature and volume dependence of the Raman mode frequencies. *Physics of the Earth and Planetary Interiors*, 117, 361–384.
- Gomer N., Gordon C., Lucey P., Sharma S., Carter J., & Angel S. (2011) Raman spectroscopy using a spatial heterodyne spectrometer: Proof of concept. *Applied Spectroscopy*, 65, 849–857.
- Goncharov A.F. (2012) Raman spectroscopy at high pressures. *International Journal of Spectroscopy*, 2012, 617528/1–16.
- Gornushkin I.B., Smith B.W., Panne U. & Omenetto N. (2014) Laser-Induced Breakdown Spectroscopy Combined with Spatial Heterodyne Spectroscopy. *Applied Spectroscopy*, 68(9), 1076-1084.
- Götze J., Nasdala L. Kleeberg R., & Wenzel M. (1998) Occurrence and distribution of “moganite” in agate/chalcedony: A micro-Raman, Rietfeld, and cathodoluminescence study. *Contribution to Mineralogy and Petrology*, 133, 96–105.

- Hagelschuer T., Böttger U., Buder M, Cho Y., et al. (2019) RAX – A Raman Spectrometer for MMX onboard the rover for Phobos. 13<sup>th</sup> IAA Low-Cost Planetary Missions Conference.
- Hajian A.R., Behr B.B., Cenko A.T., Olling R.P. et al. (2007) Initial Results from the UNSO Dispersed Fourier Transform Spectrograph. *Astrophysical Journal*, 661, 616-633.
- Halford R.S. (1946) Motions of molecules in condensed systems: I. Selection rules, relative intensities, and orientation effects for Raman and infrared spectra. *Journal of Chemical Physics*, 74, 8–15.
- Hanley J., Chevrier V.F., Berget D.J. & Adams R.D. (2012) Chlorate salts and solutions on Mars. *Geophysical Research Letters*, 39(8), L08201.
- Harlander J.M. (1991) Spatial heterodyne spectroscopy: Interferometric performance at any wavelength without scanning. University of Wisconsin.
- Harlander J.M., Roesler F.L., Reynolds R.J., Jaehnig K.P. & Sanders III W.T. (1993) Differential field-widened spatial heterodyne spectrometer for investigations at high spectral resolution of the diffuse far-ultraviolet 1548-A emission line from the interstellar medium. *Proceeding of SPIE EUV, X-Ray and Gamma-Ray Instrumentation for Astronomy IV*, 2006, 139-148.
- Harlander J.M., Roesler F.L., Englert C.R., Cardon J.G. & Winperis J. (2004) Spatial heterodyne spectroscopy for high spectral resolution space-based remote sensing. *Optics and Photonics News*, 15(1), 46-51.

- Harlander J.M., Roesler F.L., Cardon J.G., Englert C.R. & Conway R.R. (2002) Shimmer: a spatial heterodyne spectrometer for remote sensing of Earth's middle atmosphere. *Applied Optics*, 41(7) 1343-1352.
- Haskin L.A., Wang A., Rockow K.M., Jolliff B.L., Korotev R.L., & Viskupic K.M. (1997) Raman spectroscopy for mineral identification and quantification for in situ planetary surface analysis: A point count method. *Journal of Geophysical Research*, 102, 19293–19306.
- Hemley R.J., Bell P.M., & Mao H.K. (1987) Laser techniques in high-pressure geophysics. *Science*, 237, 605–612.
- Herzberg G. (1945) *Molecular Spectra and Molecular Structure. II. Infrared and Raman Spectra of Polyatomic Molecules*. Van Nostrand Reinhold, New York.
- Hirschfeld T., Schildkraut E.R., Tannenbaum H. & Tanenbaum D. (1972) Remote spectroscopic analysis of ppm-level air pollutants by Raman spectroscopy. *Applied Physics Letters*, 22(1), 38-40.
- Hirschfeld T. (1976) Fellgett's Advantage in UV-VIS Multiplex Spectroscopy. *Applied Spectroscopy*, 30(1), 68-69.
- Hirschfeld T. & Chase B. (1986) FT-Raman spectroscopy: Development and justification. *Applied Spectroscopy*, 40, 133–137.
- Hoefen T.M., Clark R.N., Bandfield J.L., Smith M.D., et al. (2003) Discovery of olivine in the Nili Fossae Region of Mars. *Science*, 302(5645), 627-630.
- Hobbs P.C.D. (2009) *Building Electro-Optical Systems: Making It All Work*. Wiley, 240-242.

- Hornig D.F. (1948) The vibrational spectra of molecules and complex ions in crystals. I. General theory. *Journal of Chemical Physics*, 16, 1063–1076.
- Hu G., Xiong W., Shi H., Li Z., Shen J., & Fang X. (2015) Raman spectroscopic detection for liquid and solid targets using a spatial heterodyne spectrometer. *Journal of Raman Spectroscopy*, 47, 289–298.
- Hu G., Xiong W., Luo H., Shi H., Li Z., Shen J., Fang X., Xu B. & Zhang J. (2018) Raman Spectroscopic Detection for Simulants of Chemical Warfare Agents Using a Spatial Heterodyne Spectrometer. *Applied Spectroscopy*, 72(1), 151-158.
- Jacquinot P. (1960) New developments in interference spectroscopy. *Reports on Progress in Physics*, 23, 267-312.
- Janesick J.R. (2007) Photon Transfer  $DN \rightarrow \lambda$ . SPIE Press Book.
- Jennings D.E., Weber A., & Brault J.W. (1986) Raman spectroscopy of gases with a Fourier transform spectrometer: The spectrum of D<sub>2</sub>. *Applied Optics*, 25, 284–290.
- Jolliff B.L., Hughes J.M., Freeman J.J. & Zeigler R.A. (2006) Crystal chemistry of lunar merrillite and comparison to other meteoritic and planetary suites of whitlockite and merrillite. *American Mineralogist*, 91(10), 1583-1595.
- Jorge Villar S.E. & Edwards H.G.M. (2006) Raman spectroscopy in astrobiology. *Analytical and Bioanalytical Chemistry*, 384, 100-113.
- Kahn F.D. (1959) The Signal: Noise Ratio of a Suggested Spectral Analyzer. *Astrophysical Journal*, 129, 518-520.

- Kaszowska Z., Malek K., Staniszewska-Slezak E., & Niedzielska K. (2016) Raman scattering or fluorescence emission? Raman spectroscopy study on lime-based building and conservation materials. *Spectrochimica Acta*, A169, 7–15.
- Kim A.G., Linder E.V., Edelstein J. & Erskine D. (2015) Giving Cosmic Redshift Drift a Whirl. *Astroparticle Physics*, 62, 195-205.
- Kingma K.J. & Hemley R.J. (1994) Raman spectroscopic study of microcrystalline silica. *American Mineralogist*, 79, 269–273.
- Kittel C. (1976) *Introduction to Solid State Physics*, 5th edn. John Wiley & Sons, New York.
- Krishnan K. & Krishnan R.S. (1966) Raman and infrared spectra of ethylene glycol. *Proceedings of the Indian Academy of Sciences A*, 64(2), 111-122.
- Kuebler K.E., Jolliff B.L., Wang A., & Haskin L.A. (2006) Extracting olivine (Fo-Fa) compositions from Raman spectral peak positions. *Geochimica et Cosmochimica Acta*, 70, 6201–6222.
- Lam P.K., Yu R., Lee M.W. & Sharma S.K. (1990) Structural distortions and vibrational modes in  $Mg_2SiO_4$ . *American Mineralogist*, 75(1-2), 109-119.
- Lamsal N. & Angel S.M. (2015) Deep-Ultraviolet Raman Measurements Using a Spatial Heterodyne Raman Spectrometer (SHRS). *Applied Spectroscopy*, 69(5), 525-534.
- Lamsal N., Sharma S.K., Acosta T.E. & Angel S.M. (2016) Ultraviolet Stand-off Raman Measurements Using a Gated Spatial Heterodyne Raman Spectrometer. *Applied Spectroscopy*, 70(4), 666-675.

- Landsberg G. & Mandelstam L. (1928) Eine neue Erscheinung bei der Lichtzerstreuung in Krysallen. *Die Naturwissenschaften*, 16(28), 557-558.
- Lebedkin S., Blum C., Stürzl, N., Hennrich, F., & Kappes, M.M. (2011) A low wavenumber extended confocal Raman microscope with very high laser excitation line discrimination. *Review of Scientific Instruments*, 82, 013705/1–6.
- Lenzner M. & Diels J.C. (2016) Concerning the Spatial Heterodyne Spectrometer. *Optics Express*, 24(2), 1829-2839.
- Leonard D.A. (1970) Feasibility Study of Remote Monitoring of Gas Pollutant Emissions by Raman Spectroscopy. National Air Pollution Control Administration Department of Health, Education and Welfare, 1-41.
- Leshin L.A., Mahaffy P.R., Webster C.R., Cabane M., et al. (2013) Volatile, Isotope and Organic Analysis of Martian Fines with the Mars Curiosity Rover. *Science*, 341(6153), 1238937.
- Li Z. & Deen M.J. (2014) Towards a portable Raman spectrometer using a concave grating and a time-gated CMOS SPAD. *Optics Express*, 22, 18736–18747.
- Lindenmaier R., Scharko N.K., Tonkyn R.G., Nguyen K.T., et al. (2017) Improved assignments of the vibrational fundamental modes of ortho, meta and para-xylene using gas and liquid-phase infrared and Raman spectra combined with ab initio calculations: Quantitative gas-phase infrared spectra for detection. *Journal of Molecular Structure*, 1149, 332-351.

- Lopez-Reyes G., Rull F., Venegas G., et al. (2014) Analysis of the scientific capabilities of the ExoMars Raman laser spectrometer instrument. *European Journal of Mineralogy*, 25, 721–733.
- Luc P. & Gerstenkorn S. (1978) Fourier Transform Spectroscopy in the Visible and Ultraviolet Range. *Applied Optics*, 17(9), 1327-1331.
- Lucey P.G., Cooney T.F., & Sharma S.K. (1998) A remote Raman analysis system for planetary landers. In: *Proceeding of the 29th Lunar and Planetary Science Conference*, Abstract #1354.
- Ma C., Zhou Q., Li F., Hao J., Wang J., et al. (2011) Rotator phases of n-heptane under high pressure: Raman scattering and x-ray diffraction studies. *Journal of Physical Chemistry C*, 115, 18310-18315.
- Mammone J.F., Sharma S.K. & Nicol M. (1980) Raman spectra of methanol and ethanol at pressures up to 100 kbar. *Journal of Physical Chemistry*, 84, 3130-3134.
- Maraduddin A.A. & Vosko S.H. (1968) Symmetry properties of the normal vibrations of a crystal. *Reviews of Modern Physics*, 40, 1–37.
- Martín-Torres F.J., Zorzano M.P, Valentín-Serrano P., Harri A.M., et al. (2015) Transient liquid water and water activity at Gale crater on Mars. *Nature Geoscience*, 8, 357-361.
- Matousek P., Towrie M., Stanley A., & Parker A.W. (1999) Efficient rejection of fluorescence from Raman spectra using picosecond Kerr gating. *Applied Spectroscopy*, 53, 1485–1489.

- Matson D.W., Sharma S.K., & Philpotts J.A. (1983) The structure of high-silica alkali-silicate glasses—a Raman spectroscopic investigation. *Journal of Non-Crystalline Solids*, 58, 323–352.
- Matson D.W., Sharma S.K., & Philpotts J.A. (1986) Raman spectra of some tectosilicates and of glasses along the orthoclase-anorthite and nepheline-anorthite joins. *American Mineralogist*, 71, 694–704.
- Maurice S., Wiens R.C., Anderson R., Beyssac O., et al. (2015) Science Objectives of the SuperCam Instrument for the Mars2020 Rover. LPSC 46.
- Maurice S., Wiens R.C., Bernardi P., Cais P., et al. (2021) The SuperCam Instrument suite on the Mars 2020 Rover: Science objectives and Mast-Unit Description. *Space Science Review*. In review.
- McClung F.J. & Hellwarth R.W. (1962) Giant Optical Pulsations from Ruby. *Journal of Applied Physics*, 33(3), 828-829.
- McCreery R.L. (2000) *Raman Spectroscopy for Chemical Analysis*. John Wiley & Sons, New York.
- McKeown D.A. (2005) Raman spectroscopy and vibrational analyses of albite: From 25°C through the melting temperature. *American Mineralogist*. 90, 1506–1517.
- McMillan P. (1985) Vibrational spectroscopy in the mineral sciences. In: *Microscopic to Macroscopic—Atomic Environments to Thermodynamic Properties* (S.W. Kieffer & A. Navrotsky, eds.). *Reviews in Mineralogy*, 14. Mineralogical Society of America, Washington, DC, 9–63.

- McMillan P.F. & Hofmeister A.M. (1988) Infrared and Raman spectroscopy. In: Spectroscopic Methods in Mineralogy and Geochemistry (F.C. Hawthorne, ed.). Reviews in Mineralogy, 18. Mineralogical Society of America, Washington, DC, 99–159.
- McMillan P.F. & Wolf G.H. (1995) Vibrational spectroscopy of silicate liquids. In: Structure, Dynamics and Properties of Silicate Melts (J.F. Stebbins, P.F. McMillan & D.B. Dingwell, eds.), Reviews in Mineralogy, 32. Mineralogical Society of America, Washington, DC, 247–314.
- McMillan P.F., Dubessy J., & Hemley R. (1996) Applications in Earth, planetary and environmental sciences. In: Raman Microscopy: Developments and Applications (G. Turrell & J. Corset, eds.). Academic Press, New York, 289–365.
- McSween H.Y., Ruff S.W., Morris R.V., Bell III J.F., et al. (2006) Alkaline volcanic rocks from the Columbia Hills, Gusev crater, Mars. *Journal of Geophysical Research Planets*, 111(E9), E09S91.
- Misra A.K., Acosta-Maeda T.E., Porter J.N., Egan M.J., et al. (2020) Remote Raman Detection of Chemicals from 1752 m During Afternoon Daylight. *Applied Spectroscopy*, 74(2), 233-240.
- Mertz L. (1967) Auxiliary computation for Fourier spectrometry. *Infrared Physics*, 7(1), 17-23.
- Ming D.W., Archer Jr. P.D., Glavin D.P., Eigenbrode J.L., et al (2014) Volatile and Organic Compositions of Sedimentary in Yellowknife Bay, Gale Crater, Mars. *Science*, 343(6169), 1245267.

- Misra A.K., Sharma S.K., Chio C.H., Lucey P.G., & Lienert B. (2005) Pulsed remote Raman system for daytime measurements of mineral spectra. *Spectrochimica Acta*, A61, 2281–2287.
- Misra A.K., Sharma S.K. & Lucey P.G. (2006) Remote Raman Spectroscopic Detection of Minerals and Organics Under Illuminated Conditions from a Distance of 10 m Using a Single 532 nm Laser Pulse. *Applied Spectroscopy*, 60(2), 223-228.
- Milam K.A., McSween H.Y., Moersch J. & Christensen P.R. (2010) Distribution and variation of plagioclase compositions on Mars. *Journal of Geophysical Research Planets*, 115(E9), E09004.
- Morgan P.K., Scott J.R. & Jovanovic I. (2016) Hybrid Interferometric/Dispersive Atomic Spectroscopy of Laser-Induced Uranium Plasma. *Spectrochimica Acta, Part B*, 116, 58-62.
- Morris R.V., Klingelhofer G., Schroder C., Rodionov D.S., et al. (2006) Mossbauer mineralogy of rock, soil, and dust at Gusev crater, Mars: Spirit's journey through weakly altered olivine basalt on the plains and pervasively altered basalt in the Columbia Hills. *Journal of Geophysical Research Planets*, 111, E02S13.
- Morris R.V., Ruff S.W., Gellert R., Ming D.W., et al. (2010) Identification of Carbonate-Rich Outcrops on Mars by the Spirit Rover. *Science*, 329(5990), 421-424.
- Mouginot J., Pommerol A., Beck P., Kofman W. & Clifford S.M. (2012) Dielectric map of the Martian northern hemisphere and the nature of plain filling materials. *Geophysical Research Letters*, 39, L02202.

- Murchie S.L., Mustard J.F., Ehlmann B.L., Milliken R.E., et al. (2009) A synthesis of Martian aqueous mineralogy after 1 Mars year of observations from the Mars Reconnaissance Orbiter. *Journal of Geophysical Research*, 114, E00D06.
- Mustard J.F., Murchie S.L., Pelkey S.M., Ehlmann B.L., et al. (2008) Hydrated silicate minerals on Mars observed by the Mars Reconnaissance Orbiter CRISM instrument. *Nature*, 454, 305-309.
- Mustard J.F., Adler M., Allwood A., Bass D.S., et al. (2013) Report of the Mars 2020 Science Definition Team.
- Mysen B.O. & Richet P. (2005) *Silicate Glasses & Melts—Properties and Structure*. Elsevier, New York.
- Nachon M., Clegg S.M., Mangold N., Schroder S., et al. (2014) Calcium sulfate veins characterized by ChemCam/Curiosity at Gale Crater, Mars. *Journal of Geophysical Research Planets*, 119(9), 1991-2016.
- Nadungadi T.M.K. (1939) Effect of crystal orientation on the Raman spectrum of sodium nitrate. *Proceedings of the Indian Academy of Sciences*, A10, 197–212.
- Nasdala L., Smith D.C., Kaindl R., & Ziemann M.A. (2004) Raman spectroscopy: Analytical perspectives in mineralogical research. In: *Spectroscopic Methods in Mineralogy*, EMU Notes in Mineralogy, 6 (A. Beran & E. Libowitzky, eds.). European Mineralogical Union and Mineralogical Society of Great Britain and Ireland, 281–343.
- Nieuwoudt M.K., Comins J.D., & Cukrowski I. (2011) The growth of the passive film on iron in 0.05 MNaOH studied in situ by Raman micro-spectroscopy and electrochemical

- polarisation. Part I: near-resonance enhancement of the Raman spectra of iron oxide and oxyhydroxide compounds. *Journal of Raman Spectroscopy*, 42, 1335–1339.
- Osterloo M.M., Hamilton V.E., Bandfield J.L., Glotch T.D., et al. (2008) Chloride-Bearing Materials in the Southern Highlands of Mars. *Science*, 319(5870), 1651-1654.
- Owen H. (2007) The impact of volume phase holographic filters and gratings on the development of Raman instrumentation. *Journal of Chemical Education*, 84, 61-66.
- Panczer G., De Ligny D., Mendoza C., Gaft M., Seydoux-Guillaume A.-M., & Wang X. (2012) Raman and fluorescence. In: *Applications of Raman Spectroscopy to Earth Sciences and Cultural Heritage* (J. Dubessy, F. Rull, & M.-C. Caumon, eds.). EMU Notes in Mineralogy, 12. European Mineralogical Union and the Mineralogical Society of Great Britain & Ireland, 1–22.
- Pankove J. (1971) *Optical Processes in Semiconductors*. Dover Publications.
- Pandya N., Sharma S.K., & Muenow D.W. (1988) Calibration of a multichannel micro-Raman spectrograph with plasma lines of argon and krypton ion lasers. In: *Microbeam Analysis 1988: Proceedings of the 23rd Annual Conference of the Microbeam Analysis Society*, Milwaukee, Wisconsin, 8–12 August, 1988 (D. E. Newbury, ed.). San Francisco Press, San Francisco, 171–174
- Pasteris J.D., Kuehn C.A., & Bodnar R.J. (1986): Applications of the laser Raman microprobe Ramanor U-1000 to hydrothermal ore deposits: Carlin as an example. *Economic Geology*, 81, 915–930.

- Porto S.P.S., Giordmaine J.A., & Damen T.C. (1966) Depolarization of Raman scattering in calcite. *Physical Review*, 147, 608–611.
- Rai C.S., Sharma S.K., Muenow D.W., Matson D.W., & Byers C.D. (1983) Temperature dependence of CO<sub>2</sub> solubility in high-pressure quenched glasses of diopside composition. *Geochimica et Cosmochimica Acta*, 47, 953–958.
- Raman C.V. (1928) A change of wave-length in light scattering. *Nature*, 121, 619–619.
- Raman C.V. & Krishnan K.S. (1928) A new type of secondary radiation. *Nature*, 121, 501–502.
- Rapin W., Meslin P.Y., Maurice S., Vaniman D., et al. (2016) Hydration state of calcium sulfates in Gale crater, Mars: Identification of bassanite veins. *Earth and Planetary Science Letters*, 452, 197-205.
- Rull Pérez F. & Martínez-Frias J. (2006) Raman spectroscopy goes to Mars. *Spectroscopy Europe*, 18(1), 18-21.
- Reynard B., Montagnac G., & Cardon H. (2012) Raman spectroscopy at high pressure and temperature for study of the Earth's mantle and planetary minerals. In: *Applications of Raman Spectroscopy to Earth Sciences and Cultural Heritage* (J. Dubessy, F. Rull, & M.-C. Caumon, eds.). *EMU Notes in Mineralogy*, 12, European Mineralogical Union and the Mineralogical Society of Great Britain & Ireland, 367–390.
- Riebe D., Beitz T., Dosche C., Löhmannsröben H.G., Raab V., Raab C. & Unverzagt M. (2014) High-Resolution Spectrometer Using Combined Dispersive and Interferometric Wavelength Separation for Raman and Laser-Induced Breakdown Spectroscopy (LIBS). *Applied Spectroscopy*, 68(9), 1030-1038.

- Roedder E. (1984) Nondestructive methods of determination of inclusion composition. In: Fluid Inclusions (E. Roedder, ed.), Reviews in Mineralogy, 12, Mineralogical Society of America, Washington, DC, 79–108.
- Rosasco G.J., Etz E.S., & Cassatt W.A. (1975) The analysis of discrete fine particles by Raman spectroscopy. *Applied Spectroscopy*, 29, 396–404.
- Rossano S. & Mysen B.O. (2012) Raman spectroscopy of silicate glasses and melts in geological systems. In: Applications of Raman Spectroscopy to Earth Sciences and Cultural Heritage (J. Dubessy, F. Rull, & M.-C. Caumon, editors). EMU Notes in Mineralogy, 12, European Mineralogical Union and the Mineralogical Society of Great Britain & Ireland, 321–366.
- Rousseau B., Van Alsenoy C., Keuleers R. & Desseyn H.O. (1998) Solids Modeled by Ab-initio Crystal Field Methods. Part 17. Study of the Structural and Vibrational Spectrum of Urea in the Gas Phase and in its P42<sub>1</sub>m Crystal Phase. *Journal of Physical Chemistry*, 102(32), 6540-6548.
- Rull F. (2012) The Raman effect and the vibrational dynamics of molecules and crystalline solids. In: Applications of Raman Spectroscopy to Earth Sciences and Cultural Heritage (J. Dubessy, F. Rull & M.-C. Caumon, eds.). EMU Notes in Mineralogy, 12, European Mineralogical Union and the Mineralogical Society of Great Britain & Ireland, 1–60.
- Salthouse J.A. & Ware M.J. (1972) Point Group Character Tables and Related Data. Cambridge University Press, Cambridge.
- Sautter V., Toplis M.J., Wiens R.C., Cousin A., (2015) In situ evidence for continental crust on early Mars. *Nature Geoscience*, 8, 605-609.

- Sharma S.K. (1979) Raman spectroscopy at very high pressure. *Carnegie Institution of Washington Year Book*, 78, 660–665.
- Sharma S.K., Mammone J.F. & Nicol M.F. (1981) Raman investigations of ring configurations in vitreous silica. *Nature*, 292, 140-141.
- Sharma S.K. (1989) Applications of advanced Raman techniques in earth sciences. *Vibrational Spectra and Structure*, 17B, 513 568.
- Sharma S.K., Lucey P.G., Ghosh M., Hubble H.W. & Horton K.A. (2003) Stand-off Raman spectroscopic detection of minerals on planetary surfaces. *Spectrochimica Acta Part A: Molecular and Biomolecular Spectroscopy*, 59(10), 2391-2407.
- Sharma S.K. (2007) New trends in telescopic remote Raman spectroscopic instrumentation. *Spectrochimica Acta*, A68, 1008–1022.
- Sharma S.K. & Simons B. (1981) Raman study of crystalline polymorphs and glasses of spodumene ( $\text{LiAlSi}_2\text{O}_6$ ) composition quenched from various pressure. *American Mineralogist*, 66, 118–126.
- Sharma S.K., Hoering T.C., & Yoder H.S., Jr. (1979a) Quenched melts of akermanite compositions with and without  $\text{CO}_2$ -characterization by Raman spectroscopy and gas chromatography. *Carnegie Institution Washington Year Book*, 78, 537–542.
- Sharma, S. K., Virgo D., & Mysen, B.O. (1979b) Raman study of the coordination of aluminium in jadeite melts as function of pressure. *American Mineralogist*, 64, 779–787.
- Sharma S.K., Mammone J.F., & Nicol M.F. (1981) Ring configurations in vitreous silica – a Raman spectroscopic investigation. *Nature*, 292, 140–141.

- Sharma S.K., Philpotts J.A., & Matson D.W. (1985) Ring distributions in alkali- and alkaline-earth alumino-silicate framework glasses—a Raman spectroscopic study. *Journal of Non-Crystalline Solids*, 71, 403–410.
- Sharma S.K., Yoder H.S., Jr., & Matson D.W. (1988) Raman study of some melilites in crystalline and glassy states. *Geochimica et Cosmochimica Acta*, 52, 1961–1967.
- Sharma S.K., Wang Z., & van der Laan S. (1996) Raman spectroscopy of oxide glasses at high pressure and high temperature. *Journal of Raman Spectroscopy*, 27, 739–746.
- Sharma S.K., Cooney T.F., Wang Z., & van der Laan, S. (1997) Raman band assignments of silicate and germanate glasses in light of high pressure and high temperature spectral data. *Journal of Raman Spectroscopy*, 28, 679–709.
- Sharma S.K., Misra A.K., & Sharma B. (2005) Portable remote Raman system for monitoring hydrocarbon, gas hydrates and explosives in the environment. *Spectrochimica Acta*, A61, 2404–2412.
- Sheinis A.I., Mierkiewicz E., Roesler F., Harlander J. & Bodkin A. (2008) A Spatial Heterodyne Spectrometer for Diffuse H- $\alpha$  Spectroscopy. *Proceedings SPIE*, 7014, 70140I.
- Shimanouchi T. (1972) Tables of molecular vibrational frequencies consolidated Volume I. U.S. Department of Commerce, 1-160.
- Sonwalker N., Sunder S.S., & Sharma S.K. (1991) Raman microprobe spectroscopy of icing on metal surfaces. *Journal of Raman Spectroscopy*, 22, 551–557.
- Spinella F., Barrata G.A., & Strazzulla G. (1991) An apparatus for in situ Raman spectroscopy of ion-irradiated frozen target. *Review of Scientific Instruments*, 62, 1743–1745.

- Squyres S.W., Arvidson R.E., Bell III J.F., Calef III F., et al. (2012) Ancient Impact and Aqueous Processes at Endeavour Crater, Mars. *Science*, 336, 570-576.
- Srivastava A. & Singh V.B. (2007) Theoretical and experimental studies of vibrational spectra of naphthalene and its cation. *Indian Journal of Pure & Applied Physics*, 45, 714-720.
- Stopar J.D., Lucey P.G., Sharma S.K., Misra A.K., et al. (2005) Raman efficiencies of natural rocks and minerals: Performance of a remote Raman system for planetary exploration at a distance of 10 meters. *Spectrochimica Acta Part A: Molecular and Biomolecular Spectroscopy*, 61(10), 2315-2323.
- Storrie-Lombardi M.C., Hug W.F., McDonald G.D., Tsapin A.I., & Neelson, K.H. (2011) Hollow cathode ion lasers for deep ultraviolet Raman spectroscopy and fluorescence imaging. *Review of Scientific Instruments*, 72, 4452–4459.
- Strange K.A., Paul K.C. & Angel S.M. (2016) Transmission Raman Measurements Using a Spatial Heterodyne Raman Spectrometer. *Applied Spectroscopy*, 71(2), 250-257.
- Strazzulla G. & Baratta, G.A. (1992) Carbonaceous material by ion irradiation in space. *Astronomy and Astrophysics*, 266, 434–438.
- Strazzulla G., Baratta G.A., & Palumbo M.E. (2001) Vibrational spectroscopy of ion-irradiated ices. *Spectrochimica Acta*, A57, 825–842.
- Sweedler J.V., Jalkian R.D., Sims G.R., & Denton M.B. (1990) Crossed Interferometric Dispersive Spectroscopy. *Applied Spectroscopy*, 44(1), 14-20.

- Taran M., Koch-Müller M., Wirth R., Abs-Wurmbach I., Rhede D., & Greshake A. (2009) Spectroscopic studies of synthetic and natural ringwoodite,  $\gamma$ -(Mg, Fe) $_2$ SiO $_4$ . *Physics and Chemistry of Minerals*, 36, 217–232.
- Trulson M.O. & Mathies R.A. (1986) Raman cross section measurements in the visible and ultraviolet using an integrating cavity: Application to benzene, cyclohexane, and cacodylate. *Journal of Chemical Physics*, 84(4), 2068-2074.
- Urmos J.P., Sharma S.K., & Mackenzie F.T. (1991) Characterization of some biogenic carbonates with Raman spectroscopy. *American Mineralogist*, 76, 641–646.
- Vaniman D.T., Bish D.L., Ming D.W., Bristow T.F., et al. (2014) Mineralogy of a Mudstone at Yellowknife Bay, Gale Crater, Mars. *Science*, 343(6169), 1243480.
- Walrafen G.E. (1964) Raman spectral studies of water structure. *Journal of Chemical Physics*, 40(11), 3249-3256.
- Wang Z., Cooney T.F., & Sharma S.K. (1993) High-temperature structural investigation of iron-bearing glasses and melts. *Contributions to Mineralogy & Petrology*, 115, 112–122.
- Wang Z., Cooney T.F., & Sharma S.K. (1995) In situ structural investigation of iron-containing silicate melts and glasses. *Geochimica Cosmochimica Acta*, 59, 1571–1577.
- Wang A., Haskin L.A., & Cortez, E. (1998) Prototype Raman spectroscopic sensor for in situ mineral characterization on planetary surfaces. *Applied Spectroscopy*, 52, 477–487.
- Wang A., Jolliff B.L., Haskin L.A., Kuebler K.E., & Viskupic K.M. (2001) Characterization and comparison of structural and compositional features of planetary quadrilateral pyroxenes by Raman spectroscopy. *American Mineralogist*, 86, 790–806.

- Wang A., Jolliff B.L., Haskin L.A., Kuebler K.E. & Viskupic K.M. (2001) Characterization and comparison of structural and compositional features of planetary quadrilateral pyroxens by Raman spectroscopy. *American Mineralogist*, 86(7-8), 790-806.
- Wang A., Haskin L.A., Lane A.L., et al. (2003) Development of the Mars Microbeam Raman Spectrometer (MMRS). *Journal of Geophysical Research*, 108 E1, 5005/1–18.
- Wang A., Kuebler K.E., Jolliff B.L. & Haskin L.A. (2004) Raman spectroscopy of Fe-Ti-Cr-oxides, case study: Martian meteorite EETA79001. *American Mineralogist*, 89(5-6), 665-680.
- Wang W., Major A., & Paliwal J. (2012) Grating-stabilized external cavity diode lasers for Raman spectroscopy—A review. *Applied Spectroscopy Reviews*, 47, 116–143.
- Wang A., Wei J., Lambert J.L. & Hutchinson I (2015) A Compact Integrated Raman Spectrometer (CIRS) for Fine-Scale Definitive Mineralogy in Venus Explorations. *Venus Science Priorities for Laboratory Measurements and Instrument Definition Workshop*, LPI contribution 1838, pg. 4027.
- Warren J.L. (1968) Further considerations on the symmetry properties of the normal vibrations of a crystal. *Reviews of Modern Physics*, 40, 38–76.
- White W.B. (1975) Structural interpretation of lunar and terrestrial minerals by Raman spectroscopy. In: *Infrared and Raman spectroscopy of Lunar and Terrestrial Minerals* (C. Karr, Jr., ed.). Academic Press, New York, 325–358.
- White W.B. & De Angelis B.A. (1967) Interpretation of the vibrational spectra of spinels. *Spectrochimica Acta*, A23, 985–995.

- Wiens R.C., Sharma S.K., Thompson J., Misra A. & Lucey P.G. (2005) Joint analyses of laser-induced breakdown spectroscopy (LIBS) and Raman spectroscopy at stand-off distances. *Spectrochimica Acta Part A: Molecular and Biomolecular Spectroscopy*, 61(10), 2324-2334.
- Wiens R.C., Maurice S., McCabe K., et al. (2016) The SUPERCAM remote sensing instrument suite for Mars 2020. In: proceedings of the 47th Lunar and Planetary Science Conference, Abstract #1332.
- Wiens R.C., Maurice S., Robinson S.H., Nelson A.E., et al. (2021) The SuperCam Instrument Suite on the NASA Mars 2020 Rover: Body Unit and Combined Systems Tests. *Space Science Reviews*. In review.
- Winston H. & Halford R.S. (1949) Motions of molecules in condensed systems: V. Classification of motions and selection rules for spectra according to space symmetry. *Journal of Chemical Physics*, 17, 607–616.
- Zettner A., Gojani A.B., Schmid T. & Gornushkin I.B. (2020) Evaluation of a Spatial Heterodyne Spectrometer for Raman Spectroscopy of Minerals. *Minerals*, 10(2), 202.
- Zhao J. & McCreery R.L. (1996) Multichannel Fourier transform Raman spectroscopy: Combining the advantages of CCDs with interferometry. *Applied Spectroscopy*, 50, 1209–1214.
- Zhao J. & McCreery R.L. (1997) Multichannel FT-Raman spectroscopy: Noise analysis and performance assessment. *Applied Spectroscopy*, 51, 1687–1697.